Diplomarbeit

DEVELOPMENT OF AN EBSD DATA ANALYZING SOFTWARE FOR MICROTEXTURE AND MESOTEXTURE STUDIES IN CUBIC MATERIALS

Sandra Zitz

Anerkannt am
Institut für Metallkunde und Werkstoffprüfung
Montanuniversität Leoben, im November 1998

1 Introduction

The electron was discovered by J. J. Thomson in 1897. In 1906 he got the Nobel Prize for demonstrating that the electron was a particle. As a nice irony of history, just 31 years later his son G. P. Thomson was awarded the Nobel Prize for showing that the electron was also a wave *(Hawkes, 1998)*.
The idea to treat an electron as a wave was based on the theory which Luis de Broglie presented in his doctoral thesis, describing matter as waves *(Hey & Walters, 1998)*.
The experimental verification of the wave nature of electrons was found by G. P. Thomson and Reid in Great Britain, and at the same time independently by Davidson and Germer in USA in 1927. They performed electron scattering experiments in crystalline materials.
Later on, in 1928, Bethe succeeded to use the Schrödinger equation to describe scattering of a beam of fast electrons by the periodic potential of a crystal (*Humphreys, 1979)*.
In 1931, the first electron microscope was built at the Technological University of Berlin by Max Knoll and Ernst Ruska. However, this Transmission Electron Microscope (TEM) just reached a magnification of about thirteen times *(Mulvey, 1989)*. Two years later, in 1933, Ruska had developed a TEM, which was able to give a magnification of 10,000 times.

Since that time a lot of work has been done in the field of electron microscopy. Modern TEMs and Scanning Electron Microscopes (SEM) open a wide world of different possibilities to scientists of several fields.
Also in the field of Materials Science, electron microscopes do give researchers insight into materials' microstructure and chemical composition.
Also in industry electron microscopes, especially SEMs, are frequently used in research and development works and to control the quality of products.

One of the numerous capabilities in Electron Microscopy is the use of electron diffraction, for example to measure crystal orientation in crystalline materials or to identify phases, the size of which would not allow the use of any X-ray method.

TEM based electron diffraction techniques like SAD (Selected Area Diffraction) and CBED (Convergent Beam Electron Diffraction) are well known. In TEM one can take orientation measurements from grains of 10 nm in diameter with an angular precision of about 0.1° for CBED *(Dingley & Randle, 1992)*.
However, specimen preparation for TEM is quite complicated and time consuming since a thin foil has to be prepared to make the specimen transparent to electrons. Due to the small area one can investigate, usually just a few grains can be found in one sample. This makes a study of texture or grain boundary geometry distribution

difficult to perform in TEM, since a huge amount of samples have to be investigated to get a result with statistical relevance.

There are three diffraction techniques which can be used in SEM. Two of them are based on the backscattering of electrons, *i.e.,* Selected Area Channeling (SAC) and Electron Back Scatter Diffraction (EBSD) and one on X-rays (Kossel technique). All these techniques can be applied to bulk specimens. When using backscattered electrons it is possible to measure the crystal orientation of several hundreds, or using automated systems even thousands of grains within one specimen. This allows one to gain statistically meaningful information about crystal orientation and grain boundary geometry within a reasonable time.
The electron channeling effect is used for pattern formation in SAC and EBSD techniques. This means that the probability that an electron will be backscattered will depend on the angle between the electron travelling direction and the crystal plane.
The SAC technique works with a rocking beam or rocking specimen stage, dependent on the instrument, producing different angles of beam incidence. In contrast to this, the EBSD method is based on the idea that also when using a stationary beam, the electrons scattered elastically within the specimen will travel in all possible directions, producing also a diffraction pattern. For EBSD the specimen has to be tilted to about 70 degrees to enhance the intensity of backscattered electrons.
Due to lens errors, the spatial resolution of SAC is normally about 10 µm, but it can be reduced to about 2 µm. The angular range of the diffraction pattern depends on the rocking angle of the beam or the specimen and is of the order of 14°. The specimen itself has to have a flat and polished surface.
The EBSD technique is now widely accepted to be the more powerful of these two, mainly because of the higher spatial resolution (about 0.5 µm), the fairly easy specimen preparation, the relatively high precision of about 1°, and the easier interpretation of the diffraction pattern due to larger angular coverage.

At Tampere University of Technology (TUT), a commercial EBSD System was installed in 1996 at the Center for Electron Microscopy (CEM).
The original aim of the present work was to study the capabilities of the system and to gather experience of its use for different applications.
For this purpose, measurements on different steel and copper specimens were conducted and analyzed.
Due to bugs in the commercial software delivered with the system, the analysis however did not give correct results. There was also a need to carry out the data analysis on a computer other than the SEM computer, which is normally needed to operate the microscope.
Therefore it was decided to develop a stand-alone analyzing software for the EBSD data for microtexture and grain boundary analysis. The current version of the software is applicable to cubic crystal systems with the point group $m\bar{3}m$, making it possible to analyze most technically important materials such as steels, copper and aluminium, just to mention a few.

In the following chapters, the development of this EBSD data analysis software is discussed. In chapter 2, the EBSD system itself is first described. Its application in microtexture and grain boundary studies, strain measurement and phase identification is described by giving a short literature review in chapter 3.
Chapter 4 deals with data representation for microtexture and grain boundary studies with the necessary theoretical background.
The setup of the EBSD system used at TUT is outlined in chapter 5.
The analyzing software developed under Visual Basic 5.0 is described in chapter 6.
Additional computer simulations were done to illustrate the textural influence on the grain boundary structure. These results are presented in chapter 7.
Finally, measurements on steel and copper specimens and the analysis of the data are presented and discussed in chapter 8.

2 Electron Back Scatter Diffraction

2.1 Historical Survey

The first observation of an electron backscattering pattern was reported by *Alam, Blackman & Pashley (1954)*, who called them 'High-angle Kikuchi patterns'. The diffraction pattern was not produced in a SEM, but in an instrument consisting of an electron source and a single lens, which focused the electron beam onto the specimen. The pattern was recorded on an electron-sensitive film, directly by exposing the film to the backscattered electrons.

In 1973, Venables integrated this method into a scanning electron microscope *(Venables & Harland, 1973)*, which was a real breakthrough since it allowed viewing at the sample and selection of the area of interest prior to collecting the diffraction pattern. They introduced the name 'Electron BackScattering Pattern (EBSP)' and it seems that they were not aware at the prior work of Alam and coworkers. However, the quality of the pattern they recorded was rather disappointing, since they used for viewing a phosphor screen which was then photographed.

A group at Bristol University, led by D. Dingley, was working at that time on recording backscattering Kossel diffraction patterns in an electron microscope.[1] To view Kossel X-ray diffraction a filter has to be used to remove the backscattered electrons. After the publications of Venables and coworkers, Dingley decided to remove the beryllium filter and to use an electron sensitive film instead of the X-ray sensitive one. The quality of the so recorded electron backscattering patterns was much better than that obtained by Venables, and a lot of new details could be seen in these patterns. Later, Dingley used a phosphor screen to view the pattern as Venables did, but could make use of the development of low-light imaging systems, *i.e.*, a silicon intensified target (SIT) camera. Further image processing increases the quality of the so recorded patterns. *(Dingley, Baba-Kishi & Randle, 1995)*.

The name Backscattered Kikuchi Diffraction (BKD) was also introduced by Dingley.

The use of low light TV cameras instead of a photographic film allows real-time imaging of the diffraction pattern. Development of computer-aided on-screen analysis was an important step in the development of the system.

---

[1] *Kossel X-ray diffraction is the third diffraction method in SEM. Diffracted X-rays, which emerge from the interaction of an electron beam and the specimen are used instead of electrons used in EBSD and SAC. The big disadvantage of this technique is that the pattern can not be viewed as a live image but has to be recorded on a X-ray sensitive film. Although the precision is very good (0.1°), what is an advantage of X-ray diffraction due to the longer wavelength, the spatial resolution is worse than in EBSD or even SAC, since grain size has to be bigger than about 10* μm.

Today fully automated systems with stage or beam movement allow making several thousand measurements during one night.
The low light cameras are the most expensive parts of the EBSD system, although the technical development in this field has lowered the prices and enhanced the image quality. For example, charge coupled device (CCD) cameras are already commercially available [1], giving less noisy images than SIT cameras. In addition, image distortion can be eliminated because no camera lenses are required and for this reason also the price is lower than that of SIT cameras. The limiting factor for the use of the first CCD cameras was the low sensitivity compared to SIT cameras. Today, CCD cameras are usually used in the field of phase identification[2], and they will probably replace the SIT cameras in the future.

In 1992 there were only about 40 EBSD systems worldwide *(Randle, 1992),* but the number of instruments has increased rapidly as can be seen from the numerous articles published on applications of EBSD. In Finland there are already two EBSD systems installed.

2.2 EBSD Setup

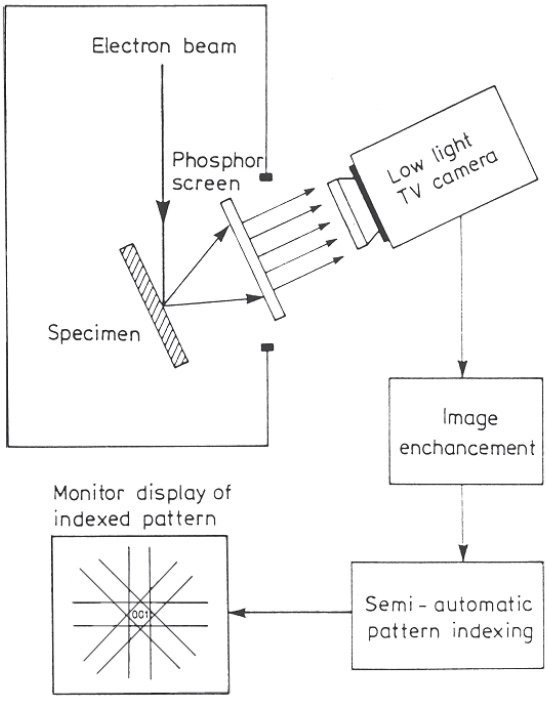

Figure 2-1 Setup of the EBSD system (Randle, 1992).

A typical setup of EBSD is illustrated in Fig. 2-1.
For taking an EBSD pattern, the electron beam is generally set to spot mode.
In order to have a high fraction of backscattered electrons the specimen is tilted to about 70 degrees. When the electron beam hits the specimen, it will spread due to scattering of the electrons in all possible directions within the specimen. The Bragg condition for diffraction is fulfilled for several crystal planes, and a diffraction pattern is formed by the backscattered electrons. This pattern consists of several bright bands, the so-called Kikuchi bands. These bands will intersect at points called poles, which represent low index directions in the crystal lattice.

[1] *http://www.oxinst.com/mag/products/ebsdcam.htm*
[2] *http://www.sandia.gov/materials/sciences/Capabilities/Kikuchi_Patterns/Kikuchi_One_Page.html*

The backscattered electrons hit the fluorescent phosphor screen causing emission of light, providing that the electron energy is high enough.
There are different possible mounting positions for the phosphor screen. It can be mounted parallel to the electron beam, but also different tilt angles are used. Also the position of the screen relative to the specimen surface varies in different configurations. The configuration used in the work of *Krieger Lassen (1994),* is shown in Fig. 2-2 as an example.

Figure 2-2 Geometrical arrangement of the phosphor screen, specimen and TV camera in the work of Krieger Lassen (1994).

The very weak pattern seen on the screen (~10^{-3} lux) is recorded by the low light TV camera.
The video signal is send to a framestore device which digitizes the image and performs frame averaging to reduce noise. As an additional image manipulation, background substraction is done to enhance the contrast.
For background substraction, an EBSP is taken by scanning the beam over larger specimen area, where several grains contribute to the image. In this condition, no Kikuchi bands are visible, just the background produced by the backscattered electrons having high enough energy to cause light emission in the phosphor screen. This pattern is then substracted from subsequent backscattered Kikuchi patterns. The effect of background substraction can be seen in Fig. 2-3.

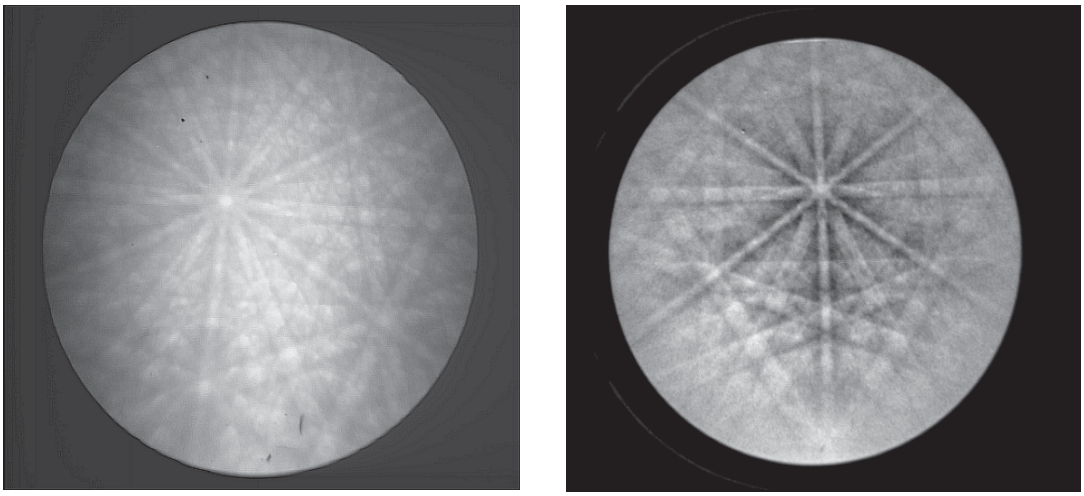

a) *b)*

Figure 2-3 These two EBSPs were recorded with the system at TUT. Picture a) shows an EBSP taken from a brittle failed tungsten filament. For this pattern no background substraction was done, only frame averaging was performed to reduce noise. Pattern b) is from a copper specimen with background substraction. The slight distortion of the pattern is due to the camera lenses, the phosphor screen itself is a circle.

The pattern can be seen directly on the computer screen, which allows on-line analysis of the diffraction pattern. The operator has to indicate two known poles or at least two Kikuchi bands with the mouse pointer. A computer program will then determine the crystal orientation. Usually, a computer generated diffraction pattern will be overlaid on the measured pattern to allow the operator to confirm or to reject the result. Finally, the orientation data will be stored in a file.

Resolution of the system depends on the emission volume of the backscattered electrons. Because of the high tilt of the sample, backscattered electrons, having energy high enough to cause luminescence on the phosphor screen, are emitted from a small depth of about 20 nm, depending on material and microscope operation parameters. Due to the specimen tilt, the lateral resolution is also different for the directions perpendicular and parallel to the specimen tilt axis. It depends on the interaction volume and so again on the microscope operating parameters and the specimen.
As an example for spatial resolution, let's consider the result of *Kenik (1996)* using a Philips XL30/FEG SEM with a Shottky FEG electron source. Kenik made measurements near a grain boundary, which in one case was parallel to the specimen tilt axis and in the other case perpendicular to it. When taking a diffraction pattern close to a grain boundary, backscattered electrons will be emitted of both grains and a double image containing crystal orientation information of both grains is formed. Kenik obtained a diffraction pattern of just one grain when moving only 50 nm away from the grain boundary lying perpendicular to the specimen tilt axis. However, if the grain boundary was lying parallel to the tilt axis, the required distances from the grain boundary to identify a grain unambiguously were 100 nm and 200 nm for the lower and upper grains, respectively. This difference in lateral resolution has to be taken into account when interpreting results of fully automated systems working with small step sizes between measurements.
The accuracy of the EBSD system is generally about 1 degree for absolute orientation measurements and 0.5 degree for misorientation calculations between two measurement points.

2.3 Pattern Formation

As already mentioned in the previous chapter, the electron beam spreads when electrons penetrate into the specimen.
All electrons which fulfill the Bragg law for diffraction $\lambda=2d\sin\theta$, *(Eq. 2-1)*, where λ is the wavelength of the electron beam, d is the crystal plane spacing and θ is the diffraction angle, are travelling on the surface of a cone with its axis perpendicular to the diffracting plane. This cone of diffracted electrons is generally called the Kikuchi cone.
As can be seen in Fig. 2-4, there are two cones of diffracted electrons for each crystal plane, one consisting of electrons diffracted by the front side of the crystal plane, the other of electrons diffracted by the back side of the plane.

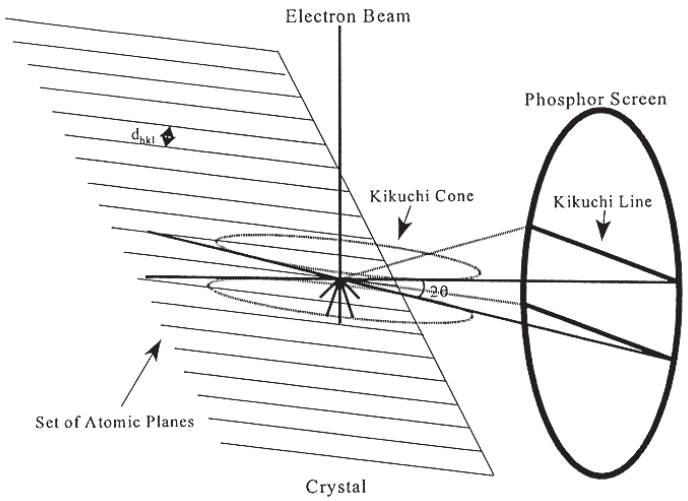

Figure 2-4 The formation of Backscattered Kikuchi lines (Krieger Lassen, 1994)

These cones will intersect the phosphor screen forming so-called Kikuchi bands, each band representing a different crystal plane. Due to the low wavelength of electrons and the resulting low diffraction angle, these bands will appear as almost straight lines. However, since the angular range of electron backscattering patterns is large (up to 90 degrees), the bending of the lines will be recognizable on the border of the screen. This kind of projection is known as gnomic projection. When using the model of a reference sphere, the center of the reference sphere is the projection point for this projection. For EBSD this is the point where the beam hits the specimen. This point will be the source of all Kikuchi cones forming the Kikuchi bands on the screen. The projection plane is the tangent plane at the north pole of the reference sphere, which corresponds to the phosphor screen in EBSD.

As can be seen in Fig. 2-3, the diffraction pattern in EBSD consists of bright bands only, unlike the Kikuchi patterns in TEM, which consists of bright and dark lines. Contrast formation in EBSD is due to the channeling effect, which means that when electrons are travelling into certain directions in the crystal, they travel between the crystal planes without being backscattered.

If treating electrons as particles, as it is done in Fig. 2-5, the channeling effect is easy to understand. This explanation, however, is misleading.

It would predict a lower intensity of backscattered electrons in directions where electrons travel almost parallel to the reflecting planes. This is, however, not the case as can be seen in Fig. 2-3, since the Kikuchi bands are bright with a dark border.

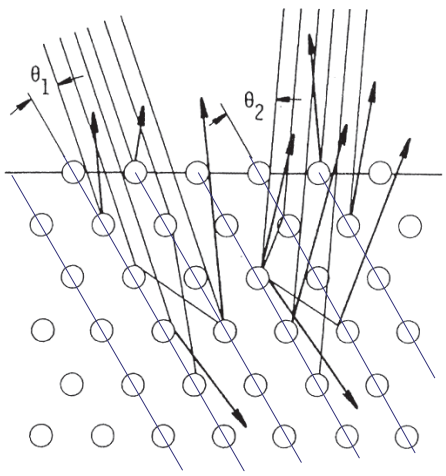

Figure 2-5 Schematic representation of the channeling effect (Semprimoschnig, 1996).

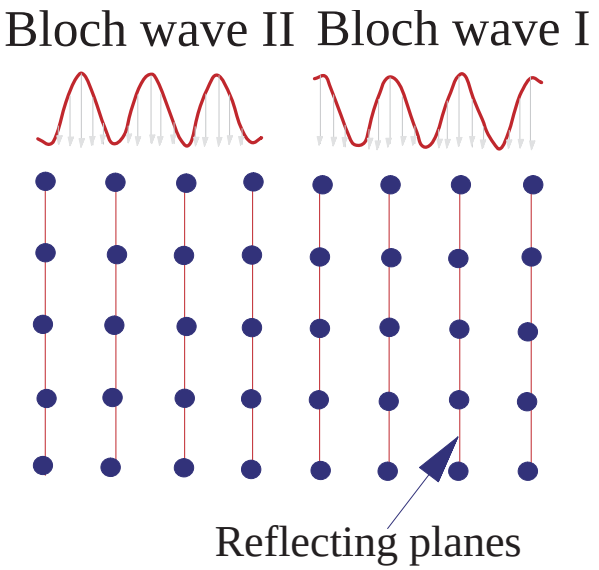

Figure 2-6 The two Bloch wave types (Joy, Newbury & Davidson, 1982).

Using the wave model of electron diffraction this effect becomes more clear.

When electrons travel through the crystal lattice, they can be mathematically described by standing waves, so-called Bloch waves. For each position in the crystal, the square of the amplitude of the Bloch wave represents the probability of meeting an electron there. In the same manner it can be understood as a local current density.

Each electron wave consists in principle out of two basic types of Bloch waves, one with its intensity maxima lying half way between the lattice planes (type II) and the other with its intensity maxima exactly at the cores of the atoms making the reflecting crystal plane (type I) (see Fig. 2-6). The sum of the local current densities is constant for all electrons, independent on its moving direction. But the ratio between the two principal Bloch waves (type I and type II) vary for different incident angle.

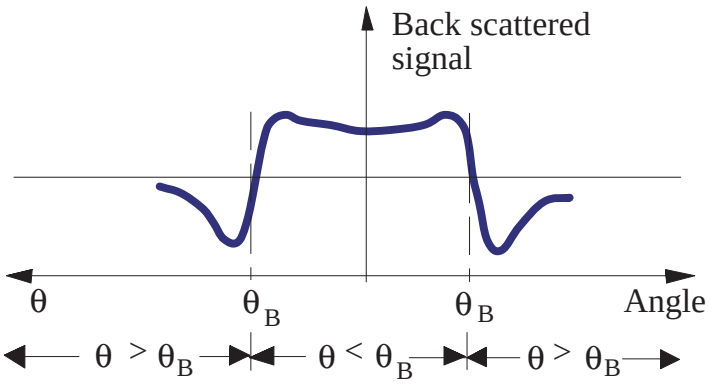

Figure 2-7 The backscattered signal depending on the angle between crystal plane and electrons (Joy, Newbury & Davidson, 1982).

An electron travelling at an angle smaller than the Bragg angle with respect to the reflecting crystal plane will consist mostly of the type I Bloch wave. Since the local current density at the atom cores is high, they interact strongly with the atoms and more electrons will become backscattered. Electrons travelling at an angle higher than the Bragg angle consist to a higher extend of the type II Bloch wave and therefore their interaction with the atom cores is not so intense and fewer electrons will be backscattered (Fig. 2-7).

Some of the Kikuchi bands in the pattern are brighter than the others. Also not every crystal plane will give a Kikuchi line. This behavior differs from crystal system to crystal system and is dependent on the structure factor F. The structure factor describes the contribution of the whole unit cell to the diffracted intensity. The position of the atoms in the unit cell as well as the chemical composition will be taken into account.
For example, in a body centered cubic crystal structure {001} planes and {002} planes (built of the atoms at the (½, ½, ½) positions) reflect electrons at the same Bragg angle, but the two reflected waves have a path difference of $\lambda/2$ and will interfere destructively and the intensity of the diffracted beam will be zero.
The intensity of the band is approximately proportional to the square of the structure factor.

$$I \propto \left|F_{hkl}\right|^2 = \left[\sum_i f_i \cos\left[2\pi\left(hx_i + ky_i + lz_i\right)\right]\right]^2 + \left[\sum_i f_i \sin\left[2\pi\left(hx_i + ky_i + lz_i\right)\right]\right]^2$$

(Eq. 2-2)

In Eq. 2-2 the summation is done over every atom i in the unit cell. The atoms are described by their position ($x_i y_i z_i$), (hkl) are the Miller indices of the crystal plane and f_i is the atomic scattering factor. The atomic scattering factor increases with increasing atomic number and decreases with increasing scattering angle, therefore it also depends on the crystallographic plane and its interplanar spacing *(Kuokkala, 1995)*.

2.4 Calibration Routines

When measuring a crystal orientation, the reference coordinate system has to be selected. In many cases it is convenient to use the sample movement axes in the microscope as reference axes, but also specific directions of the sample can be selected. For example in the case of a sheet material, the crystal axes can be expressed relative to the rolling direction (RD), transverse direction (TD) and normal direction (ND).

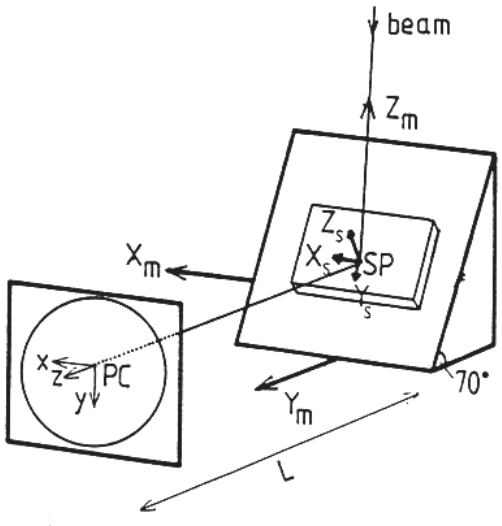

Figure 2-8 Definition of screen, microscope and specimen coordinate systems (Randle, 1992).

Three different coordinate systems generally used in EBSD studies are presented in Fig. 2-8. These include the coordinate system of the phosphor screen (x, y and z), the microscope (X_m, Y_m and Z_m) and the specimen (X_S, Y_S and Z_S.)

Additionally the sample reference axes are taken into account. In the case of a rolled sheet, one would like to determine the crystal orientations relative to the sample reference axes RD, TD and ND. Therefore the specimen has to be mounted into the microscope so that the relationship between sample reference axes and specimen axes is known. RD, TD and ND are often set parallel to X_S, Y_S and Z_S, respectively, when studying the cross-section of the sheet, it is, however, necessary to mount the specimen differently on the specimen holder.

The specimen tilt angle with respect to the electron beam, the position of the phosphor screen relative to the microscope axes, as well as, how the specimen is mounted into the specimen holder must be specified as an input for the computer program carrying out the indexing.

There are, however, three parameter necessary for the indexing that have to be determined by a calibration procedure. These are the position of the pattern source point SP on the specimen surface, the position of the pattern center PC on the screen and the specimen to screen distance L.

For an EBSP all diffracted electrons will have their origin in principle at one point on the specimen surface. This is the pattern source point SP, *i.e.*, the point where the electron beam hits the specimen, defined by the position of the electron beam and the working distance. It is also the origin of the specimen coordinate system. The pattern center PC on the phosphor screen is defined by the intersection point of the screen with a line going through the pattern source point SP and being perpendicular to the screen. This is the origin of the screen coordinate system. The specimen to screen distance is the length between the pattern center, PC, and the pattern source point, SP.

Several different ways have been used to determine the pattern center and the specimen to screen distance.

For example, *Venables & Bin-Jaya (1977)* used the so called three ball method, where three steel balls are mounted in front of the screen, producing elliptical shadows on the screen. The geometry of these shadows is then used to calculate the necessary calibration parameters. A fairly similar method is the so-called mask method presented in

the same publication. Here a rectangular mask is placed in front of the phosphor screen producing again a shadow image. The geometry of this shadow is used to determine the specimen to screen distance as well as the pattern center. However, these methods are not anymore in common use.

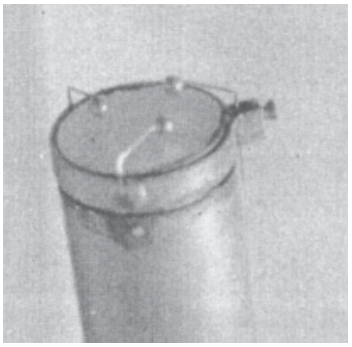

Figure 2-9 EBSP detector with the three steel balls mounted in front of the phosphor screen (Venables & Bin-Jaya, 1977).

A very frequently used method is the so called 'known orientation' method.

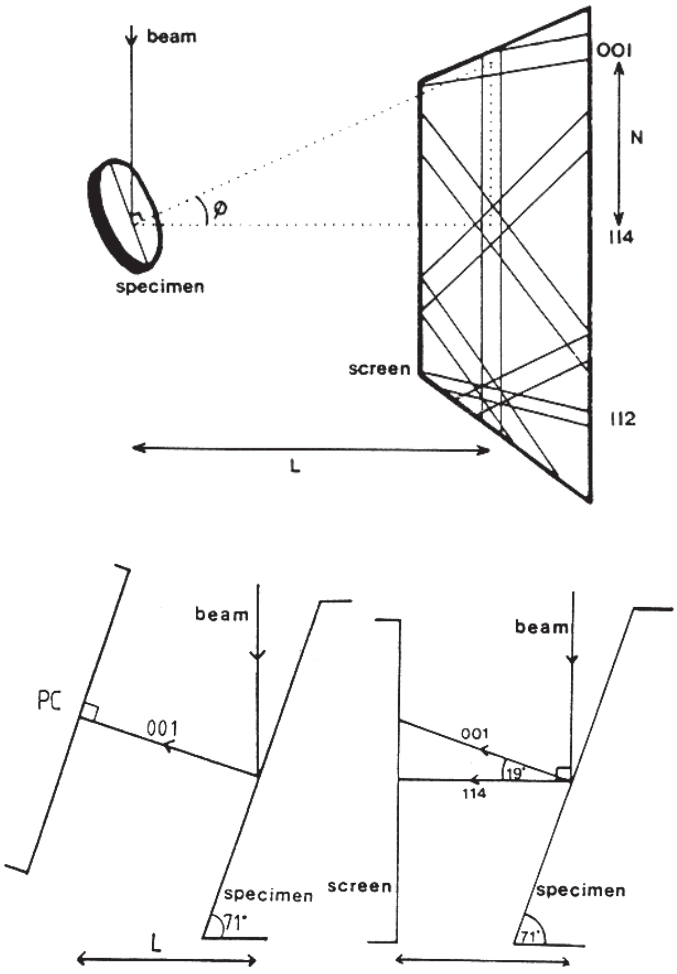

Figure 2-10 The principles of the 'known orientation method' are displayed. a) shows the principle specimen configuration in the microscope. In b) two different screen positions are displayed (Randle, 1992).

A single crystal with known orientation is mounted into the microscope. Usually a silicon crystal having a surface normal of [001] is used. If the crystal is mounted so that the X_S axis is parallel to [1$\bar{1}$0], the [1$\bar{1}$0] direction will be parallel to Y_S. In the diffraction pattern the Kikuchi band of the [1$\bar{1}$0] direction will be parallel to the y axis. On this band four prominent poles of the diamond crystal system can be found, *i.e.,* the [111], [112], [114] and [001] pole.

The angle between the [114] and [001] poles is 19.5 degrees.

If a specimen tilt angle of 70.5 degrees is used, the [114] or the [001] pole is the pattern center PC, depending on the phosphor screen position relative to the specimen (Fig. 2-10). The specimen to screen distance can be determined from the distance of [114] and [001] poles on the phosphor screen.

Since the pattern source point is the origin of all Kikuchi cones and all zone axes, it is also the projection center of all poles. When the phosphor screen is moved towards the specimen, all poles will move towards the pattern center, since this represents the projection center on the screen.

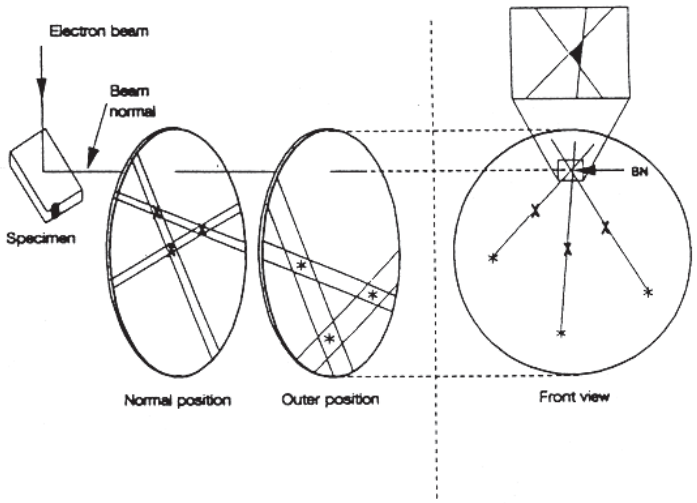

Figure 2-11 Two position method (Randle, 1992).

An other easy calibration method, known as the 'two position method', is based on this idea (Fig. 2-11). Two diffraction patterns using different specimen to screen distances are taken, the nearer specimen to screen distance will be used for the measurements. The same three poles have to be indicated in both patterns. The projection center for these poles is the pattern center. The specimen to screen distance can be calculated if the difference between the two specimen to screen distances is known.

2.5 Automated Crystal Orientation Determination

An experienced operator can make about 50-100 measurements in one hour, depending on the system and on the type of the measurement. If one wishes to map a specimen area and to make a measurement on each grain, it will take longer time than by just moving the stage stepwise and making the measurement on current position.
The development of fully automated systems allows conduction of several thousands of measurements in just a couple of hours. Investigations which were earlier very time consuming using semiautomatic indexing can now be performed within a short time.

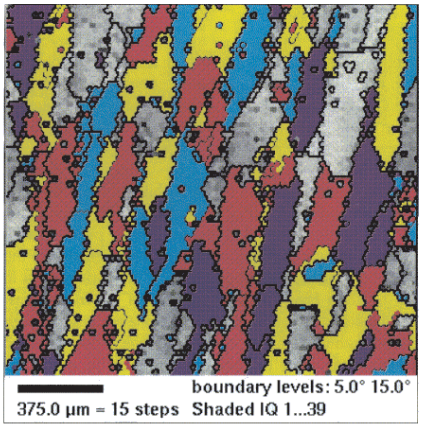

Figure 2-12 Orientation imaging microscopy™ (OIM™) map (TSL).

The beam or the stage moves by a given stepsize, scanning the whole specimen area. At each point a pattern is taken and indexed fully automatically. Fig. 2-12 shows an example of a map produced by such an automatic system. The different colors indicate a different misorientation angle range from the cube texture (001) [100]. In this picture the step size was 25 µm. A hexagonal shaped area correspond to one measurement. This can be seen on the jaggedness of the grain boundaries. In the figure several single measurement points show a different orientation than the surrounding ones. These are probably not real grains. The automatic system is not able to index all patterns correctly, some are rejected and some are indexed wrong. Many of the single 'island' points represent these kind of measurements.

A line seeking routine based on the Hough transform is used to identify the position of the Kikuchi bands. This method has proven to be the most reliable one.

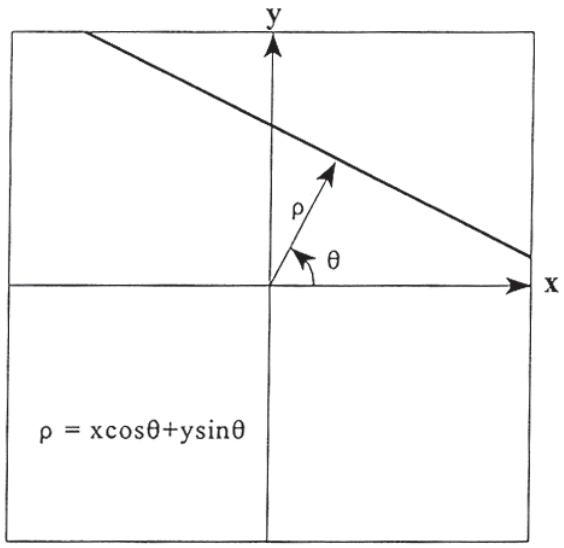

The intensity of each pixel of the pattern is determined. The Hough transform maps each pixel as a curve in the Hough space using the equation

$$\rho = x_i \cos\theta + y_i \sin\theta. \qquad \textit{(Eq. 2-3)}$$

where x_i and y_i are the coordinates of the ith pixel and θ takes all values between 0 and π (see Fig. 2-13 for definition of ρ and θ).
Each pixel in the pattern will correspond to one curve in the Hough space which has the same intensity as the pixel.

Figure 2-13 Illustration of the parameterization of lines. Each point is defined by the distance ρ and the angle θ (Krieger Lassen, 1994).

If several points are on a line, their curves in the Hough space will intersect in one point. This can be seen in Fig. 2-14. All points of the bright Kikuchi band in the pattern will be transformed to curves having a high intensity in the Hough space. These curves will intersect in one point and since the intensities are added, a bright point, representing the Kikuchi band, can be seen in the Hough space (Fig. 2-15).

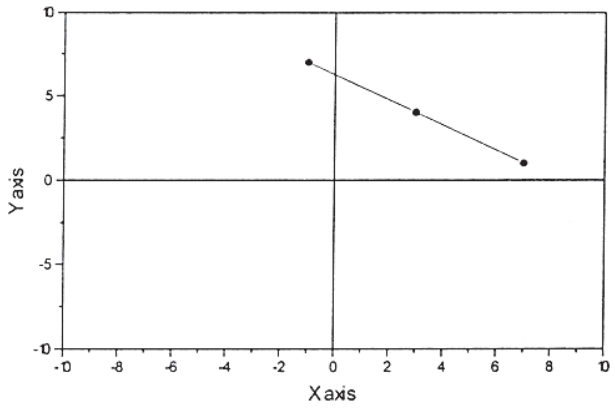

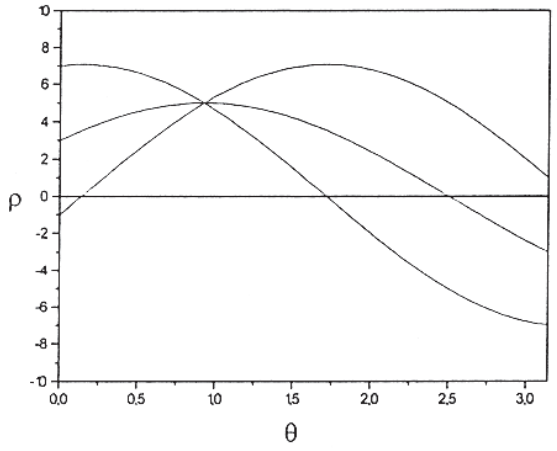

a) *b)*

Figure 2-14 This figure shows, how three colinear points are transformed into three at one point intersecting curves in the Hough space. In a) the three colinear points can be seen. Their Hough transform is shown in b) (Krieger Lassen, 1994).

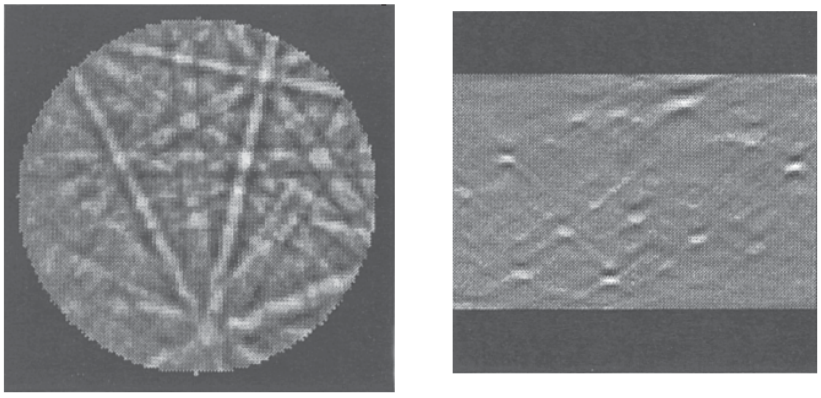

a) b)

Figure 2-15 The principle of the line seeking routine by the Hough transform is shown. a) shows the EBSP from pure copper. b) is its Hough transform The Kikuchi bands can be recognized as points (Krieger Lassen, 1994).

2.6 Specimen Preparation

The relatively easy specimen preparation is one of the advantages of the EBSD system compared to SAC or TEM based techniques. A TEM specimen has to be a thin foil to be transparent to electrons, while SAC requires a carefully electropolished flat surface.
The main requirement in EBSD specimen preparation is the removal of any surface deformation or contamination layer. Because the backscattered electron emission depth is so low, about 20 nm, any surface layer has to be removed. Deformation will blur the Kikuchi bands or even cause that no EBSP can be obtained. Contamination, like oxide layers might be thick enough to contribute to the electron diffraction. No Kikuchi bands, a double image containing information of the contamination layer and the base material as well as an EBSP just of the contamination layer could be the result. A completely flat surface, however, is not required.
Conventional metallographic specimen preparation like grinding and mechanical polishing are generally used for initial specimen preparation. But the surface deformation introduced by grinding and mechanical polishing is too high to obtain a diffraction pattern. Therefore, as a last step, the surface deformation has to be removed by chemical etching or electropolishing.
In some cases, the final preparation step after grinding is mechanical polishing in a colloidal silica suspension, for example lead or different metal carbides (M_7C_3 and M_3C) were prepared by this method *(Dingley, Baba-Kishi & Randle, 1995)*.
Ion milling is one additional possibility to remove the deformed surface layer, the prepared specimen area is, however, very small, thus this method is not even mentioned in most specimen preparation guides.
To produce a fresh and undeformed surface by fracturing or cleaving a brittle material is a further specimen preparation possibility. Fracture surfaces are generally not flat. Still, they can be studied with EBSD. Problems can arise due to shadowing of the specimen surface. Altering the specimen tilt angle and rotating the specimen allow to obtain patterns of most of the specimen area.
However several materials will give a diffraction pattern readily without any particular specimen preparation needed, for example silicon, GaAs or α-Al_2O_3 *(Dingley, Baba-Kishi & Randle, 1995)*. An other example is a the zinc coating of a steel plate.

3 Application of EBSD in Materials Science

EBSD is a very powerful technique for materials scientists. It allows to measure the crystal orientation while observing the topography of a bulk specimen with SEM and having the possibility to analyze the chemical composition with EDS.
The use of all these techniques opens new possibilities for materials scientists to improve the understanding of materials' properties.
This chapter gives a brief introduction to the possibilities of the EBSD technique and provides a literature review for new users.
In principle there are four main application areas for the EBSD technique; crystal orientation measurements (microtexture), grain boundary studies (mesotexture), phase identification and strain measurements.

3.1 Crystal Orientation Measurements

3.1.1 Microtexture

If the grains in a crystalline material are aligned preferentially, the material is said to have a preferred orientation or a texture. Since many of the mechanical and physical properties of materials depend on crystal orientation, textured materials have anisotropic properties. Texture may develope into a material during processes like deformation, recrystallization, thin film deposition and solidification. Texture research is an important field in the materials science, since texture control can be used to alter the material properties.
For example, optimal properties of electrical steels as well as optimal deep drawing properties of sheet materials are achieved by texture control.
Usually X-ray measurements and to some extent also neutron diffraction are used for texture characterization. In both of these techniques many thousands or tens of thousands of grains contribute to the measurements, and thus only the average texture of the bulk material can be obtained.
To understand the material properties in more detail, it would be important to know also the spatial distribution of texture in a sample. The properties of a material will be namely different if the grains, having a preferred orientation, have clustered or if they are randomly distributed. Furthermore a correlation between grain size and crystal orientation can give valuable information as well as the correlation between different phases and texture does.
Processes like deformation and recrystallization can be understood better if local crystal orientation is known.

This field is known as 'microtexture', since it combines the microstructure and the crystal orientation.
TEM based diffraction techniques were widely used for local orientation measurements, but the small sample area and the difficulties in specimen preparation limit the number of orientation measurements. Additionally it is difficult to correlate the crystal orientation with respect to the specimen reference system.
Also X-ray diffraction techniques can be used to determine the microtexture. This can be done by back reflection Laue system using microbeam X-rays, Kossel X-ray diffraction or synchrotron white beam X-ray topography technique. The first two of these are today fairly seldom used. The back reflection Laue method requires a grain size of about 1 mm and therefore it is not applicable for most of the engineering materials. Kossel diffraction suffers from the relatively low spatial resolution of about 10 µm and of the requirement to record the pattern on a photographic film. With the synchrotron white beam X-ray topography crystal orientation from a region of a few microns can be measured, however a synchrotron X-ray source is required *(Randle, 1992)*.
The SEM electron diffraction techniques like EBSD give the possibility to measure several hundreds of grains within a reasonable time and to map the crystal orientation in the micrograph. Therefore it is a valuable tool for microtexture studies in addition to X-ray macrotexture and TEM orientation measurements.
An example for microtexture studies is the work of *Schwartz, Lassila & LeBlanc (1998)* about the effect of tungsten addition on the microtexture and mechanical behavior of tantalum plate. They found a strong through thickness <111> texture variation in the unalloyed tantalum plate. The tungsten addition changed the texture to a <001> type and through thickness variation was not strong anymore. They suggested that this textural through thickness variation causes an anomalous hourglassing in the unalloyed tantalum compression samples.
In the field of microelectronics the microtexture of interconnect lines processed from aluminium thin-film structure was investigated by *Field & Dingley (1995, 1996),* where a strong {111} fiber texture is desirable. Grain boundaries tend to be aligned with their surface normal perpendicular to the normal axis of the thin film for energetic reasons. This effect and a strong {111} texture lead to a narrow range of possible grain boundary structures, and this in turn results in a more uniform variation of grain boundary properties, inhibiting certain damage processes in the interconnect lines.
A lot of work has been done to increase the understanding of deformation and recrystallization texture development.
One of the main advantage of the EBSD technique is that it allows to carry out crystal orientation measurements prior to deformation or recrystallization and to investigate the same area after appropriate treatment. The specimen area of interest can be quite easily recognized again if a grid of microhardness indentations is made prior to the measurements.
In recrystallization studies, one can distinguish between deformed and already recrystallized grains because the quality of the EBSPs depends on deformation. The quality of a pattern is, however, fairly difficult to define, and therefore an other way is also used to distinguish between deformed and recrystallized grains. Since deformation introduces lattice defects into the crystal, orientation changes within a grain will take place. However, within a recrystallized grain the pattern will be approximately the

same within the whole grain. These two methods are also applied in automatic systems *(Wright, Dingley & Field, 1996).*

One of the first areas where EBSD technique was used very successfully was recrystallization texture studies. Two rival theories had caused discussions over decades, the oriented nucleation and oriented growth theory *(Hjelen, Orsund & Nes, 1991).* The basis of the oriented growth theory is that recrystallization nuclei having a special orientation relationship to the neighboring deformed matrix do have a higher growth rate than other grains. For fcc materials, based on experiments of deformed single crystals, a 40 degree rotation about a <111> axis seemed to play an important role. The idea of the oriented nucleation theory is that nuclei, oriented in a special way, are already more frequently present in the deformed matrix.

EBSD measurements opened a new possibility to investigate nuclei formation and growth in partially recrystallized specimens, since also the specimen reference coordinates, like the rolling or drawing direction could be taken into account.

Several investigations on fcc materials were done, for example the works of *Hjelen, Orsund & Nes (1991), Engler (1996), Engler, Hirsch & Lücke (1995) , Jull Jensen (1995)* and *Miodownik, Wilkinson & Martin (1998).*

EBSD has also been used to investigate the recrystallization texture formation in bcc materials. *Samajdar, Verlinden & van Houtte (1998)* as well as *Park, Lee & Gottstein (1998)* used a new model of recrystallization texture evolution, proposed earlier by Lee in 1995 *(Park, Lee & Gottstein, 1998).* This model is based on the idea that the absolute maximum principal stress direction of deformed grains becomes the minimum Young's modulus direction of new grains, so that the release of strain energy is maximized.

Many studies on deformation and deformation texture evolution can be found in literature, for example the publications of *Cizek, Wynne, Hong Lu & Parker (1996), Driver, Theyssier & Maurice (1996), Blochwitz, Brechbühl & Tirschler (1996), Wert, Liu & Hansen (1997), Panchanadeeswaran, Doherty & Becker (1996), Liu, Hsun Hu & Hansen (1995)* and *Harris, Ebrahmi & Garmestani (1998).* For example in the work of *Panchanadeeswaran, Doherty & Becker (1996)* the orientation changes during channel die compression of an aluminium split sample were compared with predicted ones from a rate dependent, Taylor like, polycrystalline model. It was shown that most of the grains rotated in a completely different way as what was predicted by the model, and when the prediction was correct it was mostly for grains which rotated just slightly. Nevertheless, the overall texture development, predicted by the model, was quite correct.

A very interesting way to increase the understanding of deformation processes by using EBSD was presented by *Randle, Hansen & Juul Jensen (1996)* and *Davies & Randle (1997).* The orientation 'pertubation', *i.e.,* small orientation changes, within grains and near grain boundaries and triple junctions in deformed aluminium *(Randle, Hansen & Juul Jensen, 1996)* and aluminium and nickel *(Davies & Randle, 1997)* were studied. Further work is in progress focusing on the influence of crystal orientation on the degree of pertubations in pure aluminium and aluminium-magnesium cold rolled alloys. *(Davies & Randle, 1997).*

EBSD system installation on a SEM makes it possible to carry out in situ observations of deformation or recrystallization by using a straining-heating specimen stage in the

SEM. Examples for this are reported by *Weiland, Field & Adams (1995)* and *Weiland (1997).*

3.1.2 Fracture Facet Crystallography

EBSD technique can be used to improve the understanding of fracture processes by studying the crystal orientation of the details of the fracture surface.
For brittle materials EBSPs can be observed readily from the virgin fracture surface. If plastic deformation has taken place during the fracture process, a cross section, perpendicular to the fracture surface has to be prepared. This is because deformation will restrict, due to lattice defects and lattice plane bending, the formation of EBSPs directly from the fracture surface.
Since fracture surfaces are not flat, also the surface topography with respect to the specimen reference system has to be determined. This information is combined with the crystal orientation information, to obtain the crystal orientation of the fracture surface.
Sofar only a few works have been published in this field. *Semprimoschnig (1996)* has studied the cleavage fracture of technically pure iron with a combination of EBSD and a computer-assisted stereophotogrammetry. He named this method as 'crystallographic fractometry'.
Slavik, Wert and Gangloff (1993) investigated fatigue cracks in an unrecrystallized Al-Li-Cu alloy. Again EBSD and a tilt fractography method was used to define the fracture plane orientation. Only plane sections were used since fatigue fracture causes near surface plastic deformation restricting EBSP formation.
An other way to study cleavage fracture surfaces was presented by *Hjelen, Lewin & Vatne (1996).* The idea here was that the point on the phosphor screen having the highest intensity is correlated to the direction of the specimen surface plane normal (Fig. 3-1), and thus it was not necessary to use tilt fractography.

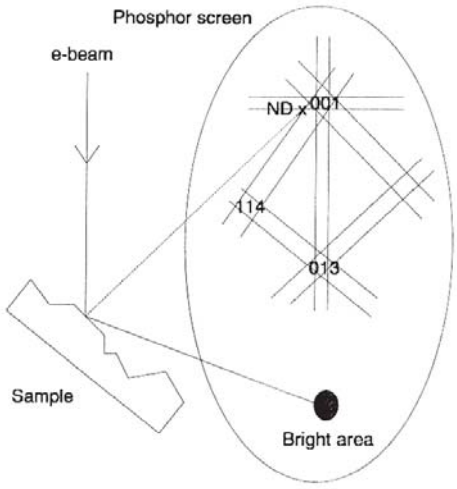

Figure 3-1 Schematic illustration of EBSP pattern and positions of brightest area and plane normal (ND) for a {001} facet plane.

A flat calibration sample with known orientation was mounted into SEM. This was used to define the relationship between the position of the plane normal and the brightest area on the phosphor screen by rotating the sample around the electron beam and tilting it around the tilt axis. The positions of the pole representing the calibration sample normal and the corresponding brightest point were mapped. This method was applied to the cleavage fracture of an Fe-0.1C-1Mn steel. By comparing the actual brightest point on the screen with the calibration, the position of the surface normal on the phosphor screen was determined. The pole on this position is the crystallographic direction of the surface normal.
The relationship between the plane normal and the brightest point on the phosphor screen seems to be materials independent.

3.2 Grain Boundary Geometry

3.2.1 Grain Boundary Design

In recrystallization studies the disorientation between deformed matrix and already recrystallized grains are often investigated. Just like in deformation studies, the disorientation between neighboring grains is important to understand in more detail the deformation process. Additionally, there is also a big interest to investigate just the distribution of disorientations between neighboring grains in a material. These studies are called as 'mesotexture' evaluation *(Randle, 1992);* studies of the texture between different grains.

It is well established that grain boundaries have a significant effect on the mechanical, physical and chemical properties of a polycrystalline material. Phenomena like intergranular corrosion, intergranular fracture or grain boundary diffusion are well known to materials scientists.

With certain disorientations two neighboring grains will fit better together than with other disorientations. These grain boundaries may have special properties, like low energy, low mobility, low tendency for segregation and high resistance against intergranular fracture and corrosion. Altering the portion of these special grain boundaries in the material by the processing route, it is possible to tailor material's properties for a special purpose. This is known as 'grain boundary design' or 'grain boundary engineering'. In this connection EBSD is a useful and often used tool for material characterization, because the geometry of a high number of grain boundaries can be determined in a reasonable time.

In these studies the coincident site lattice theory (CSL, explained in more detail in section 4.8.1) is the most widely used method to evaluate a grain boundary as special. The distribution of the different coincident site lattice boundaries and random boundaries is called grain boundary character distribution (GBCD), introduced by Watanabe in the early 1980's. He was also the researcher who brought up the idea of 'grain boundary design' *(Watanabe, 1996).*

However, the correlation between grain boundary geometry and material properties is not a straightforward question. For example in the study of *Hui Lin & Pope (1995)* about intergranular fracture in Ni_3Al, low angle and $\Sigma 3$ boundaries were found to be rather resistant against crack initiation, whereas $\Sigma 15$, $\Sigma 21$ and $\Sigma 29$ seemed to be weak grain boundaries and prone to crack initiation.

Texture is always influencing the GBCD, and thus grain boundary studies with EBSD are almost exclusively combined with microtexture studies.

A nice example for the influence of texture is given in the publication of *Watanabe, Fujii, Oikawa & Arai (1989).* Rapidly solidified and annealed Fe-6.5 wt% Si polycrystalline ribbons were investigated in this study. This material is known to have excellent soft magnetic properties, however, it is very brittle and difficult to be worked and shaped by conventional methods. The annealed material in this study exhibited a strong {001} texture and showed a high frequency of low angle boundaries (25 %), as well as, a high frequency of coincident boundaries (20%).

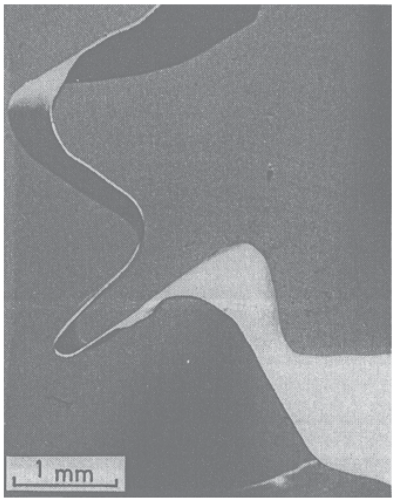

This material was very ductile and did not fracture even at 180 degree bending and irregular twisting (Fig. 3-2).

Figure 3-2 SEM micrograph of fully annealed ribbon (Watanabe, Fujii, Oikawa & Arai, 1989)

In this case the annealed material having a bigger grain size than the rapidly solidified base material, exhibited higher fraction of special boundaries because of strong texture. This is not normal, as usually the frequency of special boundaries tends to increase if the grain size decreases *(Watanabe, 1996)*. Grain size dependence of GBCD for Al-Mg alloys was for example indicated in the study of *Matsumoto, Shiayanagi & Umakoshi (1997)*.

Several applications of grain boundary design were already reported, for example the already mentioned rapidly solidified and annealed Fe-6.5 wt% Si polycrystalline ribbons. Also an increased resistance against intergranular fracture and creep in nickel could be attained by increasing the fraction of special boundaries (*Palumbo, Lehockey, Lin, Erb & Aust, 1996)*. Similar results were reported in the publications of *Palumbo & Aust (1990), Lehockey, Palumbo, Lin & Brennenstuhl (1996)* and *Palumbo, Lehockey & Lin (1997)*. Intergranular fracture was studied by *Watanabe (1993 & 1994)*. He pointed out that not just the frequency of special, against intergranular fracture resistant grain boundaries is meaningful, but additionally their connectivity does play an important role, since if a path consisting out of random, not special boundaries goes through the whole material, brittle fracture may happen. Similarly, the properties of high temperature superconductors depend on the GBCD *(Goyal, Specht, Wang & Kroeger, 1997)*.

Furthermore, different possibilities to influence the grain boundary character distribution were studied. Different strain annealing treatments were used for nickel in the work of *Thomson & Randle (1996, 1997)* to optimize the GBCD for nickel. *Watanabe, Suzuki, Tanii & Oikawa (1990)* described, that the GBCD of ferromagnetic materials can be influenced by magnetic annealing without significant change to the texture.

Also the influence of grain boundary character on precipitation may be investigated. *Caul & Randle (1996)* studied the influence of grain boundary geometry on the precipitation of Cr_2N in austenitic steel.

Numerous other studies have been done in the field of grain boundary design. As an example of these the following ones can be mentioned; *Tacikowski, Grabski, Driver & Kobylanski (1995), Mishin & Gottstein (1998), Randle, Ralph & Dingley (1988), Randle & Brown (1988), Randle & Brown (1989)* and *Furley & Randle (1991)*.

3.2.2 Grain Boundary Plane

The Coincident site lattice (CSL) model takes into account only the rotation of two neighboring grains with respect to each others but it does not include the notation of the grain boundary plane. The crystallographic orientation of the grain boundary plane influences, however, significantly the properties of a specific grain boundary and therefore CSL boundaries having irrational grain boundary plane indices may not show the special properties expected, so as high resistance against grain boundary sliding and integranular fracture.

EBSD offers good possibilities to study the crystallographic orientation of the grain boundary planes. It is, however, much more difficult to use than the GBCD technique and for this reason the number of EBSD studies in this field is very limited.

It has been observed that all fully analyzed random grain boundaries show irrational boundary plane indices, while boundary planes of coincident boundaries have often low indices *(Randle, 1995)*. The number of low index boundary planes is influenced by kinetic processes, *i.e.*, heating and cooling times during heat treatments *(Randle, 1991)*. If the number of coincident boundaries is high, it will increase the fraction of boundaries having a low index grain boundary plane, *i.e.*, low free excess volume and therefore special properties.

There are two different methods applicable to determine the grain boundary plane orientation with EBSD *(Randle, 1993)*. Both methods assume that the grain boundary plane is flat.

In the 'two-surface trace analysis' method two inclined, preferentially perpendicular to each other, surfaces are studied. On the surfaces the traces of the grain boundary must be visible (Fig. 3-3). This means that both surfaces have to be prepared metallographically to reveal the grain boundaries. One of the sides must allow the crystal orientation measurement by EBSD. Based on the EBSD result and the measurement of the angles between the specimen edge and the grain boundary trace on both surfaces, the grain boundary plane can be calculated. This method was used for example in the work of *Randle (1991)* to investigate the influence of kinetic factors of the heat treatment procedure on the distribution of grain boundary planes in nickel, as well as, in the work of *Liu, Bayerlein, Mughrabi, Day & Quested (1992)*, where intergranular crack initiation in fatigued copper polycrystals was studied. Limitation of this method is that it allows only the investigation of a few grain boundaries positioned on the edge of the two surfaces.

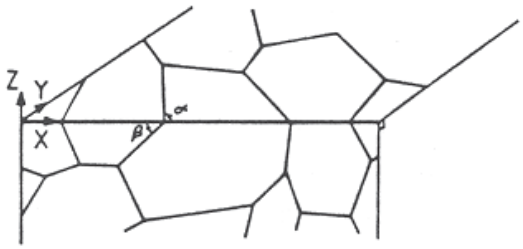

Figure 3-3 Schematic representation of the 'two surface trace analysis' method (Randle, 1993).

The second method is so-called 'serial sectioning method' (Fig. 3-4). The crystal orientations and the grain boundary trace positions are measured on the specimen surface, followed by grinding the surface to remove a layer with known thickness. Then again the position of the grain boundary traces are determined. Now it is possible to calculate the inclination angle of the grain boundary plane from the position of the grain boundary traces and the removed depth. The calibration for the depth removal as well

as for the position of the grain boundary is done by hardness indentations since the geometry of the diamond indenter is very well defined. The accuracy of the method decreases when the removed depth becomes smaller. Therefore at least 20 µm should be removed. This in turn limits the grain size of materials which can be studied by this method.
Serial sectioning method was used successfully in the work of *Randle (1995)* to study the grain boundary plane crystallography of nickel.

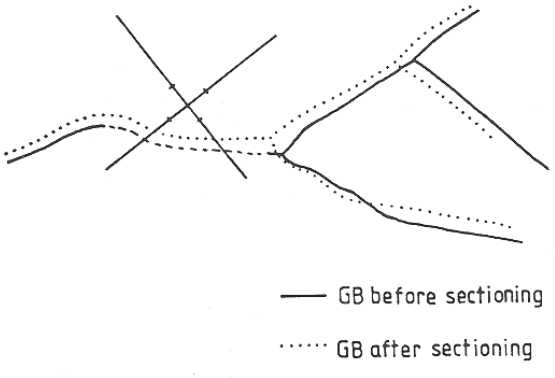

Figure 3-4 Schematic representation of the 'serial sectioning method'. The position of the cross marks the hardness indentation in the two micrographs taken prior and after removing material (Randle, 1993).

3.3 Phase Identification

The EBSD system is most widely used for orientation measurements, but its possibilities as a tool for phase identification should not be underestimated.
It is quite straightforward to use EBSD to identify known phases having different crystallography within the studied specimen. An experienced operator can make the identification just by looking at the pattern without any need for detailed indexing. This possibility is especially interesting in cases when the chemical compositions of the studied phases are fairly similar but their crystal structures are different. For example EBSD can be used to distinguish between the metal carbides M_7C_3 and M_3C, between the different iron oxides hematite, magnetite and wüstite, or simply between the bcc and fcc form of iron.[1]
Identification of unknown phases is also possible. Phase identification with EBSD is fast due to the possibility for on-line analysis, the lateral resolution of the system is fairly good, in the range of µm or even less, and as in the basic instrument SEM large specimens can be used, the identification of particles with low concentration is possible. This is a big advantage, since in TEM the specimen size is very small and thus many specimens are needed to cover a representative material volume.
Dingley, Baba-Kishi & Randle (1995) have published a diffraction pattern atlas to help microscopists in phase identification. This atlas contains patterns of 46 phases recorded on photographic film, including metals, ceramics, semiconductors, minerals and synthetic materials. They have tried to show all crystal symmetry elements in these patterns and therefore a montage of several pattern has been often necessary. This book is very useful for beginners in EBSD who are not necessarily interested in identifying patterns themselves. The atlas helps to identify the different bands and

[1] *http://www.oxinst.com/mag/educatio/ebsd/htm*

poles in the diffraction pattern, since real and schematic patterns of materials having different point groups are shown. Additionally, valuable information about specimen preparation for each phase can be found in this book.
Vatne, Karlsen & Hjelen (1996) investigated the accuracy of lattice plane spacing determination by determining the angular widths of the diffraction bands by taking an average of five measurements per band. They could show that the deviation from the theoretical value was 1.7 %, and it could be decreased down to 0.7 % by increasing the specimen to screen distance and by the use of second order diffraction bands.
A computerized method for phase identification using EBSD combined with EDS in a SEM is described by *Michael (1997)* and *Michael, Schlienger & Goehner (1997).* An automated analysis program determines the band widths and the interplanar angles in the diffraction pattern. These parameters are used to calculate the so-called sub-cell volume. The actual unit cell volume is an integer multiplied by this sub-cell volume. The chemical composition derived by EDS and this sub-cell volume are used to search for the phase in a database, in this case in the Powder Diffraction File. One phase identification takes less than 10 minutes to complete. They reported to be able to study precipitates as small as 0.3 µm in bulk materials.
The identification becomes more difficult, if the phase does not exist in the data base. However, the identification of a completely unknown phase is also very difficult with any other method.

3.4 Quantitative Strain Measurement

Plastic strain in the material will blur the Kikuchi lines, since the diffraction condition is not anymore completely fulfilled due to lattice defects and lattice plane bending. If the specimen is deformed heavily no Kikuchi bands can be recognized within a pattern.
Still, it is quite hard to define the strain quantitatively since the amount of band blurring depends, in addition to the amount of plastic strain, also on several other factors like the specimen tilt, the microscope parameters including accelerating voltage, beam current and working distance, the surface deformation due to the specimen preparation or the contamination of the specimen surface.
On the other hand, also the distribution of the lattice defects and strain in the sample does have a significant influence on the overall pattern quality. For example if dislocation cells are build up during deformation, the cell size can be bigger than the diffracting volume wherefrom the EBSP is obtained. This means that the pattern quality may change from measurement point to measurement point, since the cell interiors are virtually dislocation free.
In SEM a thin carbon layer may build up on the studied surface due to surface diffusion and electron beam cracking of hydrocarbons present in the vacuum. This contamination can be seen as black points wherefrom the EBSPs have been taken. It is often visible also as a frame if the normal scanning mode has been used at first with a high magnification and there after with a lower one. In EBSD operation these black points may serve as position markers of the measurements. They increase of course the

difficulty of quantitative strain measurement, since the pattern quality will decrease as a function of the thickness of contamination. In worst cases the pattern may disappear completely when the electron beam is kept in spot mode for a long time for EBSP recording. Author's own experience is that the Kikuchi bands in a pattern taken from a tungsten filament sample, broken in a brittle manner, disappeared after about 39 minutes, a remarkable decrease of pattern quality was visible already after about 30 minutes. The time to cause meaningful change will depend strongly on the vacuum level. For example *Buchgraber (1996)* describes, that the Kikuchi lines in the pattern disappeared within 10 minutes for copper specimens under a pressure of about 10^{-2} Pa, however, if the pressure was lowered to 10^{-3} Pa, the bands were still visible after 30 minutes.

Since many influencing factors are present, it is very difficult to give an upper limit of deformation for pattern indexing.

Strain measurements are the least established application of EBSD due to the difficulties mentioned above. However, it is an interesting possibility and therefore several researcher are working in this field. Their task is not a straightforward one, because a reliable calibration curve, which correlates strain and image quality, has to be defined.

One of the first attempts to quantify strain was done by *Quested, Henderson & McLean (1988).* They used a directionally solidified nickel-base superalloy to quantify creep strain by a 'characteristic magnification method'. Several patterns were taken while the beam was scanning different sized areas within one grain (*i.e.*, using different magnifications). The pattern quality decreased with increasing scanned area. The quality of these pattern were compared to that of an EBSP obtained with the beam kept in spot mode. A characteristic magnification could be defined for different strain levels, above which the spot and scanning mode patterns were identical in quality. They found a linear relationship between the strain level and the characteristic magnification for specimens strained parallel to the direction of solidification.

Troost (1993) defined the pattern quality by calculating the standard deviation of the pixel intensity distribution in different subsections of the EBSP. With this he created a calibration curve for strain in Si caused by Ge implantation.

Wilkinson & Dingley (1991) used a root mean square intensity of the averaged band profile to quantify the contrast of the pattern. Additionally, a Fourier transform was used to define the sharpness of the pattern. Their samples were Al alloy tensile test specimens.

In a later work these authors described the application of this method to an Al6061/SiC fiber composite. In this study the measurement results derived from EBSPs were compared to calculated plastic strain and stress distribution by a FEM model (*Wilkinson & Dingley, 1992).*

A method using microindentations and the grey level profile of Kikuchi bands was presented by *Day & Shafirstein (1996).*

An other technique to determine also small local elastic strains and lattice rotations is to measure the shift of the position of zone axes or Kikuchi bands between unstrained and strained specimens. The shift of the Kikuchi bands was used by *Troost, van der Sluis & Gravesteijn (1993)* for epitaxial $Si_{1-x}Ge_x$ layers on Si(100).

Wilkinson (1995) studied epitaxial $Si_{1-x}Ge_x$ layers on Si(100) as well. But he used the shift of the zone axes. In these measurements the angular range of the diffraction

pattern was only about 14 degrees since the specimen to screen distance was enlarged to increase the angular resolution. Wilkinson estimated that this method is sensitive to strains as small as 0.02 % and lattice rotations as small as 0.01 degree.

The shift of the zone axes is also applied by *Wilkinson, Henderson & Martin (1996)* to investigate the plastic zone of a fatigue crack in combination with electron channelling contrast imaging (ECCI). This allows to image even individual dislocation lines in SEM.

Nowadays attempts are made to use the Hough transform for strain analysis, since it is already used for automated pattern recognition[1]. The spread of the bright line intersection points in Hough space is used to define the pattern quality. Different ways to determine calibration curves for this method (or also for any other one) are described by *Baudin, Chastel & Pennelle (1997).*

[1] Lecture of Prof. Dingley

4 EBSD Data Analysis for Microtexture and Mesotexture Studies in Cubic Materials

4.1 EBSD Data

The crystallographic orientation is measured relative to the sample reference axes using the EBSD technique. The crystal orientation is expressed as a three by three matrix, the so-called orientation matrix. It contains the direction cosines of the angles between the crystal <001> directions and the sample reference axes.

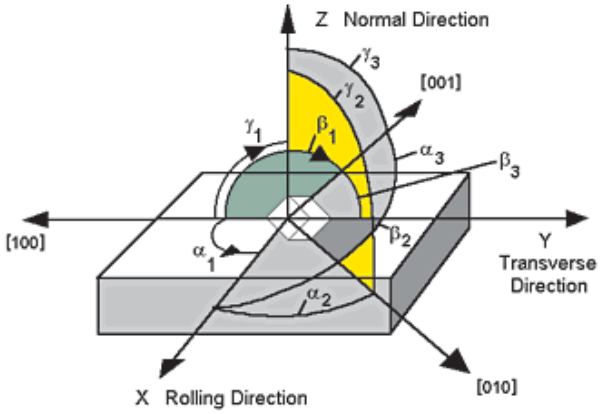

Fig. 4-1 gives a schematic illustration of this. The angles α_1, β_1 and γ_1 are those between the crystallographic [100] direction and the rolling (RD), transverse (TD) and normal (ND) direction, respectively. RD, TD and ND represent the specimen reference axes of a rolled sheet. α_2, β_2 and γ_2 represent the same angles for the [010] direction while α_3, β_3 and γ_3 for the [001] direction.

Figure 4-1 Definition of the crystal axes, the sample reference axes and the angles used in the orientation matrix.[1]

The orientation matrix A is defined as

$$A = \begin{pmatrix} \cos(\alpha_1) & \cos(\beta_1) & \cos(\gamma_1) \\ \cos(a_2) & \cos(\beta_2) & \cos(\gamma_2) \\ \cos(\alpha_3) & \cos(\beta_3) & \cos(\gamma_3) \end{pmatrix} \quad \textit{(Eq. 4-1)}$$

[1] *http://www.oxinst.com/mag/apps/notes/124.htm*

The first row in the matrix shows the [100] crystal direction expressed in sample reference coordinates. Similarly, the second and third rows contain the directions of the [010] and [001] crystal axes, respectively.
Correspondingly, the first, second and third columns of the matrix express the specimen reference axes RD, TD and ND in crystal coordinates.
These matrices are orthogonal, *i.e.*, the sum of the squares of the matrix elements is one in every row and in every column. Consequently, the determinant of an orientation matrix is +1.

4.2 Ideal Orientation

The 'ideal orientation' representation gives the expression of the sample reference axes with respect to the crystal axes as nearest Miller indices. One or two reference axes are used depending on the sample itself. The 'ideal orientations' of important texture components in rolled sheets provide an example for this. The cube texture is represented as (001)[100], *i.e.*, the rolling plane is parallel to the (001) plane while the rolling direction (RD) is parallel to the [100] direction. Sets of planes and directions can be used as well, for example, {112}<111> represents the copper texture. For this texture type two different ideal orientations can be identified, *i.e.*, (112)[$1\bar{1}1$] and (112)[$\bar{1}\bar{1}1$].
The 'ideal orientations' for cubic materials can be easily obtained from the columns of the orientation matrix.

4.3 Pole Figures

EBSPs represent three dimensional orientations. Many different sets of crystal planes contribute to the diffraction pattern, whereas the diffraction from just one set of crystal planes is used for X-ray macrotexture measurements.
This difference between the two methods influences the data representation used.
The result of an X-ray measurement, a pole figure, does not allow readily to perform quantitative calculations, because it represents the intensity of the diffracted beam from the chosen set of crystal planes for different beam incidence angles. An Orientation Distribution Function (ODF) has to be extracted from several different pole figures. The ODF is a three dimensional expression of the crystal orientations allowing to perform quantitative texture analysis.
Quantitative texture information, however, can be computed easily using EBSD data.
Nevertheless, a visual representation of the crystal orientations is desirable since it gives qualitatively important information, which in turn can be used as input parameters for the further data analysis.
The pole figure is an often used method due to its frequent application in X-ray macrotexture measurements. Moreover, it gives a quick impression of the orientation distribution within the sample. An experienced user can define the ideal orientations of significant texture components based on the pole figures.

Pole figures are stereographic projections of a specific set of crystal planes into a sample reference plane. The {100}, {110} and {111} crystal planes are used for cubic crystal systems.

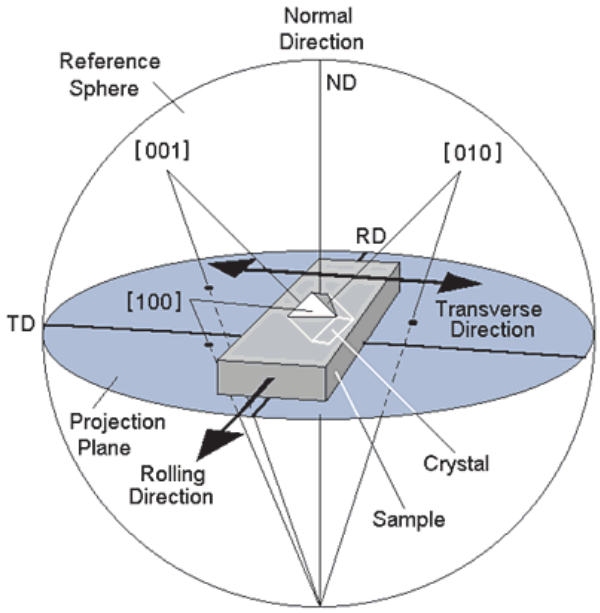

Figure 4-2 Schematic representation of the {100} pole figure construction.[1]

Fig. 4-2 shows the construction of the {100} pole figure. The sample reference axes represent the coordinate axes for the stereographic projection. The crystal unit cell, indicated by the cube, is adjusted so that the origins of the crystal coordinate system and the sample coordinate system are the same. The two coordinate systems, however, are usually rotated relative to each other. A unit sphere in the sample reference coordinate system is used for the stereographic projection. The intersection points of the <100> crystal directions with the unit sphere are projected into its equatorial plane with the south pole as the projection center.

Fig. 4-3 shows an example of a pole figure of an EBSD microtexture measurement. In this case the crystal directions are displayed as discrete points. Additionally, intensity contour line plots, similar to X-ray pole figures, can be used, especially for a high number of data and a strong texture. However, in case of a weak texture and a low number of data a representation with discrete points is more recommended.

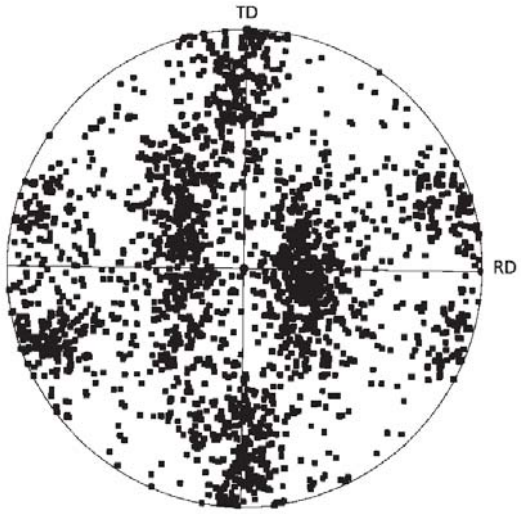

Figure 4-3 {111} pole figure of a deformed aluminium-lithium alloy.[2]

[1] *http://www.oxinst.com/mag/apps/notes/124.htm*
[2] *htpp://www.oxinst.com/mag/educatio/ebsd.htm*

4.4 Inverse Pole Figure

The 'inverse pole figure' has become the most widely used method to represent microtexture data. It displays the sample reference axes relative to the crystal coordinate system as a stereographic projection.
Of the three sample axes only one is displayed in one figure. Therefore, in most cases, three stereographic projections, *i.e.*, one for each sample axis, are presented.
Furthermore, the whole projection plane is not used but the results are presented in one unit triangle.

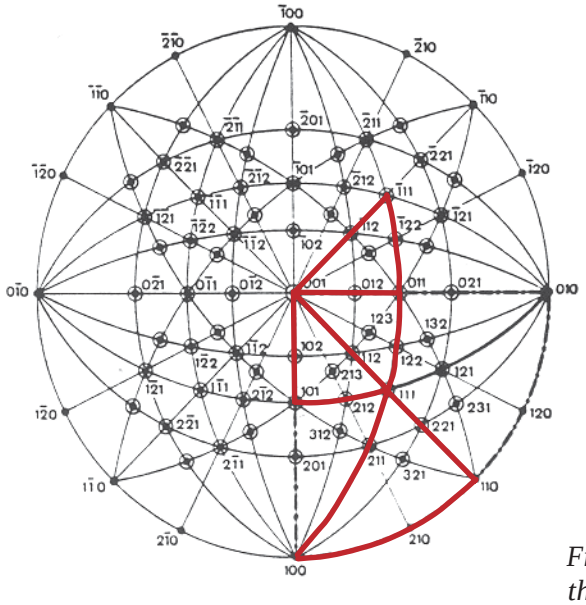

Fig. 4-4 shows the 24 upper hemisphere unit triangles for the cubic crystal system. (There are additionally 24 unit triangles in the lower hemisphere.) Four different unit triangles are used to display EBSD microtexture data, they are marked by a red border.
The unit triangle containing the [001], [011] and [111] directions is generally presented flipped about the [010] direction, looking similar to the one containing the [001], [011] and [$1\bar{1}1$] directions.

Figure 4-4 The 24 upper hemisphere unit triangles of the cubic crystal system (Randle, 1992).

4.5 Euler Angles and Orientation Distribution Function (ODF)

The Orientation Distribution Function (ODF) is a typical representation for macrotexture studies. The crystal orientation is defined by three angles, the Euler angles, which, in turn, define the coordinates of the orientation in a three dimensional space, *i.e.*, the Euler space. Generally, it is not the perspective view of this space which is used to represent the ODF but a series of two dimensional sections through the space.
This representation used to be applied also for microtexture data, but nowadays rather rarely, since inverse pole figures, pole figures and frequency charts of data having a certain maximum deviation from different ideal orientations are easier to interpret and they give the same information as the ODF does. It is, however, useful when microtexture and macrotexture data are compared.
The starting point for Euler angles is the assumption that the crystal axes are parallel to the sample reference axes. Then, the crystal coordinate system has to be rotated three times in turn to obtain the measured crystal orientation (Fig. 4-5).

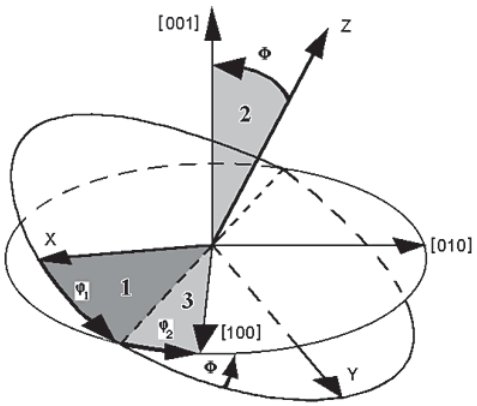

- Step 1: A rotation of φ_1 about the crystal [001] axis
- Step 2: A rotation of Φ about the crystal [100] axis
- Step 3: A rotation of φ_2 about the crystal [001] axis

Figure 4-5 Schematic representation of how three subsequent rotations specify an orientation.[1]

Fig. 4-5 describes the most commonly used specification for the Euler angles, *i.e.*, the Bunge specification. Another notation, known as Roe's specification, uses a second rotation about the crystal [010] axis instead of the crystal [100] axis.

4.6 Grain Boundaries

A grain boundary in a bicrystal has eight degrees of freedom. Five of them are known as macroscopic and the other three as microscopic ones. The three microscopic degrees of freedom are movements which occur on the atomic scale. The two bicrystal halves relax parallel and perpendicular to the grain boundary plane to minimize the grain boundary free energy.
There are two ways to describe the macroscopic degrees of freedom, *i.e.*, the 'interface-plane scheme' and the 'misorientation scheme'.

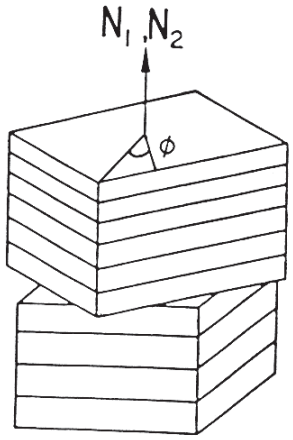

The 'interface-plane scheme' uses the normals of the grain boundary plane in each crystal (N_1, N_2). These describe four degrees of freedom, the last degree of freedom is expressed by a twist angle Φ between the two crystals (Fig. 4-6). This scheme is rarely used to describe grain boundaries in EBSD measurements, since the grain boundary plane orientation is usually unknown.

Figure 4-6 Schematic illustration of the 'interface-plane scheme'. The crystallographic planes which form the grain boundary plane are represented for both crystals. They are related by a twist angle Φ. *(Randle, 1993).*

Another way to describe a grain boundary is the so-called 'misorientation scheme'.
The grain boundary is characterized by a rotation axis [uvw] (2 degrees of freedom), which is common to both crystals, the rotation angle θ (1 degree of freedom), and the

[1] *http://www.oxinst.com/mag/apps/notes/124.htm*

grain boundary plane normal N with respect to the crystal axes of one of the two grains (2 degrees of freedom).
For EBSD the rotation axis [uvw] and the rotation angle θ can be easily calculated using the misorientation matrix.

4.7 Mathematical Description of Grain Misorientation

In principle, the orientation matrix describes the misorientation between the sample reference axes and the crystal axes. Similarly, a so-called misorientation matrix can be formulated, describing the rotation between two EBSD data. This provides an opportunity to study grain boundary geometry easily using EBSD.
There are two different ways to obtain the misorientation matrix M of two grains, with the orientation matrices A_1 and A_2 for grain 1 and grain 2, respectively.
The matrix obtained by Eq. 4-2 will describe the rotation between the two grains relative to the sample reference axes, whereas the one, obtained by Eq. 4-3, describes the rotation relative to the crystal axes of grain 1.

$$M_1 = A_2^{-1} A_1 \qquad \textit{(Eq. 4-2)}$$

$$M_2 = A_2 A_1^{-1} \qquad \textit{(Eq. 4-3)}$$

$$M_{1,2} = \begin{pmatrix} a_{11} & a_{12} & a_{13} \\ a_{21} & a_{22} & a_{23} \\ a_{31} & a_{32} & a_{33} \end{pmatrix} \qquad \textit{(Eq. 4-4)}$$

The misorientation matrix consists of nine elements representing the angle / axis pair according to the 'misorientation scheme'.
The misorientation angle θ is defined by Eq. 4-5:

$$\cos(\theta) = (a_{11} + a_{22} + a_{33} - 1) \,/\, 2 \qquad \textit{(Eq. 4-5)}$$

The misorientation axis [uvw] can be calculated by the following equations:

$$u : v : w = a_{32}-a_{23} : a_{13}-a_{31} : a_{21}-a_{12} \qquad \textit{(Eq. 4-6)}$$

$$u^2 + v^2 + w^2 = 1 \qquad \textit{(Eq. 4-7)}$$

If θ = 180 degrees then [uvw] is given by:

$$u : v : w = (a_{11}+1)^{1/2} : (a_{22}+1)^{1/2} : (a_{33}+1)^{1/2} \qquad \textit{(Eq. 4-8)}$$

Since cubic crystal systems having point group $m\bar{3}m$ have a high symmetry, one crystal direction can be expressed in several symmetrically equivalent ways, for example all <111> directions, *i.e.*, [111], [$\bar{1}$11], [1$\bar{1}$1] and [11$\bar{1}$], are symmetrically equivalent.

Consequently, the misorientation matrix is not unique, nor are the misorientation angle and axis.
All symmetry equivalent solutions can be calculated by pre-multiplying the direction by 48 symmetry matrices. 24 of them have a right-handed coordinate system, and another 24 a left-handed one. Per convention, those having a right-handed coordinate system are used for EBSD orientation matrices.

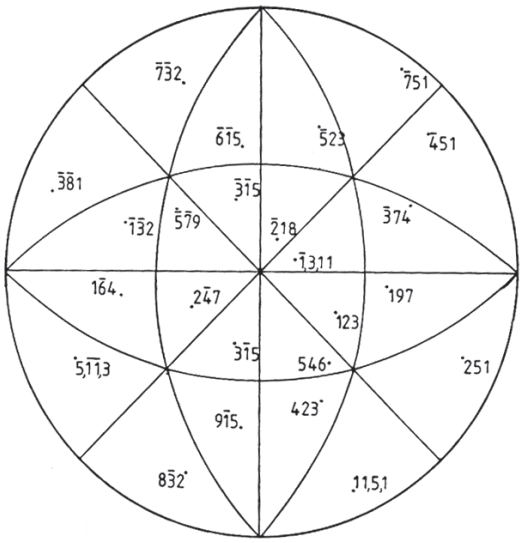

Since the orientation matrices of the two neighboring grains can be expressed in 24 different but symmetrically equivalent ways, there are 256 possible ways to calculate the misorientation matrix, and accordingly 24 different angle / axis pairs (Fig. 4-7). Per convention, the one having the smallest misorientation angle θ is usually chosen to represent the grain boundary geometry. It is referred to as 'disorientation'.

Figure 4-7 The misorientation axes for the 24 symmetry-related solutions of the angle/axis pair of a grain boundary specified by a disorientation of 50.13/[123]. Each axis falls in a different unit triangle (Randle, 1993).

The disorientation angle distribution is usually displayed as a chart, whereas disorientation axes are represented as a stereographic projection in a unit triangle, similar to the inverse pole figure.
The range of the disorientation angles extends to 45 degrees for a <100>, to 60 degrees for a <111> and to 60.72 degrees for a <110> axis, due to crystal symmetry considerations. The maximum disorientation angle in the cubic crystal system is 62.80 degrees for a $<1, 1, \sqrt{2} - 1>$ disorientation axis.
The exact disorientation angle limits can be calculated depending on the disorientation axis [uvw], where $u \geq v \geq w \geq 0$, in the following way *(Mackenzie, 1964)*:

$$\text{I: } 0 \leq \tan(\theta/2) \leq (\sqrt{2} - 1)/u \quad \text{for } \sqrt{2}\,u \geq v + w$$
$$\text{II: } 0 \leq \tan(\theta/2) \leq 1/(u+v+w) \quad \text{for } \sqrt{2}\,u < v + w \qquad \textit{(Eq. 4-9)}$$

4.8 Geometrically Special Grain Boundaries

In case of certain angle/axis pairs the two crystal lattices match better together than for random grain boundaries. These grain boundaries are referred to as 'geometrically special'. Their potential to have special properties is especially important for the concept of 'grain boundary design'.
The coincident site lattice (CSL) formalism is the most widely accepted way to recognize geometrically special grain boundaries. It is also very convenient to use in terms of EBSD data representation.
The result is represented as a frequency chart, the so-called grain boundary character distribution (GBCD).
The CSL formalism is the only grain boundary concept discussed in the present work. For more information concerning other grain boundary models, *e.g.*, the planar matching model, the O-lattice or the structural unit model, the reader may refer to *Gleiter (1982)* or *Randle (1993).*

4.8.1 CSL Formalism

The concept of the CSL theory can be understood with the help of two notionally interpenetrating lattices.
Fig. 4-8 illustrates this for two crystal lattices having the disorientation axis [uvw] and the disorientation angle θ according to the 'misorientation scheme'. Certain angle/axis pairs result in the coincidence of some lattice points from each lattice. Since the crystal lattices are periodic, these coincident lattice points will also form a periodic superlattice, *i.e.*, the coincident site lattice. The coincident site density in the volume is denoted by $1/\Sigma$. The grain boundary between these two lattices is referred to as Σ boundary. For example, if every fifth atom of two notionally interpenetrating lattices is a member of the coincident site lattice, then the grain boundary is a $\Sigma 5$ boundary.

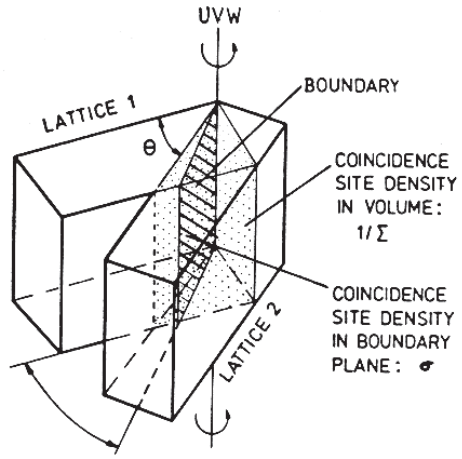

Figure 4-8 Schematic representation of the interpenetrating lattices model (Randle, 1993).

The grain boundary plane itself can consist of coincident sites only, as it is the case for a coherent twin boundary. Still, it is also possible that the grain boundary plane does not contain any of the coincident sites, even though the coincident site density is high. This can be described by the coincident site density in the boundary plane σ.

Fig. 4-9 shows a projection of a set of lattice points from two interpenetrating lattices. The open circles form the first lattice, the circles containing a dot represent the second lattice. The disorientation between these two lattices can be described by a rotation of 36.87 degrees about the [001] axis, corresponding to a Σ 5 boundary. In the figure, the [001] axis is perpendicular to the plane of the paper. Coincident sites are shown as filled circles (Fig. 4-9 a)). Fig. 4-9 b) shows the construction of a grain boundary. The coincident site lattice is represented in Fig. 4-9 c). For comparison, Fig. 4-9 d) shows a Σ 13 grain boundary, which is associated with a rotation of 22.62 degree about the [001] axis.

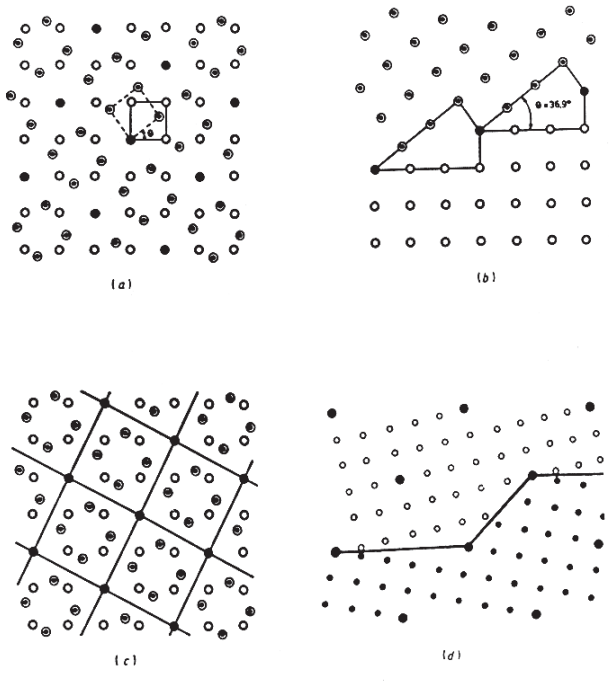

Figure 4-9 a) The projection of two interpenetrating lattices, misorientated by 36.87°/001. b) A grain boundary is generated from a). c) The coincident site lattice is shown. d) A Σ 13 boundary (Randle, 1993).

4.8.2 Physical Significance of the CSL

Due to the periodicity of the coincident site lattice and depending on the grain boundary plane the two interfaces fit sometimes more closely together than those with random geometry. These boundaries have lower free excess volume, and thus lower free energy and special properties.

Different bicrystal studies on the interfacial energy of grain boundaries showed cusps in the energy curve for geometrically special grain boundaries (Fig. 4-10). A review of the geometric criteria for low interfacial energy was conducted by *Sutton & Balluffi (1986)*.

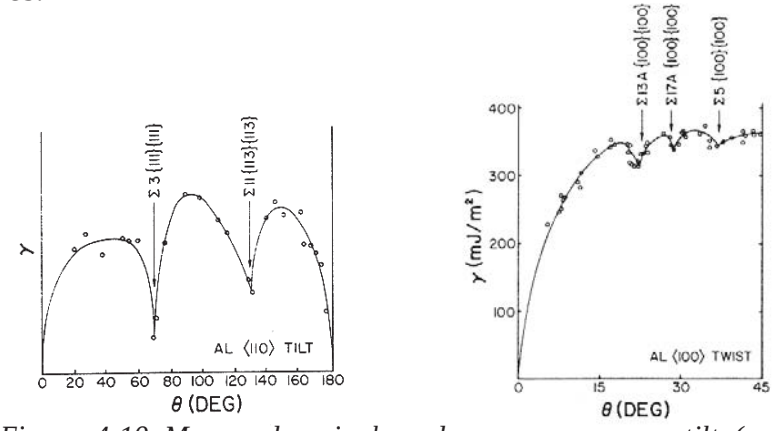

Figure 4-10 Measured grain boundary energy versus tilt (or twist) angle for a) <110> tilt boundaries in aluminium, b) <100> twist boundaries in aluminium (Sutton & Balluffi, 1986).

For example a higher resistance to intergranular fracture and grain boundary sliding can be found for CSL boundaries. However, properties like intergranular segregation and intergranular diffusion were strongly influenced by the crystallographic orientation of the grain boundary plane and other factors, *e.g.*, impurity atoms *(Priester, 1989)*. For example, the silicon segregation showed maxima at Σ 5 and Σ 13 boundaries in a Cr-Ni stainless steel. Most probably this effect is due to the other solute atoms causing a reduction in the Si enrichment at general boundaries. On the special boundaries, however, they did not segregate in the same amount, therefore Si could segregate there to a larger extent *(Lejcek & Hofmann, 1995)*.

4.8.3 Regions of Existence of Special Grain Boundaries

Grain boundaries having exactly the misorientation of a CSL boundary are scarce in a polycrystalline material.
Still, also grain boundaries close to a CSL boundary showed special properties. This is due to a dislocation network, which conserves the CSL structure on the grain boundary. These dislocations are known as secondary intrinsic grain boundary dislocations *(Randle, 1993)* and they are described similar to primary grain boundary dislocations of low angle boundaries. The Burgers vector decreases while Σ is increasing, and so the maximum allowable deviation is also decreasing.
Shvindlerman & Straumal (1985) analyzed the available experimental results related to the region of existence of special boundaries.
They found that the allowable misorientation from ideal CSL boundary decreases with increasing Σ. In addition, special properties exist only in a finite temperature interval and the upper limit of Σ number, where a grain boundary can still be regarded as special, decreases with increasing temperature (more exactly T/T_m).
The maximum misorientation may be explained by the increasing energy of the dislocation network. If the misorientation angle reaches a certain value, the dislocation energy is so high that it becomes more favorable for the grain boundary to become random. Also, with increasing temperature, another structure might become energetically more favorable, and a so-called structural phase transformation occurs *(Gleiter, 1982)*.
Different dependencies for the maximum deviation were proposed. The far most often used one is the Brandon criterion (Eq. 4-10).

$$\nu = \nu_0 \, \Sigma^{-1/2} \qquad \textit{(Eq. 4-10)}$$

where ν is the maximum deviation for a specific Σ number and ν_0 is a proportionality factor equal to the angular limit for low angle boundaries, *i.e.*, 15 degrees.
Several other criteria exist, for example to have a maximum deviation proportional to Σ^{-1}, $\Sigma^{-5/6}$ or $\Sigma^{-2/3}$.

4.9 The Rodrigues-Frank Space

Another way of representing misorientations is by using the Rodrigues vector **R.** It is defined as

$$\mathbf{R} = \begin{pmatrix} u \\ v \\ w \end{pmatrix} \tan\left(\frac{\theta}{2}\right) \qquad \textit{(Eq. 4-11)}$$

where [uvw] is the misorientation axis and θ is the misorientation angle. Since the vector has three components, R_1, R_2 and R_3, it can be displayed in a three dimensional space, the so-called Rodrigues-Frank space.
If the disorientation is chosen, all Rodrigues vectors lie in a space bounded by a truncated cube, known as the 'fundamental zone' of the Rodrigues Frank space. As a result of the crystal symmetry, it is possible to use only 1/48 of the fundamental zone to display all possible disorientations (Fig. 4-11).

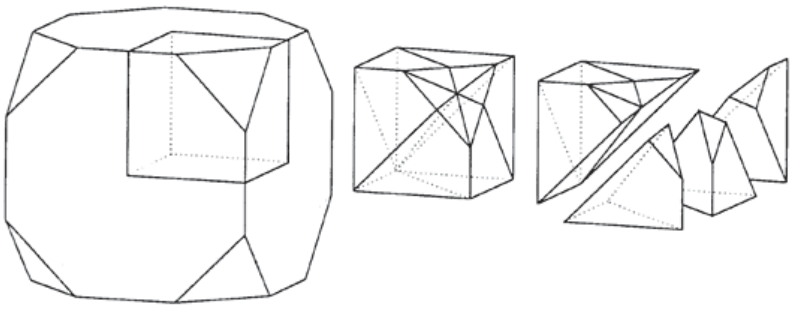

Figure 4-11 Construction of the Rodrigues-Frank space. The fundamental zone is shown on the left, the subsequent figures display the construction of 1/48 part of it.[1]

Again, two dimensional sections through the three dimensional space are used to display the disorientations.
Still, it is more straightforward to interpret a GBCD or a disorientation angle and axis distribution than the Rodrigues-Frank space. This explains why it is rather rarely used in practice. Therefore, it won't be described in more detail in this work.
In principle, it is possible to use the Rodrigues-Frank space to display orientation data, since the orientation matrix describes the misorientation between the sample reference coordinate system and the crystal coordinate system. Similarly, Euler angles can be used to describe grain boundary geometry, and Misorientation Distribution Functions (MODF) can be presented. However, both data representation possibilities are very seldom applied.
For more information on the Rodrigues-Frank space, please refer to *Randle (1993).*

[1] *http://www.oxinst.com/mag/apps/notes/124.htm*

5 The EBSD System at TUT

5.1 General System Description

The EBSD system at CEM is fully integrated into a Philips XL 30 SEM, which is equipped with a LaB_6 electron source. The microscope operating software is used to obtain the diffraction patterns, and the frame store of the microscope is used to store the images.
The phosphor screen is inclined -10 degrees with respect to the horizontal direction. A Hamamatsu C 2400-08 SIT camera is used to view the pattern. The phosphor screen can be moved together with the camera to alter the specimen to screen distance.
Furthermore, the semiautomatic indexing software COS XL Version 2.2 from TexSEM Laboratories (TSL) is fully integrated into the microscope system, the pattern as well as microscope operation parameters like the working distance are taken from the microscope control software.
The advantage of an integrated system lies in the fact that no stand-alone PC with a frame grabber card is required, since all image manipulation can be done in the microscope system.
However, the microscope frame store device is generally too slow for automatic EBSD systems and therefore no integrated automatic system exists on the market.
Fig. 5-1 shows the Philips SEM, Fig. 5-2 gives a detailed picture of the phosphor screen, the lower part of the objective lens and the SE detector in the specimen chamber.

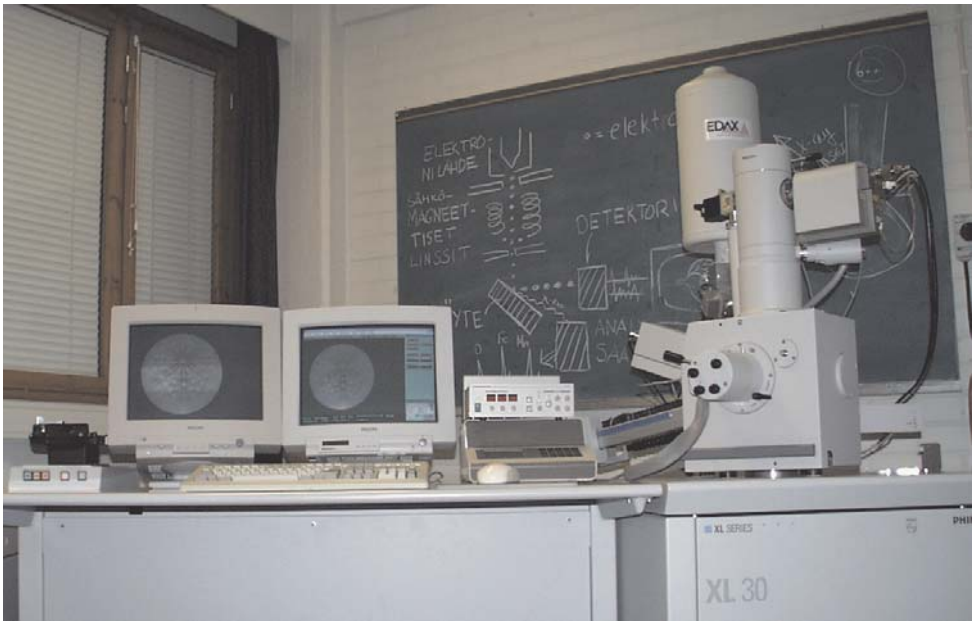

Figure 5-1 The Philips XL 30 at CEM equipped with an integrated EBSD system. The camera control unit is seen on the left side of the microscope, as well as the -10 degrees inclined camera mount and the camera.

Figure 5-2 The lower part of the objective lens (up), SE detector with collection grid and the phosphor screen.

5.2 Calibration Routines

Since the present work was the first one on this instrument, basic adjustments of the system had to be done first. Therefore, the camera inclination angle and the camera rotation relative to the specimen chamber door were adjusted in the indexing program. It is recommended to use the 'single crystal method' as a first time calibration, because this allows correction of camera lenses and computer screen distortions.

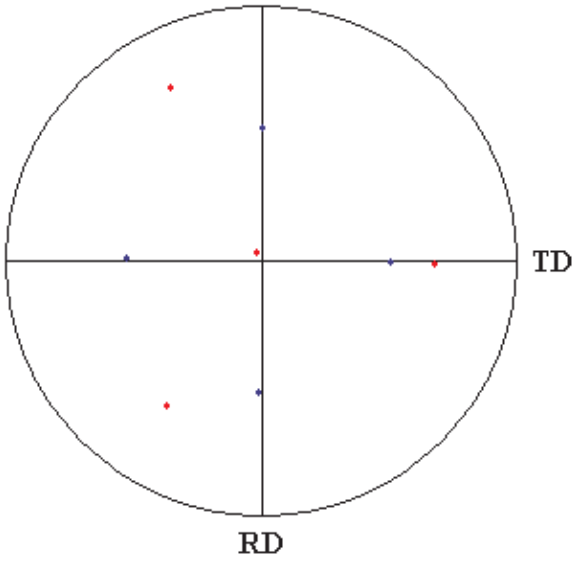

The Si calibration crystal, delivered with the system, had no (001) but a near (111) orientation (Fig. 5-3). Use of this crystal caused major problems for an unexperienced user and therefore it was decided to prepare a new calibration specimen from a Si wafer for the first calibration.

Figure 5-3 The {111} pole figure of the two Si single crystals. The orientation of the correctly aligned Si single crystal is displayed in blue, that of the original calibration crystal is in red.

The single crystal calibration method requires the substitution of the Si crystal by the sample of interest after performing the calibration procedure.

Another possibility is to use the specimen itself for the calibration applying the so-called 'two position method'. Two EBSD patterns using a known specimen to screen distance difference are recorded and used for EBSD calibration.
Since no spacer was delivered together with the system, L-shaped spacers with different widths were designed. They allow the calibration for several specimen to screen distances (Fig. 5-4). These spacers are positioned between the SIT camera and the rubber disk on the camera mount (Fig. 5-5).

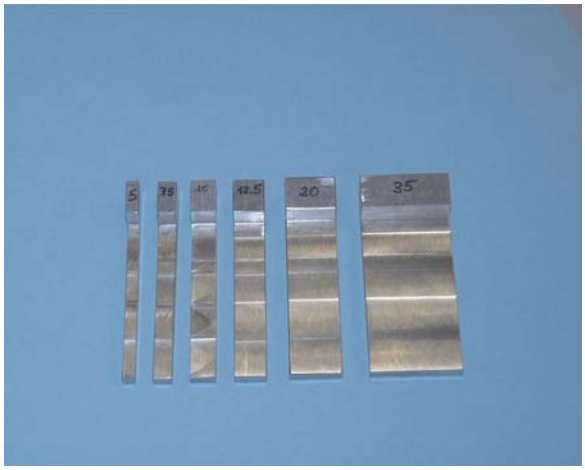

Figure 5-4 Six different spacers with the widths of 5, 7.5, 10, 12.5, 20 and 35 mm were designed for the 'two position calibration'.

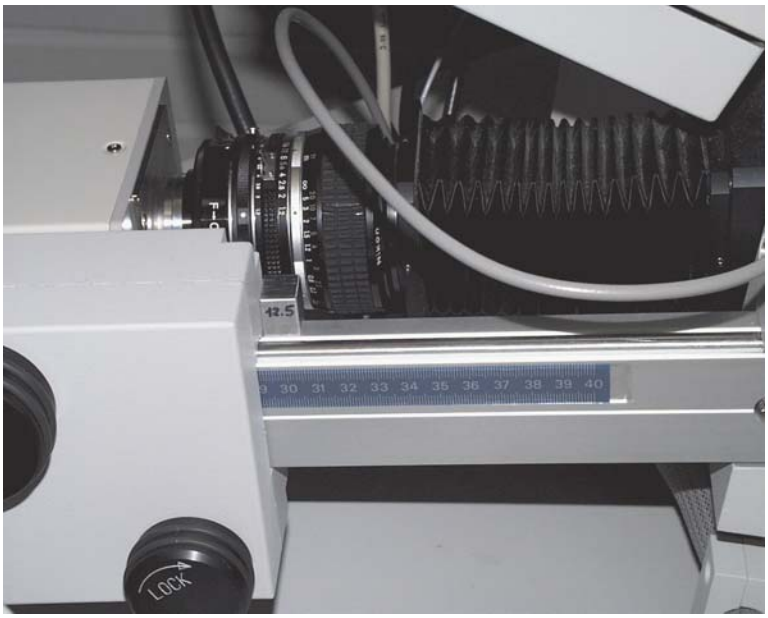

Figure 5-5 The location of the spacer in the SIT camera system. The spacer stops the SIT camera movement before the smallest specimen to screen distance is reached.

A new calibration has to be done every time when the specimen to screen distance is changed. The calibration routine, however, is fairly easy and it can be done within a few minutes.

5.3 Crystal Orientation Software™ (COS™)

The COS™ program allows semiautomatic indexing of EBSPs. The operator can choose between two methods. In the first method the operator indicates three Kikuchi bands by the mouse pointer. The software will compare the interplanar angles using a look up table to find the correct result. In the other method the operator indicates the position of two poles with known indices. In both cases a computer generated diffraction pattern will be overlaid on the pattern allowing the operator to accept or reject the suggested solution.

In addition, the software offers also the basic data analysis, *i.e.*, pole figures, inverse pole figures, grain disorientations and Euler angles. However, it is not very applicable for practical data analysis, since no statistical information is provided.
One of the main disadvantages of the integrated system is that the software does not run on a stand alone PC. Since the SEM is a frequently used instrument in materials science, it is not possible to perform time consuming data analysis on the microscope control computer.
The basic idea of the present work was the development of a stand alone analyzing software. At the beginning of this software development the angle/axis pair calculations of the new program did not give the same result as the COS™. By studying the orientation matrices it appeared that something was wrong in the indexing software. Many of the orientation matrices did have a -1 determinant, indicating that they describe a left-handed coordinate system, instead of a right-handed one. TSL confirmed that this is a bug in their software.
Experiments were conducted to understand the consequences of these left-handed matrices on the correctness of the orientation data. The same pattern (Fig. 5-6) was indexed several times by the two indexing methods available.

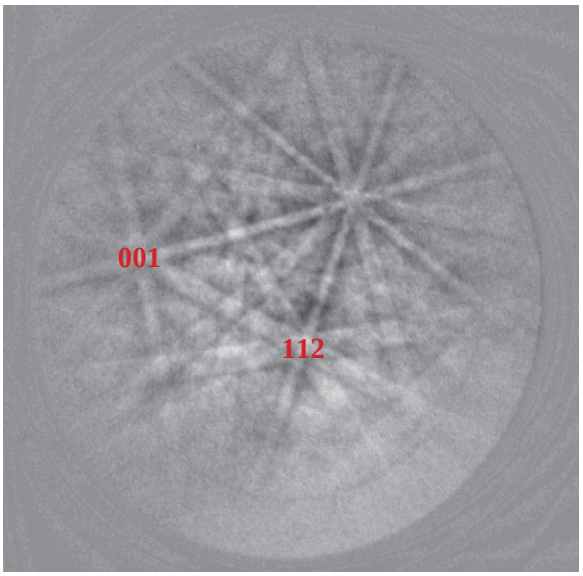

Figure 5-6 EBSP of a copper sample, used to analyze the bug in the COS™ software.
The poles of the <001> and <112> zone axes were used in the known pole indexing method.

A Kikuchi map was used to find all symmetry equivalent correct solutions for indexing this pattern. It could be shown that the left-handed orientation matrices were due to wrong pattern indexing. When the two poles indicated in Fig. 5-6 were used to index the pattern, the computer program did not accept all operator inputs. In such cases, it changed the signs of the indices of the two poles by its own resulting in an incorrect solution. Additionally, the other poles were not indexed according to the first two poles, but flipped about the Kikuchi band containing the two selected poles. Therefore, the computer generated Kikuchi pattern overlay *looked correct to the operator*.
It is not easy to define the reason for this behavior without knowing the code of the COS™ program. First it was assumed that the program tries to keep the third sample reference axes (third column in the orientation matrix) in the upper hemisphere of the unit sphere, but this was not true for all orientation matrices. Wrong indexing could

happen by changing the order of two vectors in a cross product. Mixing left and right-handed unit triangles represents another possibility.
Still, the experiments showed clearly that the left-handed orientation matrices could be transformed correctly to the right-handed ones by pre-multiplying them by one of the left-handed crystal symmetry matrices.
Because left, as well as, right-handed orientation matrices are in a data set, the disorientation of two data having different handiness is calculated incorrectly by COS™.
Moreover, it could be shown that Euler angles are incorrectly calculated independent of the handiness of the orientation matrix by calculating Euler angles and comparing them to the results of COS™. Since COS™ program can use also operator generated data, the orientation matrices of common texture components were used to verify this bug. The results of COS™ were not the same as those given in the literature.
A further disadvantage of the COS™ analyzing capabilities is the inverse pole figure. It presents only the normal direction ND and instead of a unit triangle the whole projection plane is used. This means that it is difficult to identify any texture when just a few hundred data points are available (Fig. 5-7).

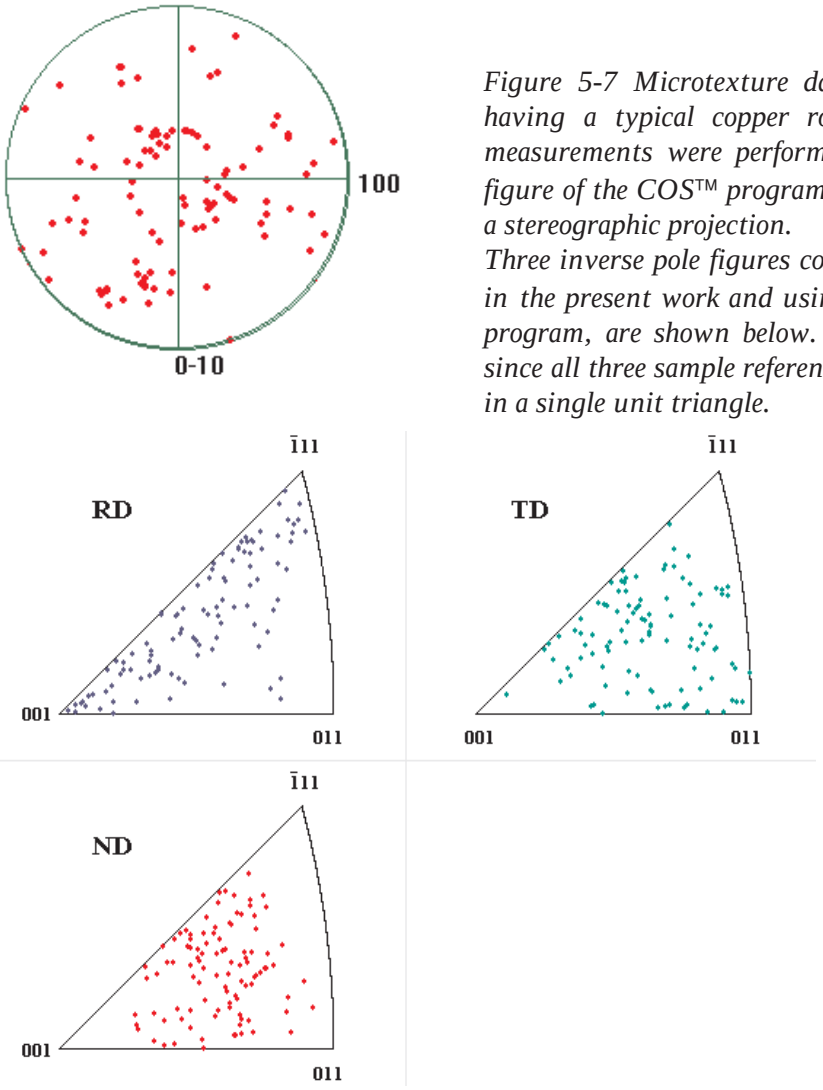

Figure 5-7 Microtexture data of a cold rolled copper sheet having a typical copper rolling type texture. Totally 100 measurements were performed. On the left, the inverse pole figure of the COS™ program is shown representing the ND as a stereographic projection.
Three inverse pole figures computed by the software developed in the present work and using the same data as in the COS™ program, are shown below. The texture is easier to identify, since all three sample reference axes are displayed, each of them in a single unit triangle.

6 Yuki - An EBSD Data Analyzing Tool

The main requirements for the analyzing software were the use of a stand alone PC system, a fast data analysis and a software which is easy to use. In addition, it was desirable that software modifications are possible and easily accomplishable.
Visual Basic 5.0 was selected as the programing language.

6.1 Analyzing Possibilities

The current version of the software is based on the symmetry operations and CSL definitions for the cubic crystal system with point group m$\bar{3}$m, allowing for the analysis of most of the important engineering materials like steel, copper or aluminum.

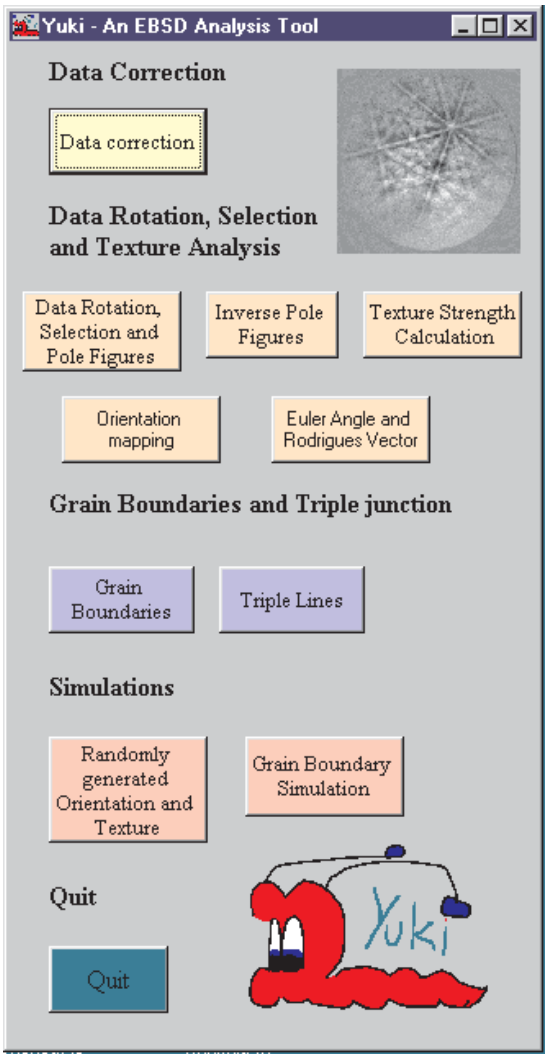

The software works with Microsoft® Excel files for data input and result output, thus making it possible to exploit Excel in further analysis. Special attention was given to provide visual output already during performing the data analysis in the form of stereographic projections and charts. Several additional results can be found in the Excel files.
Raw data, having a left-handed coordinate system, are corrected by the multiplication of the first row by -1. The user has the possibility to use pole figures and inverse pole figures for the visualization of the orientation distribution. The calculation of Euler angles and Rodrigues vectors is possible for orientation matrices, as well as, disorientation matrices between neighboring grains. The output can be used to present the data in Euler and Rodrigues-Frank space.
A texture strength calculation is also included. The percentages of data within 5, 10 and 15 degrees of an ideal orientation will be calculated.

Figure 6-1 Start window of Yuki.

One of the main advantages of EBSD lies in its possibility to correlate crystal orientations with the microstructure. To visualize this correlation, parameters of two different ways of orientation mapping are calculated. Examples for maps are shown in chapter 8.
Studies on the geometry of grain boundaries represent one of the main application areas of EBSD. Yuki allows to perform grain boundary analysis in terms of the angle / axis pair and the CSL concept for a high number of grain boundaries in a fairly short time. Also an algorithm to identify triple lines from a list of neighboring grains is included.
The GBCD is strongly influenced by the texture of the material. To visualize this phenomenon computer simulations of texture and grain boundaries can be performed.
The software is installed on 12 stand alone computers at TUT to allow easy access to the software.

6.2 Pole Figures, Data Selection and Rotation

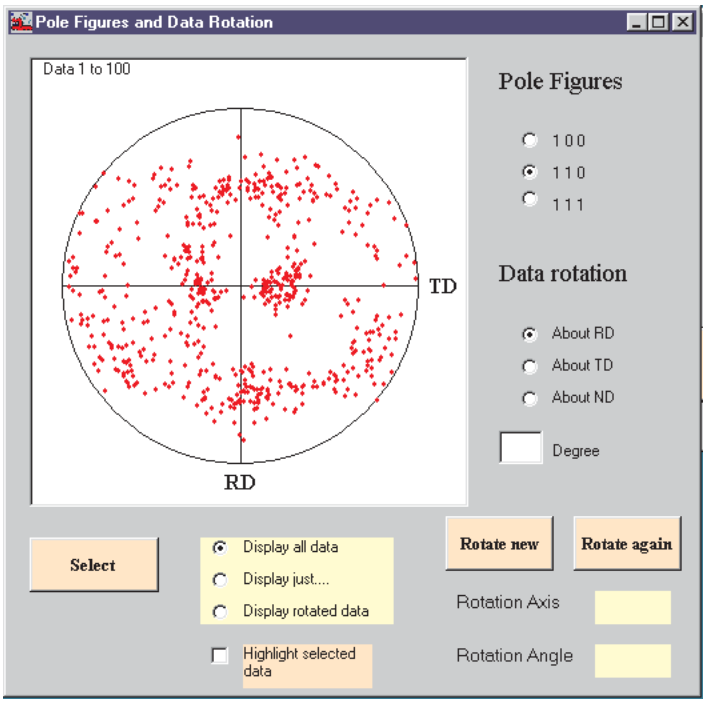

The user can choose {100}, {110} or {111} pole figures to represent the measured data. Additionally, data rotation can be performed. This possibility is very useful, in cases when the sample is misaligned. Rotated data can be used in the majority of various data analysis options. Moreover, the selection of specific data is possible.

Figure 6-2 The pole figure window. A {110} pole figure of a rolled copper sample is shown, exhibiting typical copper rolling type texture.

6.2.1 Notation of the Sample Reference Axes

The axes notations generally used for rolled sheets are the rolling direction (RD), the transverse direction (TD) and the normal direction (ND). These notations are used also in the present work.
The first, second and third columns of the orientation matrix contain the direction cosines of RD, TD and ND with respect to the crystal axes.
The code of the software allows an easy change of these notations. This is required, *e.g.*, if another type of a sample is studied.

6.2.2 Pole Figures

The direction cosines of the <100> directions are needed with respect to the sample reference axes to construct a {100} pole figure. These are given by the rows of the orientation matrix.
If a pole figure other than {100} is desired, the direction cosines of the studied direction [uvw] with respect to the sample reference axes can be calculated by using the following equations:

$$\begin{aligned} \cos \omega_1 &= a_{11}\, u + a_{12}\, v + a_{13}\, w \\ \cos \omega_2 &= a_{21}\, u + a_{22}\, v + a_{23}\, w \\ \cos \omega_3 &= a_{31}\, u + a_{32}\, v + a_{33}\, w \end{aligned} \qquad \textit{(Eq. 6-1)}$$

where ω_1, ω_2 and ω_3 represent the angles between [uvw] and [100], [010] and [001], respectively, and a_{11} to a_{33} are the nine elements of the orientation matrix.
The direction [uvw] can be plotted as a stereographic projection with the coordinates u' and v' by

$$\begin{aligned} u' &= u \,/\, (w+1) \\ v' &= v \,/\, (w+1) \end{aligned} \qquad \textit{(Eq. 6-2)}$$

6.2.3 Data Rotation

The data can be rotated about RD, TD and ND. The possibility to carry out several rotations in turn allows any possible rotation of the data.
Mathematically, these are rotations of the sample coordinate system. In practice, however, the data are rotated by this mathematical operation in the other direction than the coordinate system.
The rotation can be described by formula

$$A' = A\, M \qquad \textit{(Eq. 6-3)}$$

where A is the orientation matrix, M the rotation matrix and A' the rotated orientation matrix.
For a rotation of an angle φ about RD, TD and ND, the rotation matrices are described in Eq. 6-4, Eq. 6-5 and Eq. 6-6, respectively.

$$M_x = \begin{pmatrix} 1 & 0 & 0 \\ 0 & \cos\varphi & \sin\varphi \\ 0 & -\sin\varphi & \cos\varphi \end{pmatrix} \qquad \textit{(Eq. 6-4)}$$

$$M_y = \begin{pmatrix} \cos\varphi & 0 & -\sin\varphi \\ 0 & 1 & 0 \\ \sin\varphi & 0 & \cos\varphi \end{pmatrix} \qquad \text{(Eq. 6-5)}$$

$$M_z = \begin{pmatrix} \cos\varphi & \sin\varphi & 0 \\ -\sin\varphi & \cos\varphi & 0 \\ 0 & 0 & 1 \end{pmatrix} \qquad \text{(Eq. 6-6)}$$

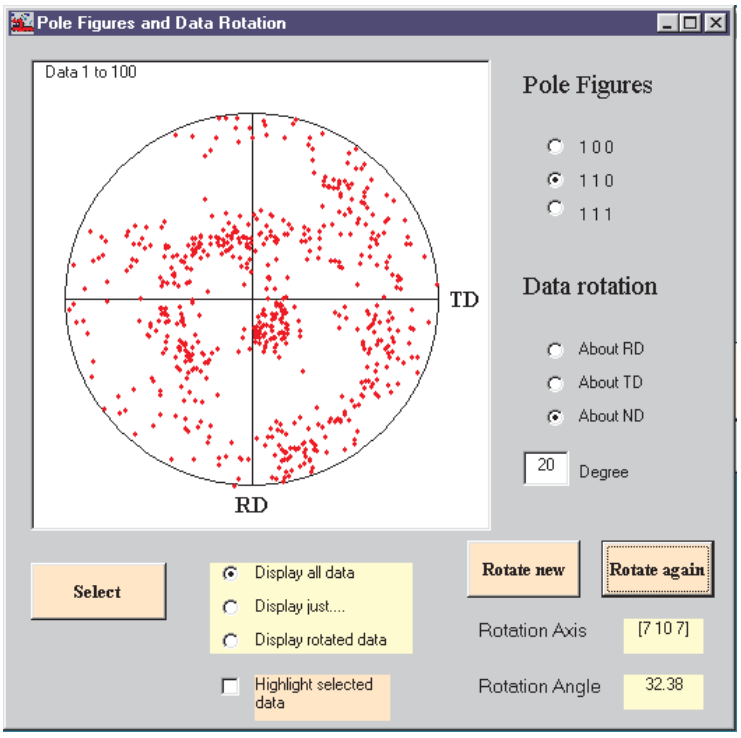

The result of the data rotation is displayed in the pole figure (Fig. 6-3). The rotation axis and the rotation angle is calculated in the same way as the angle / axis pair. A low index approximation of the rotation axis and the rotation angle is shown on the screen.

Figure 6-3 The same data as in Fig. 6-2 rotated by 32.38 degrees about the [7,10,7] axis.

6.2.4 Data Selection

Special data of interest can be selected. It is also possible to carry out different kinds of analysis for the selected data.

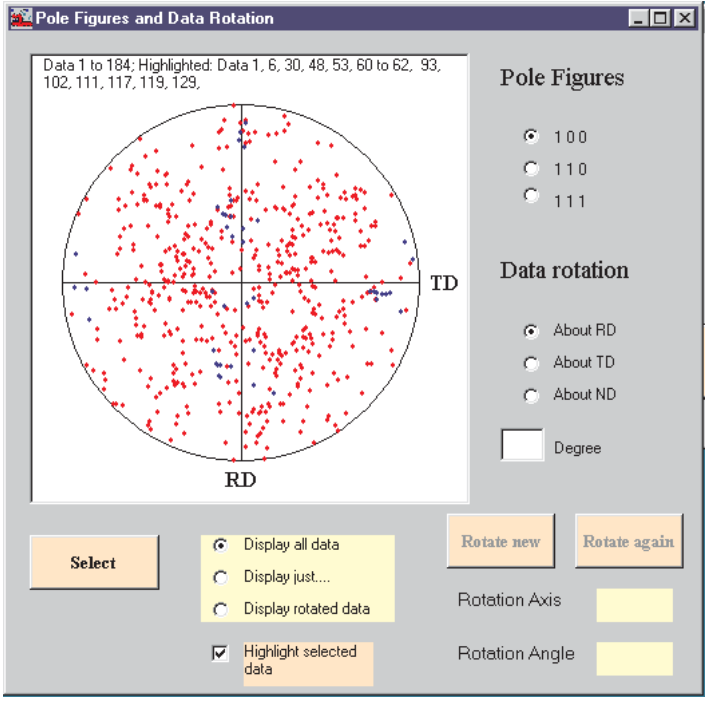

One way to display the selected data is to use different colors for pole figure plotting (Fig. 6-4).
The microtexture measurement in Fig. 6-4 was carried out on a steel sample prepared by grinding, mechanical polishing and chemical etching. Selected data, displayed in blue, represent grains which were only slightly etched. The {100} pole figure shows clearly that the etching rate is crystal orientation dependent.

Figure 6-4 Microtexture data of a hot rolled steel sheet. The selected data for slightly etched grains are displayed in blue in the {100} pole figure.

6.3 Inverse Pole Figure

Unit triangles are used to plot RD, TD and ND with respect to the crystal axes.

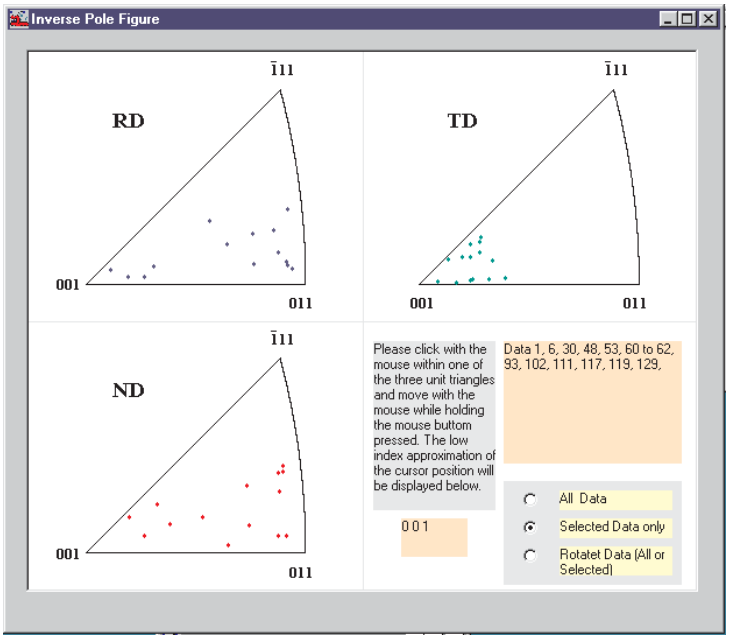

Fig. 6-5 shows the same selected data displayed already in Fig. 6-4. The strong <001> texture of the TD is easy to recognize. This microtexture measurement was carried out on the cross section of the steel sheet, having the TD as the specimen normal.

Figure 6-5 Inverse pole figure of the selected data displayed in Fig. 6-4.

To assist the user to recognize orientations in the unit triangle, a low index approximation of the mouse pointer position is displayed when the mouse button is held down. The highest index in the low index approximation has been set at 15.

6.4 Texture Strength Calculations

The EBSD data can be directly used to calculate the percentage of data within a maximum deviation from the ideal orientation. After the user has identified different fiber and sheet textures in the pole figures and in the inverse pole figures, their ideal orientations are used as input parameters for the texture strength calculation. The percentages of data within 5, 10 and 15 degrees of the ideal orientation are calculated and can be directly displayed as a frequency chart. Additionally, the grain numbers of the data with the actual deviation of the ideal orientation are given in the Excel sheet for further analysis of the microstructure, such as texture component grain size correlation or spatial distribution of different texture components.

A random reference, based on a model of the unit sphere, was developed because none could be found in the literature. The principle of this model will be outlined below.

The direction cosines of a sample reference axis with respect to the crystal axes describe a vector within a unit sphere in the crystal coordinate system. In case of a material without any preferred orientation, these vectors will be distributed homogeneously in the unit sphere. Therefore, the probability that a vector is within the volume, described by all vectors within a specific deviation from the ideal orientation, is used as a random reference.

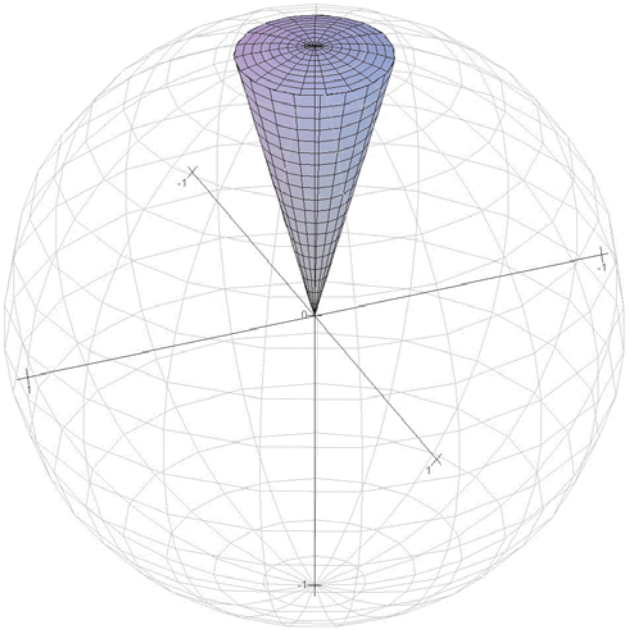

All vectors are within an angle φ from the ideal orientation, *i.e.*, in a cone with an opening angle φ. The ideal orientation is the cone axis (Fig. 6-5).

The probability for a direction to be within this cone corresponds to the volume of the cone V_2 divided by the volume of the sphere V_1.

Figure 6-5 The axis of the cone corresponds to the ideal orientation. All vectors within this cone with the opening angle φ are within an angle φ from the ideal orientation.

The volume of the unit sphere can be calculated by

$$V_1 = 4 \pi / 3 \qquad \textit{(Eq. 6-7)}$$

Correspondingly, the volume of the cone is defined by

$$V_2 = 2\pi / 3 \ (-\cos\varphi + 1) \qquad \textit{(Eq. 6-8)}$$

The probability that a vector is within this cone can be calculated by

$$p_1 = (V_2 / V_1) = (-\cos\varphi + 1) / 2 \qquad \textit{(Eq. 6-9)}$$

For a fiber texture, only one sample reference axes is textured and the other two are randomly distributed. When the fiber axis is defined, the probability for the other two axes is 1. This means that only the probability for the textured axis to be within a specific deviation from the fiber axis has to be taken into account for the calculation of the random reference.
Each crystal orientation can be described in several symmetrically equivalent ways, corresponding to several cones in the unit sphere. To define the random reference for a fiber texture the probability p_1 has to be multiplied by a factor F, describing the number of the symmetrically equivalent cones in the unit sphere. Factor F for different crystal directions is listed in Table 6-1, where letters a, b, c represent different integers.

<uvw>	F
<100>	6
<111>	8
<110>	12
<ab0>	24
<aab>	24
<abc>	48

Table 6-1 Multiplication factor F for different crystal orientations. This factor multiplied by p_1 corresponds to the random reference of a fiber texture with the fiber axis <uvw>.

The position of all three reference axes must be defined in the case of a sheet texture.

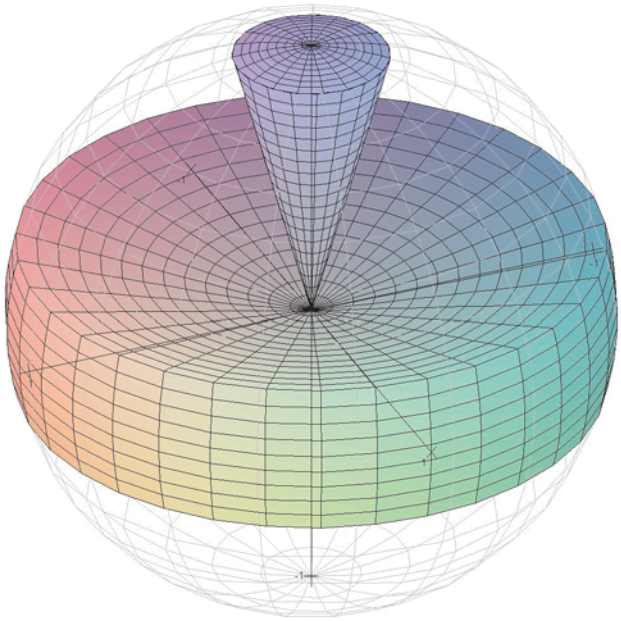

The probability for one of the three reference axes to be within a deviation angle of φ from the ideal orientation is again p_1. When the first axis is defined, the vector representing the second reference axis will be perpendicular to it. This means that it will be in volume V_3 (shown in Fig. 6-6), containing all vectors perpendicular to those in the cone with volume V_2.

Figure 6-6 The cone with the volume V_2. All vectors being perpendicular to those in the cone will fall into volume V_3, i.e., in this figure along the equatorial plane.

Volume V3 can be calculated by

$$V_3 = 4\,\pi\ /\ 3\,(\cos\,(\pi/2 - \varphi)\,) \qquad \textit{(Eq. 6-10)}$$

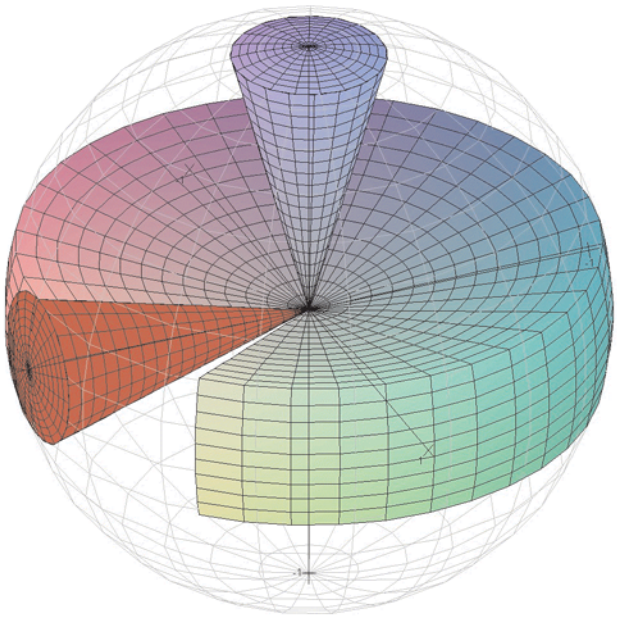

These vectors within a deviation of φ from the ideal orientation of the second reference axis will fall in a cone with the opening angle φ and the ideal orientation of the second reference axis as a cone axis. This cone, having the volume V_2 , is displayed in Fig. 6-7 in red. A part of the volume V_3 has been cut away for better clarity of the presentation.

Figure 6-7 All possible vectors within an angle φ from the ideal orientations of the first and the second reference axes fall within the blue and the red cone, respectively.

The probability p_2 for a vector lying within the volume V_3 and the volume V_2 is

$$p_2 = V_2 / V_3 = (\,-\cos\varphi + 1)\ /\ (2\,(\cos\,(\pi/2 - \varphi)) \qquad \textit{(Eq. 6-11)}$$

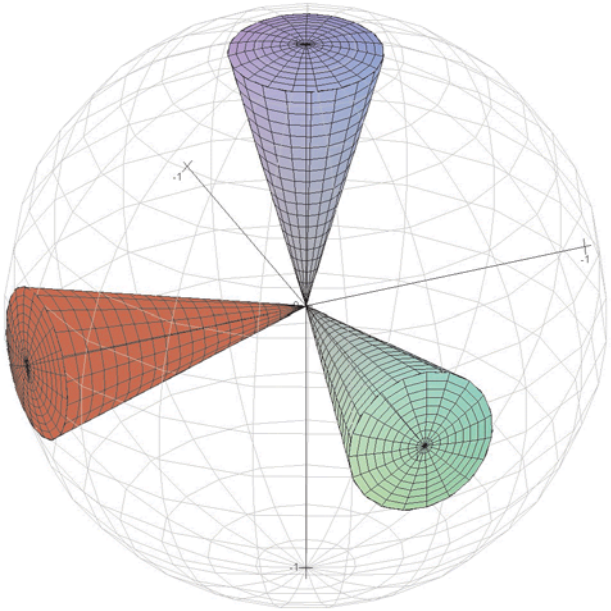

If two of the reference axes are defined, the third one will be perpendicular to both of them. The corresponding vector will again situate within a cone with an opening angle φ and the ideal orientation, the third axis, as the cone axis, displayed in green in Fig. 6-8. The probability for it to be there is $p_3 = 1$.

Figure 6-8 The three cones corresponding to the three reference axes are shown.

The probability that all three axes are within a deviation of φ from their ideal orientation is p_4:

$$p_4 = p_1\, p_2\, p_3 = (-\cos\varphi + 1)^2 \,/\, (4\cos(\pi/2 - \varphi)) \qquad \textit{(Eq. 6-12)}$$

This probability p_4 is multiplied by the factor 24, because 24 different symmetrically equivalent ways are possible to describe the reference axes with respect to the crystal axes.
Yuki offers also a possibility to calculate the texture strength of a texture type, having more than one texture components. For example, the copper texture {112}<111> has two different components, *i.e.*, (112)[111] and (112)[$\bar{1}$11].
In this case, the probability p_4 is multiplied by 24 and the number of components to obtain the random reference for this sheet texture.

6.5 Euler Angles and Rodrigues Vectors

Euler angles and Rodrigues vectors can be calculated for orientation and misorientation matrices.
The three Euler angles describe three sequential rotations, which can be mathematically described by three rotation matrices, according to Eq. 6-4, 6-5 and 6-6 for the crystal [100], [010] and [001] axis, respectively. The rotation matrix M, describing all three sequential rotations, can be obtained by the matrix multiplication of the three matrices:

$$M = M_3\, M_2\, M_1 \qquad \textit{(Eq. 6-13)}$$

where M_1, M_2 and M_3 are the rotation matrices for the first, second and third of the sequential rotations, respectively.
The elements of the orientation or disorientation matrix, a_{11} to a_{33}, can be obtained from the three Euler angles φ_1, Φ and φ_2 (Bunge specification) and from Ψ, Θ and Φ (Roe specification) according to Table 6-2. Also the relation between the two specifications is described there.
If the second Euler angle is equal to zero, the orientation is not defined unambiguously, but every combination of the first and third rotation angles giving the same sum can be used to describe the orientation. In the present work, the entire rotation is defined by the first rotation angle, the third one is set to zero.
Rodrigues vectors are calculated from the angle/axis pairs within the fundamental zone in the Rodrigues-Frank space, for disorientation matrices additionally within 1/48 of the fundamental zone as described in section 4.9.
Both, Euler angles and Rodrigues vectors can be used to display the grain orientations or the grain boundary geometry in the Euler space or in the Rodrigues-Frank space, respectively.

Table 6-2 The relation between the orientation and misorientation matrices and the Euler angles after Bunge and Roe, and the relationship between the two Euler angle specifications, as well as, the angle ranges.

Bunge specification	Roe specification
$a_{11} = \cos\varphi_2 \cos\varphi_1 - \sin\varphi_2 \cos\Phi \sin\varphi_1$	$a_{11} = \cos\Psi \cos\Phi \cos\Theta - \sin\Psi \sin\Phi$
$a_{12} = \cos\varphi_2 \sin\varphi_1 + \sin\varphi_2 \cos\Phi \cos\varphi_1$	$a_{12} = \cos\Phi \cos\Theta \sin\Psi + \sin\Phi \cos\Psi$
$a_{13} = \sin\varphi_2 \sin\Phi$	$a_{13} = -\cos\Phi \sin\Theta$
$a_{21} = -\sin\varphi_2 \cos\varphi_1 - \sin\varphi_1 \cos\varphi_2 \cos\Phi$	$a_{21} = -\sin\Phi \cos\Theta \cos\Psi - \sin\Psi \cos\Phi$
$a_{22} = -\sin\varphi_2 \sin\varphi_1 + \cos\varphi_2 \cos\Phi \cos\varphi_1$	$a_{22} = -\sin\Phi \cos\Theta \sin\Psi + \cos\Phi \cos\Psi$
$a_{23} = \cos\varphi_2 \sin\Phi$	$a_{23} = \sin\Phi \sin\Theta$
$a_{31} = \sin\Phi \sin\varphi_1$	$a_{31} = \sin\Theta \cos\Psi$
$a_{32} = -\sin\Phi \cos\varphi_1$	$a_{32} = \sin\Theta \sin\Psi$
$a_{33} = \cos\Phi$	$a_{33} = \cos\Theta$
$0 < \varphi_1 < 2\pi$	$\varphi_1 = \Psi - \pi/2$	$0 < \Psi < 2\pi$
$0 < \Phi < \pi$	$\Phi = \Theta$	$0 < \Theta < \pi$
$0 < \varphi_2 < 2\pi$	$\varphi_2 = \Phi - \pi/2$	$0 < \Phi < 2\pi$

6.6 Grain Boundary Analysis

The grain numbers of the neighboring grains have to be saved in an Excel file. This file and the data file are used to calculate the angle/axis pairs and the GBCD. All calculated results are stored again into an Excel file to allow further analysis, for example to plot a grain boundary map.

6.6.1 Angle/Axis Pairs

The disorientation matrices are calculated according to Eq. 4-2 and Eq. 4-3. They describe the rotation with respect to the sample reference axes and with respect to the crystal axes of one grain.
These matrices are used to calculate the angle/axis pairs according to Eq. 4-5, 4-6 and 4-7.
The disorientation angle distribution is displayed as a chart. The disorientation axes are plotted relative to the crystal axes as well as to the specimen axes in a stereographic projection. Also sections through a three dimensional angle/axis space are used utilizing a stereogram in the x-y plane and taking the disorientation angle as the z-axis. An example for the presentation possibilities of the angle/axis pair distribution is shown in Fig. 6-9. 258 grain boundaries of a copper sample were analyzed, showing a [001] as well as ND disorientation axis texture. This sample showed a ND <100> fiber texture. The random reference which was used in the representation of the disorientation distribution relative to the crystal axes was taken from *Mackenzie (1964)*. The so-called 'Mackenzie triangle' is divided into 8 areas, 5 of them are defined by a deviation of 5, 10, 15, 30 and 45 degrees from the [001] crystal direction, 2 by a deviation of 5

and 9.7 degrees from the [$\bar{1}11$] direction, and the last one contains all the other disorientation axes.

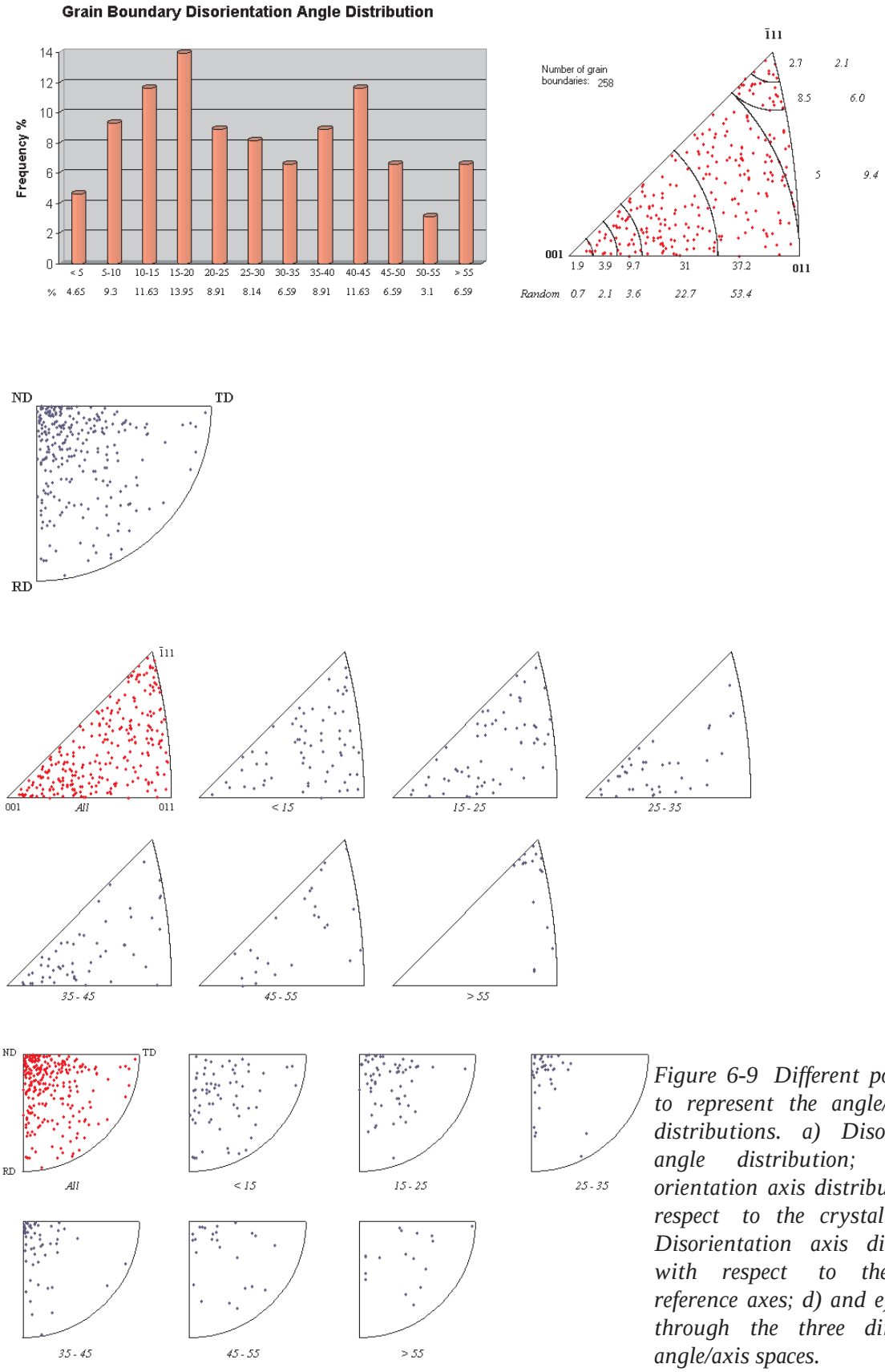

Figure 6-9 Different possibilities to represent the angle/axis pair distributions. a) Disorientation angle distribution; b) Disorientation axis distribution with respect to the crystal axes; c) Disorientation axis distribution with respect to the sample reference axes; d) and e) Sections through the three dimensional angle/axis spaces.

6.6.2 Coincident Site Lattice

The user can define the maximum Σ-value, which is used to categorize a grain boundary as a CSL, up to 49. In the literature the most frequently used values are 25, 29 and 49. The Brandon criterion is used to define the maximum deviation from the ideal CSL boundary. If necessary, it is possible to redefine the deviation criterion by a multiplication factor.
The deviation of the ideal CSL disorientation is determined by comparing the disorientation matrices for the experimental and CSL case, M_{exp} and M_{CSL}, respectively. The difference matrix M_D is calculated by

$$M_D = M_{exp}\, M_{CSL}^{-1} \qquad \textit{(Eq. 6-14)}$$

The angular deviation can be determined from the difference matrix M_D by Eq. 4-5.
Both disorientation matrices have to be related to the same symmetry related solution. Therefore the disorientation matrices are recalculated from the angle / axis pairs, with the axis [uvw] defined by $u \geq v \geq w \geq 0$ and $u^2+v^2+w^2=1$. The following relationships are used

$$\begin{aligned}
a_{11} &= u^2 (1- \cos\theta) + \cos\theta \\
a_{12} &= u\, v (1- \cos\theta) - w \sin\theta \\
a_{13} &= u\, w (1- \cos\theta) + v \sin\theta \\
a_{21} &= v\, u (1- \cos\theta) + w \sin\theta \\
a_{22} &= v^2 (1- \cos\theta) + \cos\theta \\
a_{23} &= v\, w (1- \cos\theta) - u \sin\theta \\
a_{31} &= w\, u (1- \cos\theta) - v \sin\theta \\
a_{32} &= w\, v (1- \cos\theta) + u \sin\theta \\
a_{33} &= w^2 (1- \cos\theta) + \cos\theta
\end{aligned} \qquad \textit{(Eq. 6-15)}$$

where a_{11} to a_{33} are the elements of the disorientation matrix, [uvw] is the disorientation axis and θ is the disorientation angle.
The angle / axis pairs for the coincident boundaries have been extracted from a look-up table (Table 6-3).
A measured grain boundary may be within the maximum deviation of several coincident boundaries. This is taken into account in the GBCD (Fig. 6-10), the percentage values for the low angle (LA), coincident and random boundaries are given correctly. The sum of them, however, is generally larger than 100 % due to the overlapping of regions of existence of special boundaries.

Table 6-3 The angle/axis pairs for each cubic CSL up to Σ 49 (Grain Boundary Structure and Kinetics, 1980).

Σ	θ	[uvw]	Σ	θ	[uvw]
1 (LA)	< 15°	any	33a	20.05°	<110>
3	60°	<111>	33b	33.55°	<311>
5	36.87°	<100>	33c	58.98°	<110>
7	38.21°	<111>	35a	34.04°	<211>
9	38.94°	<110>	35b	43.23°	<331>
11	50.48°	<110>	37a	18.92°	<100>
13a	22.62°	<100>	37b	43.13°	<310>
13b	27.80°	<111>	37c	50.57°	<111>
15	48.19°	<210>	39a	32.21°	<111>
17a	28.07°	<100>	39b	50.13°	<321>
17b	61.93°	<221>	41a	12.68°	<100>
19a	26.53°	<110>	41b	40.88°	<210>
19b	46.83°	<111>	41c	55.88°	<110>
21a	21.79°	<111>	43a	15.18°	<111>
21b	44.40°	<211>	43b	27.91°	<210>
23	40.45°	<311>	43c	60.77°	<332>
25a	16.25°	<100>	45a	28.62°	<311>
25b	51.68°	<331>	45b	36.87°	<221>
27a	31.58°	<110>	45c	53.13°	<221>
27b	35.42°	<210>	47a	37.07°	<331>
29a	43.61°	<100>	47b	43.66°	<320>
29b	46.39°	<221>	49a	43.58°	<111>
31a	17.90°	<111>	49b	43.58°	<511>
31b	52.19°	<211>	49c	49.22°	<322>

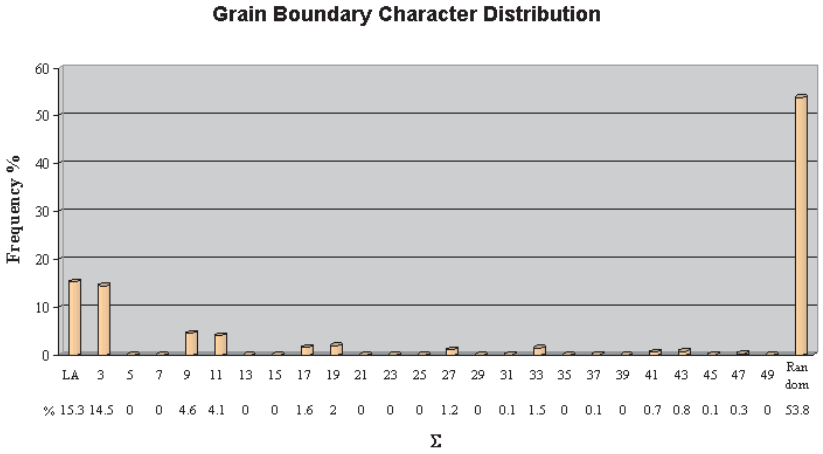

Figure 6-10 A GBCD of simulated grain boundaries from data having a strong <110> fiber texture. The sum of the frequencies is 100.76 % due to the overlapping of regions of existence of CSL boundaries.

6.6.3 Triple Grain Junctions

When two grains meet at a grain boundary, they are separated by a grain boundary surface. Three or more grains meet only by a line. Generally, the number of grains meeting on a line is three due to energetic considerations. Such a line is called as a triple line or a triple grain junction. Grain boundaries with a low energy, *e.g.*, low Σ value boundaries, can cause favorable conditions for more than three grain boundaries to meet at a grain junction. These are called multiple grain junctions.
Triple lines play an important role in processes like intergranular corrosion and intergranular fracture. In case of intergranular fracture for example, the crack will often stop on a triple line if it meets two grain boundaries which are resistant to intergranular fracture. In order to be able to propagate it should change its mode of fracture from intergranular to transgranular. More energy is needed for this and therefore it happens rather seldom.
An algorithm was developed to identify the triple lines from the list of neighboring grains. The triple lines are categorized, according to the CSL model, into triple lines where no, one, two or three special boundaries meet (Fig. 6-11).
The algorithm does not work when more than three grains meet at a line. For example, when four grains meet, this multiple grain junction is counted as two separate triple lines.

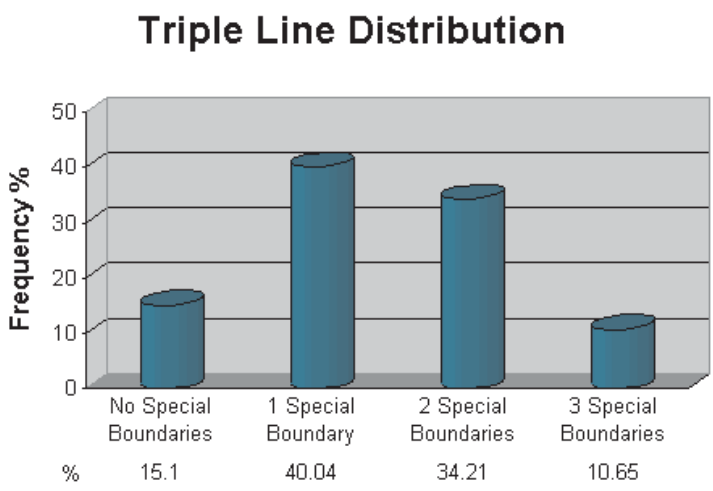

Figure 6-11 An example of a triple line distribution. The special boundaries are low angle and all Σ boundaries, i.e., those selected as special ones in the GBCD.

6.7 Simulations

Texture and grain boundary simulations can also be performed by Yuki. The simulations can be used either to assist the identification of texture components in the pole figures, or to illustrate the relationship between texture and grain boundary geometry.

6.7.1 Texture Simulations

It is possible to generate simulated orientation matrices with a random, fiber or sheet texture by using a random number generator.
The simulation of the random textured data is outlined in this paragraph in more detail, paying a special attention to the question how a mathematical operation can transform random numbers in such a way that they cease to be random.
A random orientation matrix is simulated in the current version of the software with three random numbers, *i.e.*, a, b, c, between -1 and 1.
Two pseudo random numbers are generated, a and b, respectively. They are used to create a unit vector consisting of 3 numbers, when $a^2 + b^2$ is smaller than 1, otherwise they are rejected. This vector corresponds to the first column of the orientation matrix. Then a third pseudo random number (c) is generated, corresponding to the first element of the second column in the orientation matrix. The other two elements of the second column are calculated, so that the resulting vector is perpendicular to this in the first column and has a unit length. The vector in the third column is perpendicular to those two in the first and in the second column.
This method has been chosen because other attempts to simulate random texture resulted in a clearly non-random texture.

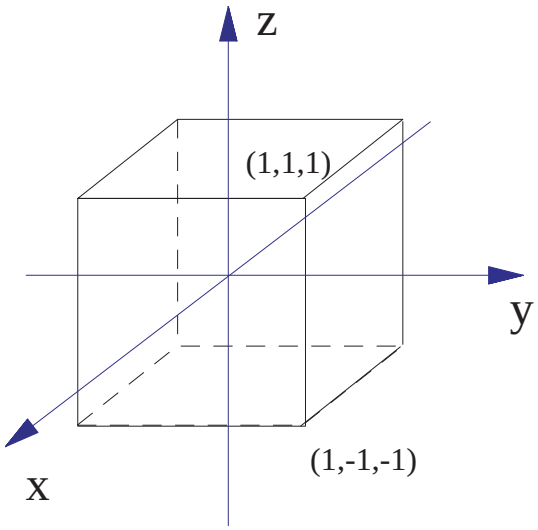

When a vector is generated from three random numbers, the three random numbers describe a vector within a cube with an edge length of 2 (Fig. 6-12). When these vectors are normalized, they describe a unit sphere. However, they are not evenly distributed on this unit sphere, since more initial vectors existed in the directions of the cube edges and corners. The cube edges and corners can be clearly seen in the pole figures representing simulated data by this method (Fig. 6-13).

Figure 6-12 Three independent random numbers between -1 and 1 describe a vector within the shown cube.

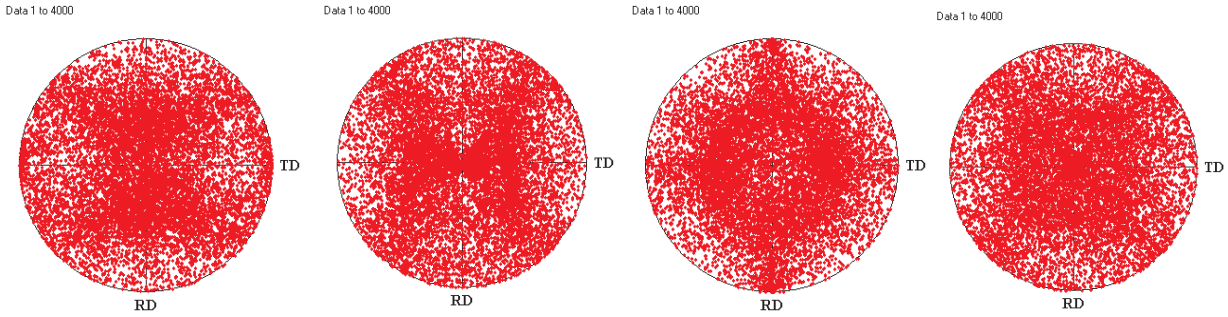

Figure 6-13 The effect of the normalization of a vector can be seen. The first (RD), second (TD) and third column (ND) as well as the first row ([100]) of the orientation matrix were normalized to generate the data displayed as {100} pole figures in a), b), c) and d), respectively. The edges and corners of the random number cube can be seen clearly in the projections.

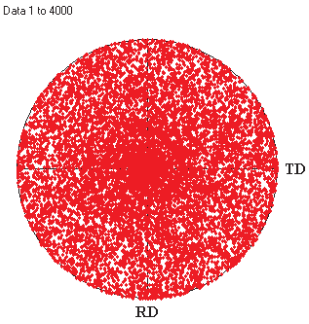

Another reason for non-random texture is the calculation of the cosines of an angle when three randomly generated Euler angles are used to generate the orientation matrix (Fig. 6-14).

Figure 6-14 The ND shows a <100> texture due to the use of the cosines function for calculating the orientation matrices from three randomly generated Euler angles

All orientation matrices within a selected maximum deviation from the ideal orientation are used to simulate fiber and sheet textures.

6.7.2 Grain Boundary Simulations

Texture influences the grain boundary structure. This can be easily understood when considering a material having a strong fiber texture. It can be shown that grain boundaries with the fiber axis as a misorientation axis are frequently found in these materials.

To provide a possibility to understand this texture influence better, the simulation of grain boundary geometry is included in the software. It is assumed that the grains having different orientations are distributed randomly in the polycrystalline material. No orientation correlation between neighboring grains is taken into account. This assumption is not true for many practical materials, *e.g.*, because of processing induced deformation and recrystallization twinning.

In principle use of a three dimensional arrangement of grains would be the correct way to do the simulation. *Garbacz & Grabski (1993)* showed that the results of simulations of grain boundary geometry do not differ much for different arrangements of the orientation data. They used small grain clusters of two and three grains as well as three dimensional arrangements of cubic and Kelvin polyhedra (tetrakaidekahedra)-shaped grains for their simulations.

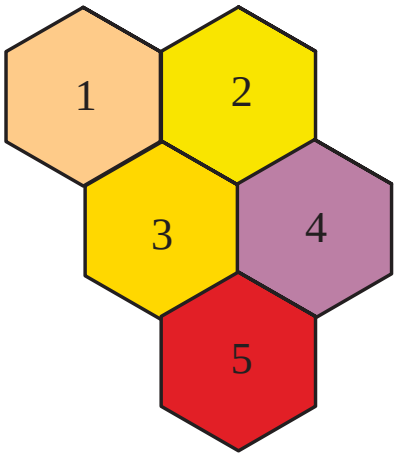

In the present work small grain clusters of five grains are used to calculate the geometry of seven grain boundaries and three triple junctions (Fig. 6-15). The algorithm to simulate these grain clusters is easier to develop than the one where all orientation data are arranged into a three dimensional grain aggregate.

Figure 6-15 A schematic representation of the grain cluster used for the simulations in the present work.

Two different kinds of simulations can be done. One possibility is to use simulated orientation data to study the influence of texture on GBCD. In this case, the simulated orientation matrices are used only once for the simulation, and grain clusters are built until no simulated data are left.
The other possibility is to use measured data for the simulation. This is to provide a reference for the textural influence on GBCD. This reference can be compared with the measured grain boundary geometry. This comparison makes it possible to study how strongly the texture influences the GBCD and to what extent other factors like twinning or kinetic factors during the processing and heat treatment of the material will influence the GBCD. However, this simulation should not be used to predict GBCD based on the measured texture as in the most cases it will not give a correct result.
The number of grain clusters can be selected when measured data are used for the simulation. A high number is recommended to give statistically meaningful information, even if the measured grain number is low. All orientation data are used several times during a simulation, but they are never used twice for one grain cluster.

7 Computer Simulations of the Texture Influence on the Grain Boundary Geometry

Several grain boundary simulations from textured data sets have been carried out to illustrate the effect of texture on the GBCD.
Moreover, orientation matrices with random texture have been used to simulate random grain boundary geometry providing a random reference for the analysis of measured data.

7.1 Random Texture

Three grain boundary simulations, each of them from 8,000 random textured data, were done. The results of the 33,600 grain boundaries and the 14,400 triple lines are presented in this section.
The differences between the disorientation angle distribution, disorientation axis distribution and GBCD of the three individual simulations were small. The texture strength calculations of the generated random data, however, varied remarkably (Table 7-1), especially for the different sheet textures. These variations can be explained by the fairly low number of orientation data and the way of random number generation by a computer. All random numbers result from a specific mathematical operation with a seed value. The value returned by the system timer is generally used as the first seed value, thereafter the last generated number is used as the following seed value. Therefore, the random data result will depend on the time of day when the simulation was started.
The results of the disorientation angle distribution are given in Table 7-2, those of the disorientation axis distribution in the Mackenzie triangle in Table 7-3. The GBCD using the Brandon criterion is listed in Table 7-4, giving the percentages of random boundaries for a maximum Σ of 25, 29 and 49. These three maximum Σ values were chosen, because all three are frequently used in the literature. Finally, the triple line distributions corresponding to a maximum Σ value of 25, 29 and 49 are given in Table 7-5.
These results comprise a random reference for studies on the grain boundary geometry of real specimens.

Table 7-1 The texture strength results for the three random simulated data sets, calculated for several different texture types, fiber as well as sheet textures. The random reference used is presented in section 6.4.

	1. Simulation of 8000 random textured data					
Texture type	% within a deviation of 5 degrees	× random	% within a deviation of 10 degrees	× random	% within a deviation of 15 degrees	× random
<111> ND	1.35	0.89	6.79	1.12	15.1	1.11
<112> TD	4.89	1.07	18.89	1.04	42.7	1.04
<123> RD	9.23	1.01	37.5	1.03	69.83	0.85
(001)[100]	0.01	0.13	0.45	0.56	1.71	0.64
{112}<111>	0.19	0.94	1.76	1.11	5.15	0.96
{123}<412>	0.28	0.69	2.78	0.87	9.66	0.90
	2. Simulation of 8000 random textured data					
Texture type	% within a deviation of 5 degrees	× random	% within a deviation of 10 degrees	× random	% within a deviation of 15 degrees	× random
<111> ND	1.75	1.15	6.76	1.11	14.91	1.09
<112> TD	4.61	1.01	19	1.04	42.49	1.03
<123> RD	9.61	1.05	37.79	1.04	70.22	0.86
(001)[100]	0.1	1.00	0.63	0.78	2.03	0.75
{112}<111>	0.28	1.38	1.69	1.06	5	0.93
{123}<412>	0.35	0.88	2.8	0.88	9.76	0.91
	3. Simulation of 8000 random textured data					
Texture type	% within a deviation of 5 degrees	× random	% within a deviation of 10 degrees	× random	% within a deviation of 15 degrees	× random
<111> ND	1.44	0.94	6.61	1.09	14.59	1.07
<112> TD	4.81	1.05	19.2	1.05	42.79	1.05
<123> RD	9.09	1.00	38.05	1.04	70.33	0.86
(001)[100]	0.05	0.50	0.43	0.53	1.5	0.56
{112}<111>	0.25	1.25	1.7	1.07	5.41	1.01
{123}<412>	0.5	1.25	3.03	0.95	9.66	0.90

Table 7-2 The disorientation angle distribution for the three simulations. The result for all simulated grain boundaries comprises a random reference for the analysis of the measured data.

Disorientation Angle Distribution (%)				
Angle range	*1. Simulation*	*2. Simulation*	*3. Simulation*	*All simulated grain boundaries*
< 5°	0.05	0.12	0.05	0.07
5 °- 10°	0.65	0.59	0.62	0.62
10° - 15°	1.58	1.53	1.65	1.59
15° - 20°	3.21	3.23	3.09	3.18
20° - 25°	4.77	5.14	5.44	5.12
25° - 30°	7.77	7.53	7.25	7.51
30° - 35°	10.21	10.39	10.28	10.29
35° - 40°	13.96	14.11	14.03	14.03
40° - 45°	17.24	17.70	17.41	17.45
45° - 50°	17.90	17.60	17.63	17.71
50° - 55°	13.92	13.45	13.91	13.76
> 55°	8.74	8.63	8.65	8.67

Table 7-3 The random disorientation axis distribution obtained by the simulations for the 'Mackenzie triangle' (Fig. 7-1). Compared to the analytical result of Mackenzie (1964), it shows a good coincidence.

Disorientation Axes Distribution (%)					
Zone in the 'Mackenzie triangle'	*1. Simulation*	*2. Simulation*	*3. Simulation*	*All grain boundaries*	*Analytical solution*
I	0.67	0.78	0.65	0.70	0.7
II	1.96	2.09	2.18	2.08	2.1
III	3.74	3.83	3.13	3.57	3.6
IV	22.23	22.52	22.75	22.50	22.7
V	53.63	53.29	53.71	53.54	53.4
VI	2.19	1.94	2.29	2.14	2.1
VII	6.10	5.96	6.08	6.05	6
VIII	9.47	9.59	9.21	9.43	9.4

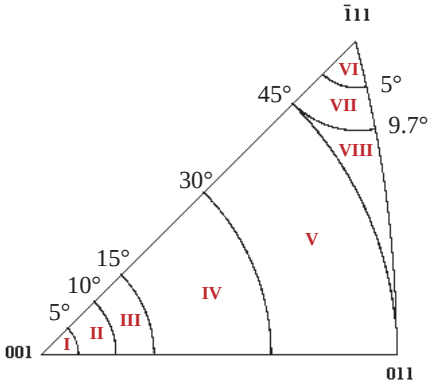

Figure 7-1 The different zones in the 'Mackenzie triangle'.

Table 7-4 The GBCD, the percentages of the random boundaries are given for a maximum Σ value of 25, 29 and 49.

GBCD (%)				
Σ	*1. Simulation*	*2. Simulation*	*3. Simulation*	*All Boundaries*
LA	2.29	2.23	2.32	2.28
3	1.75	1.64	1.86	1.75
5	1.12	1.23	1.29	1.21
7	1.01	0.98	1.13	1.04
9	1.11	0.90	1.08	1.03
11	0.71	0.88	0.77	0.78
13a	0.27	0.27	0.31	0.28
13b	0.39	0.43	0.40	0.41
15	0.69	0.77	0.50	0.65
17a	0.16	0.16	0.19	0.17
17b	0.30	0.34	0.30	0.32
19a	0.29	0.36	0.29	0.32
19b	0.19	0.19	0.22	0.20
21a	0.19	0.22	0.20	0.20
21b	0.66	0.55	0.51	0.57
23	0.51	0.44	0.45	0.46
25a	0.11	0.16	0.08	0.12
25b	0.53	0.36	0.48	0.46
27a	0.21	0.14	0.16	0.17
27b	0.45	0.34	0.27	0.35
29a	0.11	0.13	0.13	0.12
29b	0.34	0.41	0.33	0.36
31a	0.16	0.06	0.12	0.11
31b	0.32	0.24	0.25	0.27
33a	0.15	0.19	0.15	0.16
33b	0.37	0.23	0.22	0.27
33c	0.10	0.05	0.07	0.07
35a	0.26	0.32	0.23	0.27
35b	0.32	0.36	0.21	0.30
37a	0.06	0.07	0.06	0.07
37b	0.18	0.13	0.26	0.19
37c	0.05	0.06	0.06	0.06
39a	0.04	0.04	0.10	0.06
39b	0.38	0.42	0.43	0.41
41a	0.04	0.06	0.04	0.04
41b	0.17	0.26	0.24	0.22
41c	0.12	0.03	0.13	0.09
43a	0.09	0.07	0.04	0.07
43b	0.16	0.21	0.22	0.20
43c	0.09	0.12	0.13	0.11
45a	0.12	0.22	0.16	0.17
45b	0.18	0.24	0.15	0.19
45c	0.17	0.17	0.21	0.18
47a	0.17	0.24	0.17	0.19
47b	0.15	0.14	0.22	0.17
49a	0.08	0.11	0.04	0.07
49b	0.13	0.15	0.12	0.13
49c	0.21	0.22	0.14	0.19
Random (Σ_{max}=25)	87.83	87.97	87.70	87.83
Random (Σ_{max}=29)	86.77	87.01	86.91	86.90
Random (Σ_{max}=49)	82.88	82.95	83.03	82.95

Table 7-5 The triple line distributions. Grain Boundaries are categorized as special by the CSL model. Σ 25, Σ 29 and Σ 49 were used in turn as the upper Σ limit, to specify a grain boundary as special.

Triple Line Distribution (%)				
Σ_{max} = 25				
Number of special boundaries	*1. Simulation*	*2. Simulation*	*3. Simulation*	*All Boundaries*
0	68.60	68.13	67.90	68.21
1	27.50	28.17	27.81	27.83
2	3.71	3.56	4.15	3.81
3	0.19	0.15	0.15	0.16
Σ_{max} = 29				
Number of special boundaries	*1. Simulation*	*2. Simulation*	*3. Simulation*	*All Boundaries*
0	65.10	65.52	66.40	65.67
1	29.88	30.23	28.94	29.68
2	4.77	4.06	4.52	4.45
3	0.25	0.19	0.15	0.19
Σ_{max} = 49				
Number of special boundaries	*1. Simulation*	*2. Simulation*	*3. Simulation*	*All Boundaries*
0	56.44	56.71	56.58	56.58
1	36.33	35.67	34.83	35.61
2	6.79	7.25	8.10	7.38
3	0.44	0.38	0.48	0.43

7.2 Dependency of the GBCD and the Disorientation Angle and Axis Distribution on the Spread of a <100> Fiber Texture

The GBCD depends strongly on the sharpness of the texture. The simulations done provide a good example for this.
Four different data sets of 8000 data were simulated, having a ND <100> fiber texture. The maximum deviation was chosen to be 2, 5, 10 and 15 degrees for each simulation, respectively (Fig. 7-2). The results show clearly the strong dependence of the grain boundary geometry distribution on the sharpness of the texture.

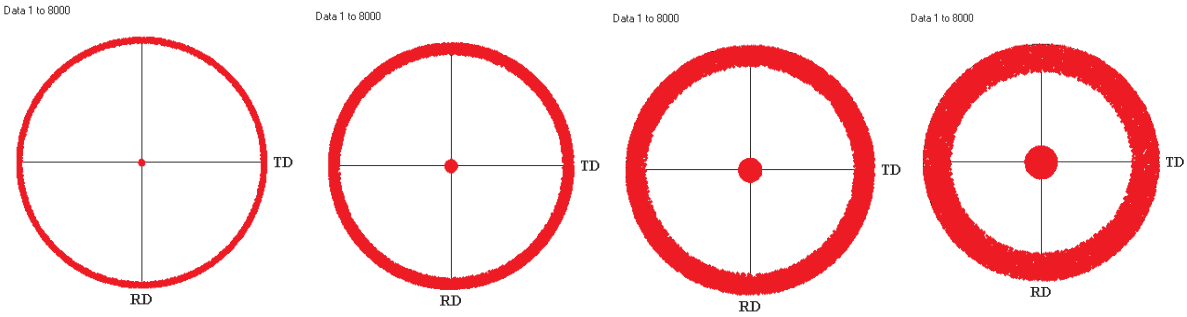

Figure 7-2 {100} pole figures of the four different simulated data sets. The maximum deviation from the ideal ND <100> fiber texture is 2, 5, 10 and 15 degrees, respectively.

Fig. 7-3 presents the results of the disorientation angle distribution. It can be seen that the amount of low angle boundaries decreases with decreasing sharpness of the texture, whereas the frequency of high angle boundaries increases.

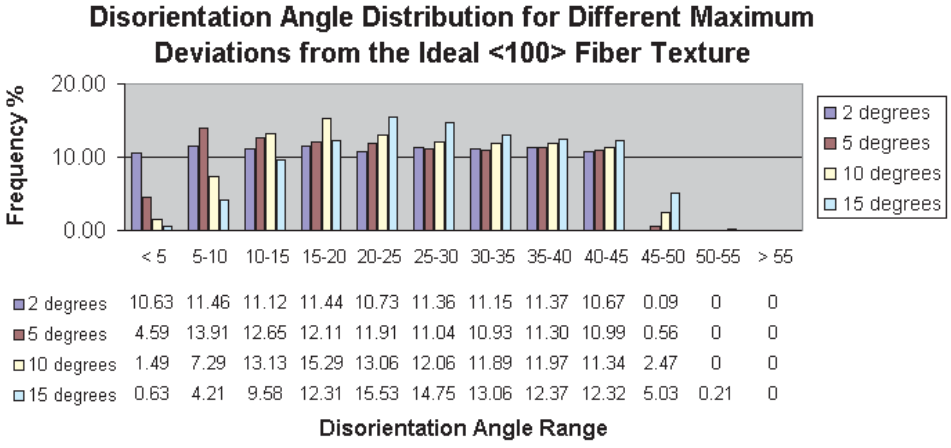

Figure 7-3 The disorientation angle distribution of the 11,200 simulated grain boundaries for different sharpness of the <100> texture.

The eight zones of the Mackenzie triangle are used to present the disorientation axis distribution dependency on the sharpness of the texture in Fig. 7-4. It is obvious that most of the disorientation axes are near the <100> direction for a sharp texture, however, when the texture becomes less sharp, disorientation axes deviate more strongly from the fiber axis.

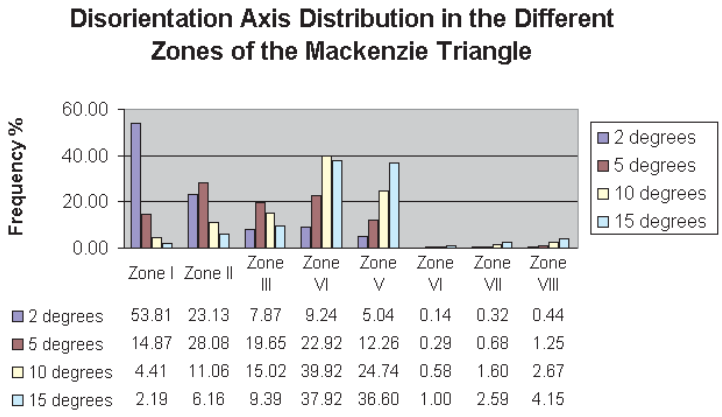

Fig. 7-4 The disorientation axis distribution for the simulations from the differently sharp <100> textured data sets.

To present the influence of the sharpness of the texture on the GBCD only those coincident boundaries up to Σ 49 having an <100> misorientation axis are selected. The GBCD shows a strong dependency on the sharpness of the fiber texture. While the frequency of random boundaries is 3.5 % for the simulation with the sharpest texture (2 degrees maximum deviation), it increases to 73 % for this simulation using a fiber texture having a maximum deviation of 15 degrees (Fig. 7-5).

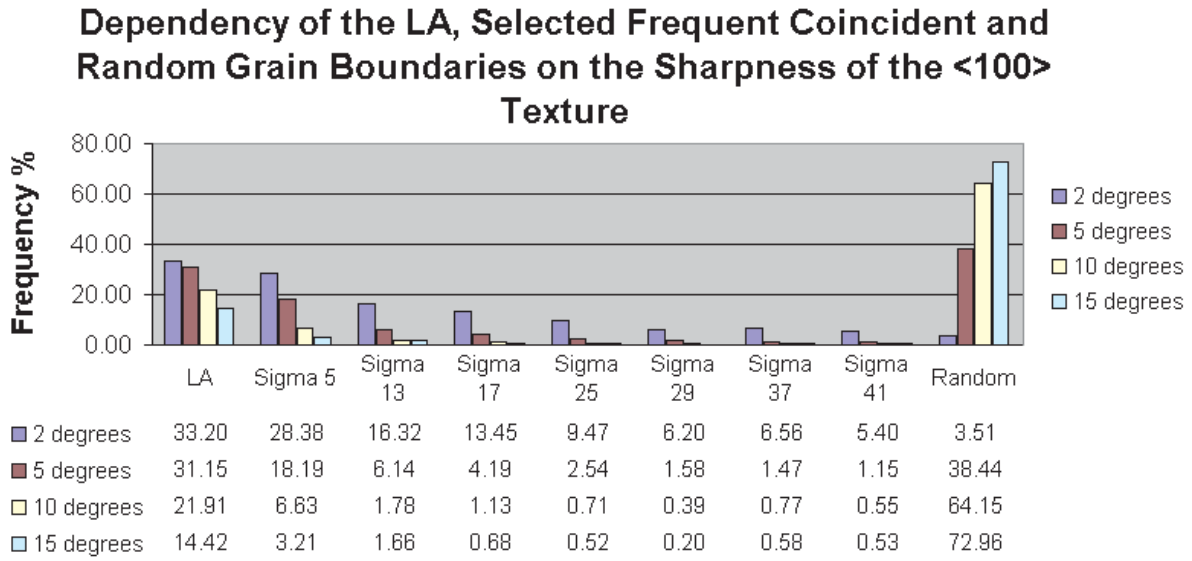

	LA	Sigma 5	Sigma 13	Sigma 17	Sigma 25	Sigma 29	Sigma 37	Sigma 41	Random
2 degrees	33.20	28.38	16.32	13.45	9.47	6.20	6.56	5.40	3.51
5 degrees	31.15	18.19	6.14	4.19	2.54	1.58	1.47	1.15	38.44
10 degrees	21.91	6.63	1.78	1.13	0.71	0.39	0.77	0.55	64.15
15 degrees	14.42	3.21	1.66	0.68	0.52	0.20	0.58	0.53	72.96

Figure 7-5 The GBCD shows a strong increase of random boundaries with decreasing sharpness of the <100> fiber texture. Σ 49 was chosen as the upper limit to define a grain boundary as special.

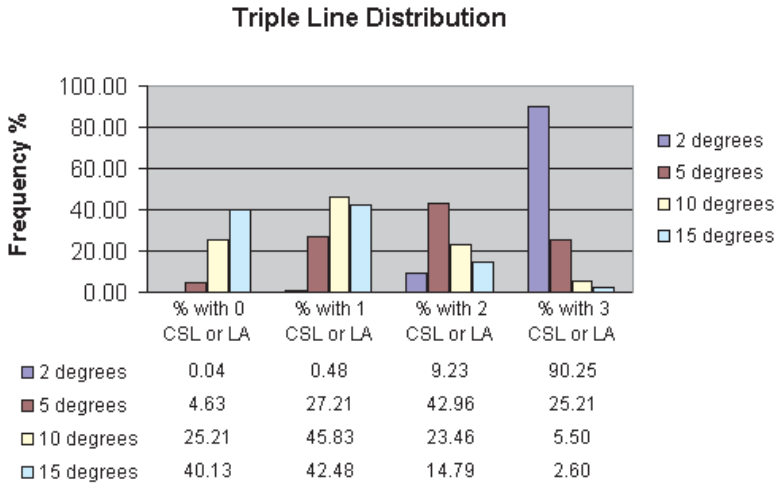

	% with 0 CSL or LA	% with 1 CSL or LA	% with 2 CSL or LA	% with 3 CSL or LA
2 degrees	0.04	0.48	9.23	90.25
5 degrees	4.63	27.21	42.96	25.21
10 degrees	25.21	45.83	23.46	5.50
15 degrees	40.13	42.48	14.79	2.60

The strong influence of the sharpness of texture can be also seen in the triple line distribution (Fig. 7-6).

Figure 7-6 The triple lines are categorized according to the CSL model, using a upper Σ limit of 49. Unambiguously, the sharpness of the texture has a strong influence on the triple line distribution.

7.3 Different Fiber Textures

Different ND fiber textures, *i.e.*, <100>, <110>, <111>, <112> and <113>, are used to illustrate their effect on the grain boundary geometry distribution. The maximum deviation from the ideal orientation is 5 degrees in each case. The disorientation angle and axis distribution as well as the GBCD differ strongly for the different textures. Fig. 7-7 and Fig. 7-8 show the disorientation angle and axis distribution, respectively.

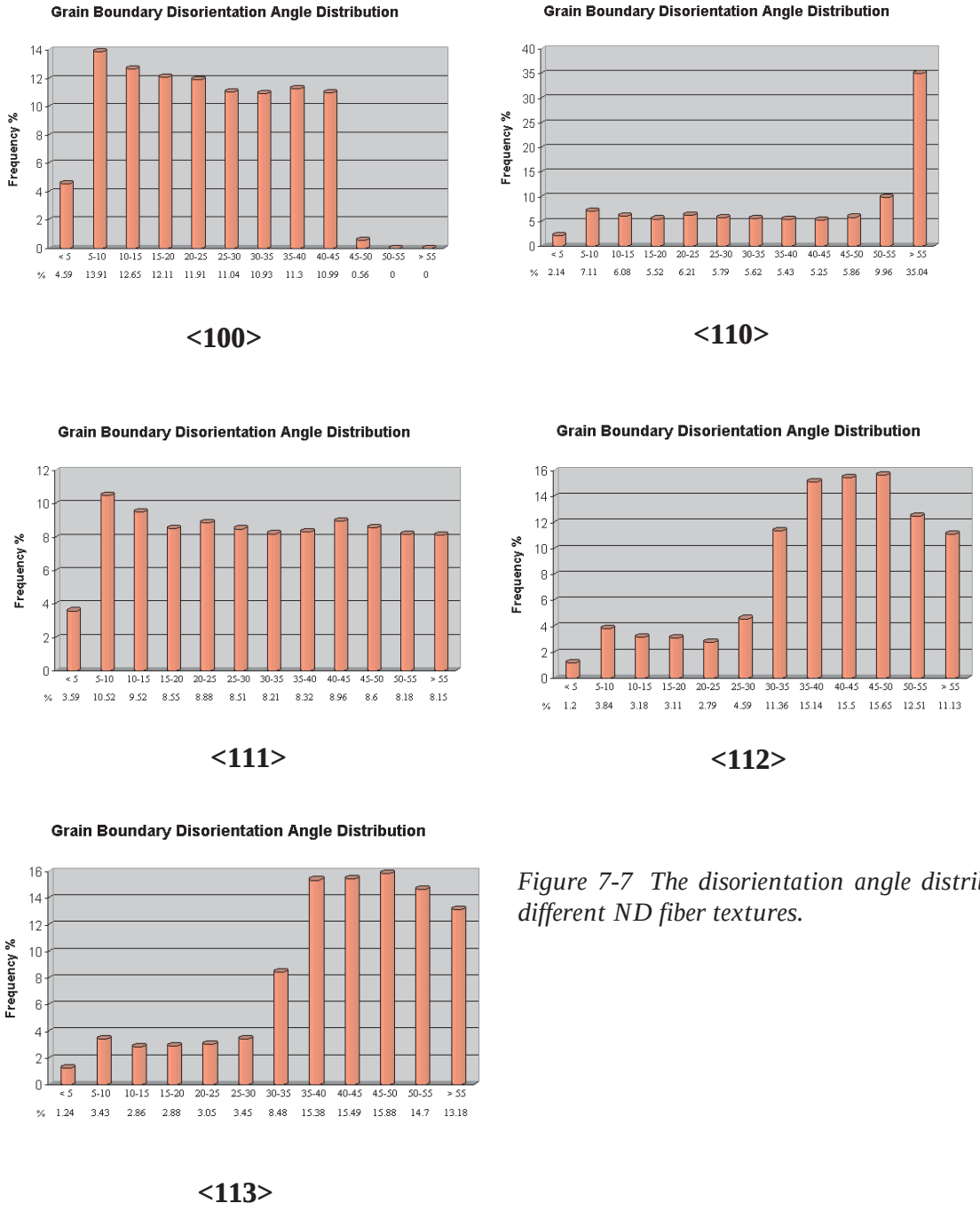

Figure 7-7 The disorientation angle distribution for different ND fiber textures.

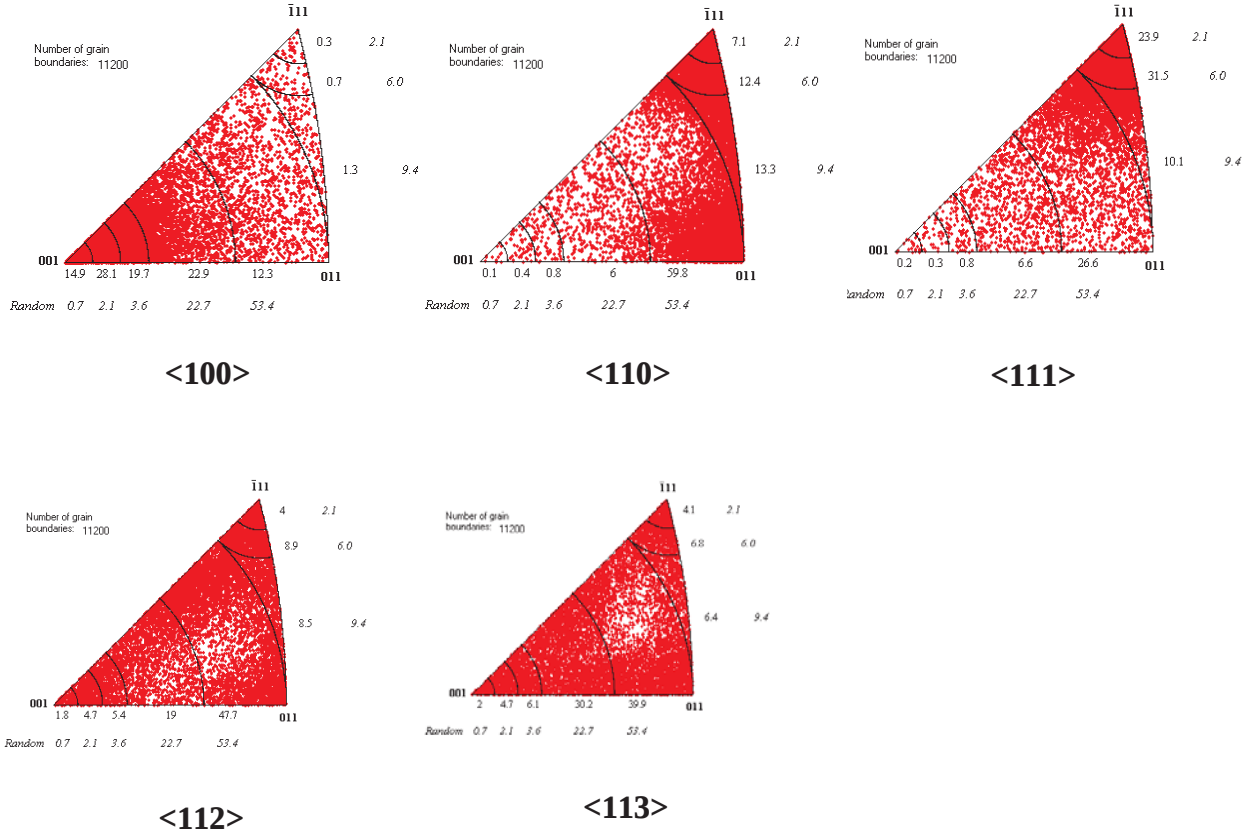

Figure 7-8 The disorientation axis distributions for the five different fiber textures.

Especially of interest are the GBCDs. Obviously, those coincident boundaries having the fiber axis as misorientation axes have a high frequency. The simulation results for the GBCDs are presented in Fig. 7-9, additionally all coincident boundaries having the fiber axis as a misorientation axis are listed next to the GBCD chart with their misorientation angle. When those misorientations are not disorientations, the disorientation axis and angle is given additionally in brackets.

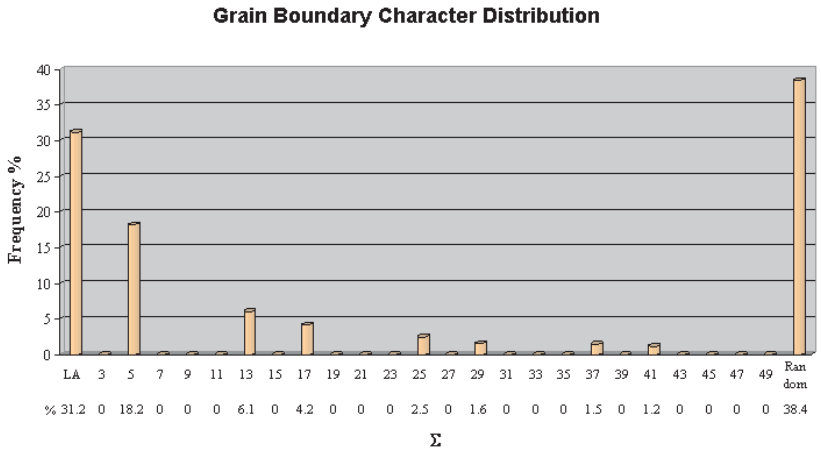

<100>

Σ5	36.9°
Σ13a	22.6°
Σ17a	28.1°
Σ25a	16.3°
Σ29a	43.6°
Σ37a	18.9°
Σ41a	12.7°

Figure 7-9 The GBCDs for simulations based on different fiber textured data. The coincident boundaries having the fiber axis as misorientation axis are listed next to the GBCD, together with the misorientation angle. The disorientation axis/angle pair is given additionally in brackets when the according misorientation is not the disorientation.

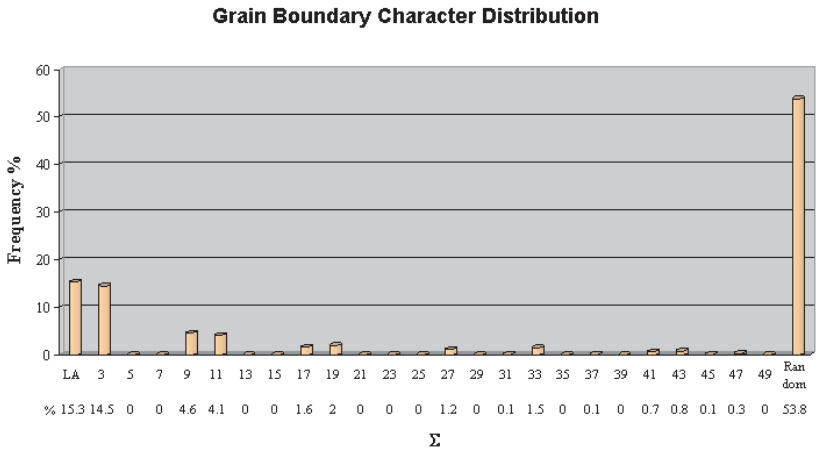

<110>

Σ3	70.5°	(<111>, 60°)
Σ9	38.9°	
Σ11	50.5°	
Σ17b	86.6°	(<221>, 61.9°)
Σ19a	26.5°	
Σ27a	31.6°	
Σ33a	20.1°	
Σ41c	55.9°	

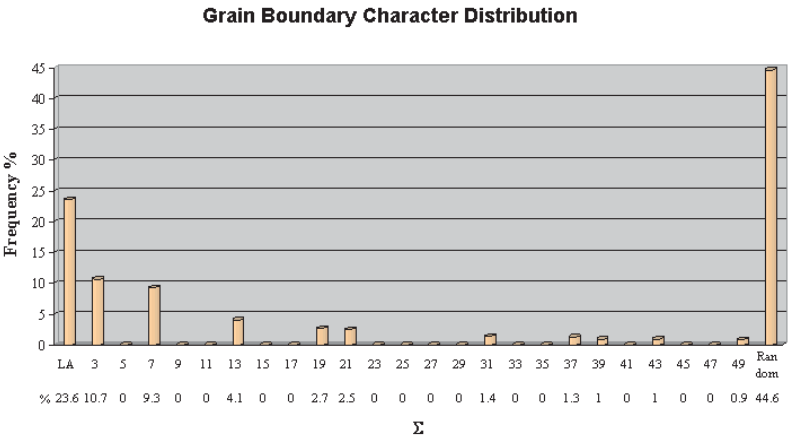

<111>

Σ3	60°
Σ7	38.2°
Σ13b	27.8°
Σ19b	46.8°
Σ21a	21.8°
Σ31a	17.9°
Σ37c	50.6°
Σ39a	32.2°
Σ43a	15.2°
Σ49a	43.6°

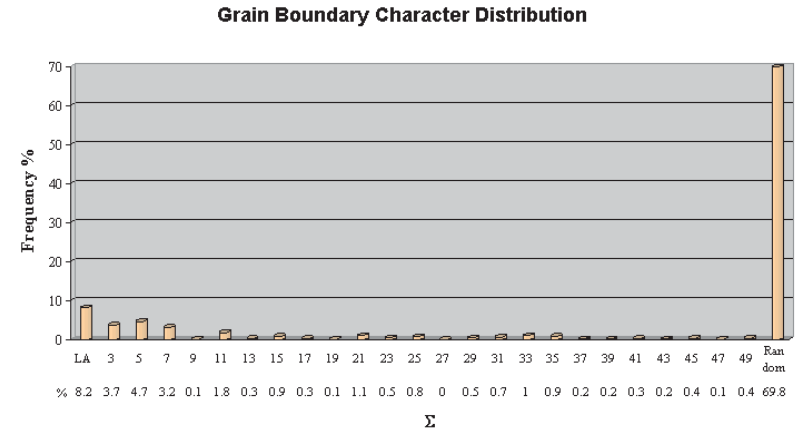

<112>

Σ3	180°	(<111>, 60)
Σ5	101.5°	(<100>, 36.9°)
Σ7	135.6°	(<111>, 38.2°)
Σ11	63°	(<110>, 50.5°)
Σ15	78.5°	(<210>, 48.2°)
Σ21b	44.4°	
Σ25b	156.9°	(<331>, 51.7°)
Σ31b	52.2°	
Σ33b	117°	(<311>, 33.6°)
Σ35a	34°	

Figure 7-9 (Continued)

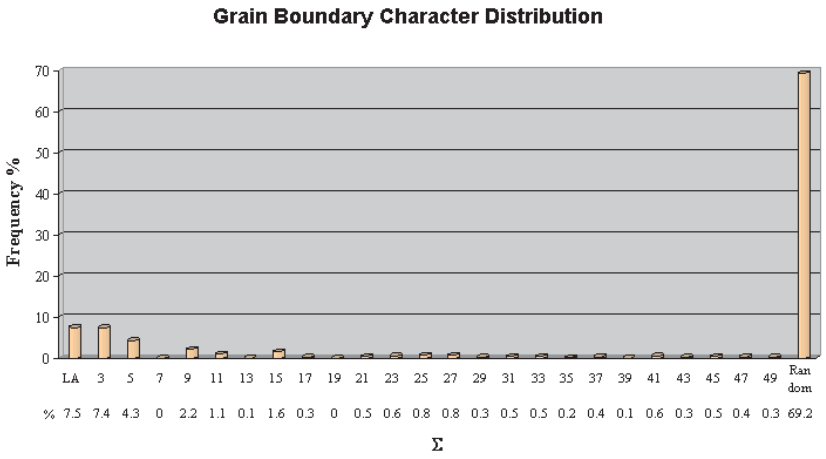

<113>

Σ3 146.4° (<111>, 60°)
Σ5 95.7° (<100>, 36.9°)
Σ9 67.1° (<110>,38.9°)
Σ11 180° (<110>, 50.5°)
Σ15 117.8° (<210>, 35.4°)
Σ23 40.5°
Σ25b 168.5 ° (<331>, 51.7 °)
Σ27b 79.3° (<210>, 35.4 °)
Σ31b 126.6° (<211>, 52.2°)
Σ33b 33.6°
Σ37b 109.8° (<310>, 43.1°)

Figure 7-9 (Continued)

7.4 Different Texture Strengths

Cube textured, *i.e.*, (001)[100], grains were used to define the influence of the texture strength. Data sets with different percentages of data within a 5 degrees deviation from the ideal cube orientation were used for these simulations, *i.e.*, 10, 20, 30, 40, 50, 60, 70, 80, 90 and 100%. The other data were simulated to have random texture. The final percentages of cube oriented data within 5 degrees deviation were determined with a texture strength calculation. The most interesting result in these simulations was the dependency of the frequency of LA and high angle grain boundaries on the texture strength. About 70 % of all data had to be within 5 degrees deviation from the ideal cube orientation to obtain a ratio of 1:1 for the low angle and high angle boundaries (Fig. 7-10).

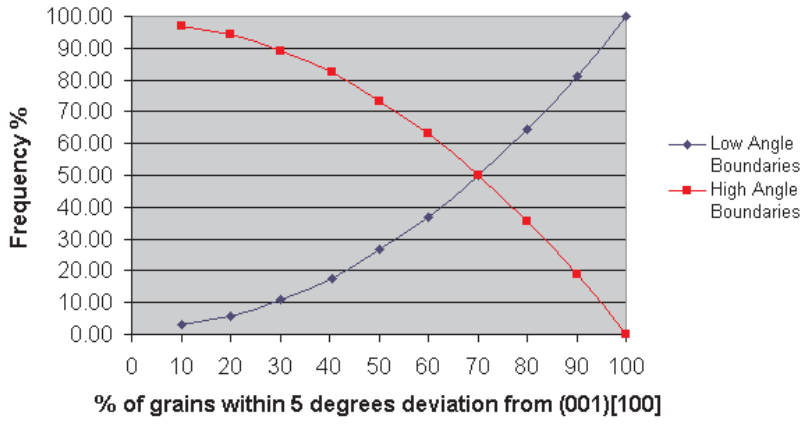

Figure 7-10 The frequency of low and high angle grain boundaries depends on the texture strength of the sheet texture. Data sets having 10.05, 20.04, 30.03, 40.05, 50.09, 60.03, 70.05, 80.04, 90.00 and 100 %, respectively, within a deviation of 5 degrees from the ideal cube orientation were used for these simulations.

8 Microtexture and Mesotexture Analysis of Measured Data

Several microtexture and mesotexture measurements on steel and copper samples were carried out during the present work. Because the main objective of this work changed in the course of the study from analyzing the materials microstructure and properties to the development of a data analysis method, a major part of the measurements can not be presented in this chapter. The measurements shown are used to demonstrate the data analysis capabilities of the developed program Yuki.

8.1 Various Samples

Before actual crystal orientation measurements were carried out, several different test materials were used to gather experience of the system and of the different possibilities for specimen preparation.

Old tungsten filaments, from a light bulb or from the electron source of SEM, are samples which can be recommended to every new user of the EBSD technique. Patterns obtained from the fresh, brittle fracture surface are of high quality due to the high atomic number of tungsten. They provide a good possibility to gather experience in using the system and to study different factors influencing the pattern quality, *e.g.*, the microscope operating parameters or the thickness of the carbon contamination layer.

Automated mechanical polishing with colloidal silica was tested as the final preparation step for steel samples, containing different carbides. EBSPs obtained from these samples were of good quality, however, the grain structure could not be seen in SE image. Also the use of the BE detector to obtain an orientation contrast image failed since the specimen surface was still too rough for contrast formation. A carefully polished flat surface is namely required to obtain a good orientation contrast. Moreover, the BE detector is not convenient to be used together with the EBSD system because it has to be mounted on the phosphor screen mount in forward scattering position. A larger specimen to screen distance and a bigger spot size than in EBSD operation is needed to obtain an orientation contrast image, which would then require a change of the working parameters every time a new specimen area is imaged.

As another example, the zinc coating of a galvanized steel plate required no particular specimen preparation in order to obtain EBSPs.

8.2 Hot Rolled Steel Specimens

The crystal orientations of 1765 individual grains in a hot rolled steel sheet were measured by EBSD. This material is used to produce rolls for the paper industry. Its microstructure is ferritic-pearlitic, the carbon content is about 0.1 and the average grain size is about 30 µm near the surface and 40 µm in the middle of the sheet. The thickness of the sheets used in the present work was 20 mm.
Specimens were prepared from the cross section of the sheet perpendicular to the TD. Grinding with SiC paper up to a mesh size of 1200 and mechanical diamond polishing with 3 µm and 1 µm diamond particle size were used as initial specimen preparation, followed by chemical etching with a 5% Nital etchant for 5-10 seconds, to reveal the microstructure and to remove the deformation layer.

8.2.1 Microtexture Studies

Microtexture studies were carried out in different depths below the sheet surface in order to investigate the through thickness variation of texture. Also samples from different positions in the sheet were studied. However, the different measurements did not show any significant differences in the texture. Therefore all measured data are presented together to illustrate the possibilities of data analysis.
The samples exhibited a fairly weak texture along the γ - fiber (ND ⊥ {111}) as well as along the ε-fiber. Fig. 8-1 and Fig. 8-2 show the {111} pole figure and the texture strength calculation results for typical texture components on these fibers, respectively.

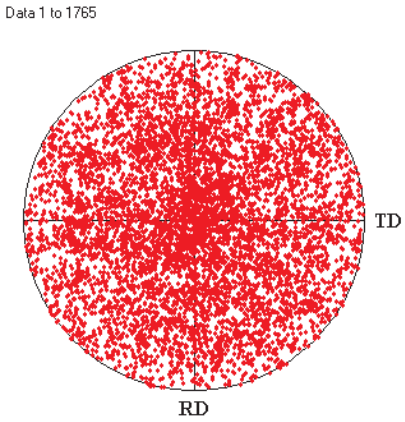

Figure 8-1 The {111} pole figure of 1765 measured grains.

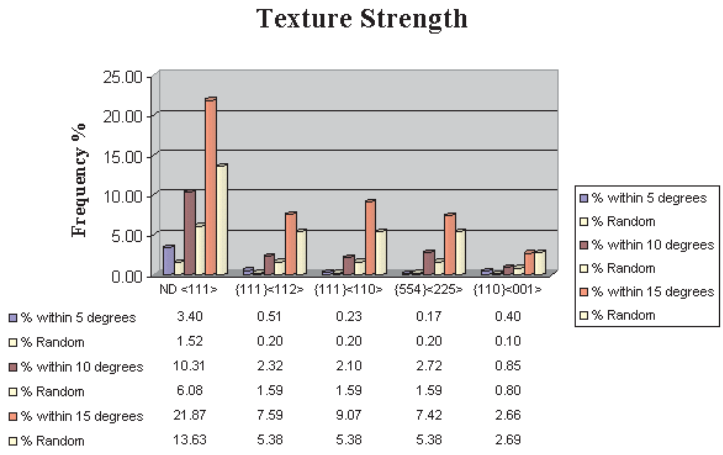

Figure 8-2 The texture strength calculation shows clearly that the hot rolled steel sheet has a weak texture.

A major advantage of the EBSD technique in comparison to macrotexture techniques is that the texture can be correlated to the microstructure. Crystal orientation maps can be very helpful when the spatial distribution of texture in the sample is studied.
One microtexture measurement from about 10 mm beneath the sheet surface has been chosen to serve as an example. All parameters needed for the different maps can be calculated within a few seconds by Yuki, the plotting of the maps themselves, however, is fairly time consuming, but those maps provide valuable information to understand the material's behavior.
Three different computer programs, *i.e.*, Gimp, Photoshop and Applixware Graphics were used to create the maps. Each of these programs includes different features, which are convenient to use but non of them alone is suitable for creating all different kinds of maps.
The orientations of 119 individual grains were measured. The micrographs were photographed by using dynamical focus and tilt correction in the SEM. The identification number of the orientation measurement for a specific grain was marked on a videoprint of the microstructure, allowing the correlation between the microstructure and the crystal orientation to be done later on.
The tilt correction distorts the image which, however, is negligible when the magnification is fairly high. The image of the microstructure is frozen on one of the two computer screens during EBSD operation, thus allowing the positioning of the beam with respect to the micrograph. In principle, the calibration of the EBSD system is only valid for the beam position in which the calibration was carried out, because changing the position of the beam will alter the specimen to screen distance and the position of the pattern center. Therefore also a rather high magnification has to be chosen to keep this error as small as possible. Thus, nine images of neighboring areas on the specimen surface were used to carry out the 119 orientation measurements. These nine images were fitted together to form one single image of the microstructure (Fig. 8-3).

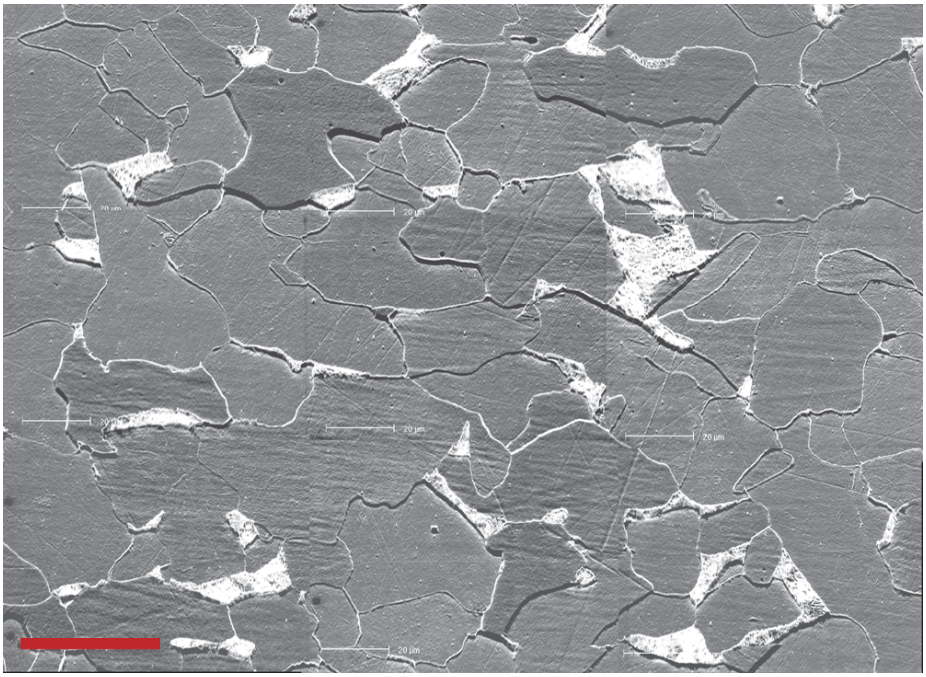

Figure 8-3 This image of the microstructure of the steel sheet is composed out of nine single images. The length bars can still be seen on each of these nine images. The red bar denotes 40 µm. Crystal orientation measurements were carried out of the ferritic grains, no patterns could be obtained from the pearlite.

Fig. 8-4 shows one possibility to create a crystal orientation map. Every grain is colored according to the orientation of one sample reference axis with respect to the crystal axes. A color key in the form of a unit triangle is used. Each reference axis has to be displayed in a single map. Pearlitic grains have a white color in these maps, because it was not possible to obtain EBSPs from the fine lamellae of the pearlite.
Another possibility is to color specific textured grains correspondingly. Fig. 8-5 shows grains within a deviation of 15 degrees from different ideal sheet texture orientations, colored according to the color key shown below the map. Fig. 8-6 presents all grains within 15 degrees from a ND <111> fiber texture, colored in dark, medium and light red for a maximum deviation of 5, 10 and 15 degrees from the ideal orientation. The grey grains are pearlite.
The maps indicate that textured grains tend to cluster, what could be associated to former austenite grains. The number of grains displayed in these maps, however, is fairly low. It would be necessary to investigate other micrographs to confirm this observation. Fig. 8-4 shows clearly the ND <111> texture.

Fig. 8-4 The grains are colored according to the orientation of RD and ND with respect to the crystal axes. The color key displayed next to the map is used. Pearlitic grains are colored in white.

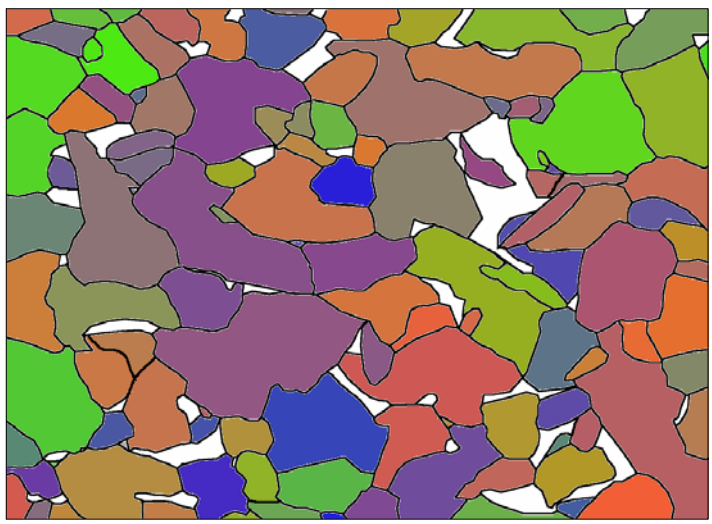

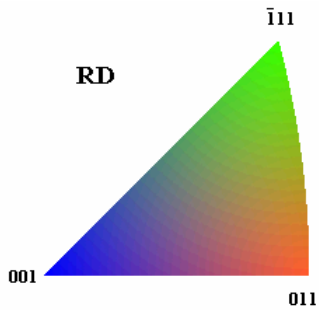
$\bar{1}11$
RD
001
011

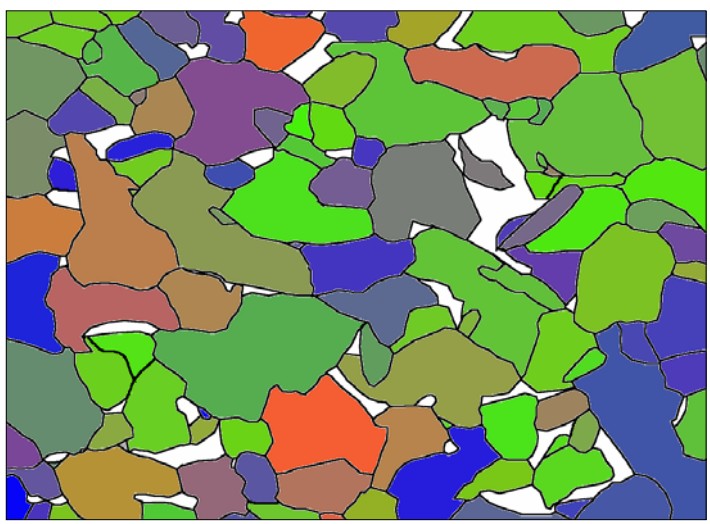

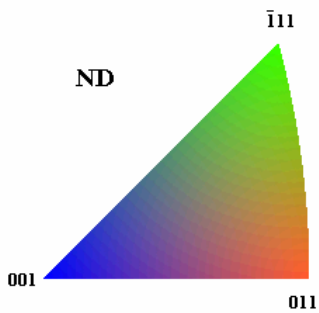
$\bar{1}11$
ND
001
011

Fig. 8-5 All grains within a deviation of 15 degrees from the ideal orientation of specific texture components are colored according the color key displayed below the map. Pearlite is colored in grey, all other grains in white.

Figure 8-6 The grains colored in dark, medium and light red are within a maximum deviation of 5, 10 and 15 degrees from a ND <111> fiber texture. Pearlite is colored in grey, all other grains in white.

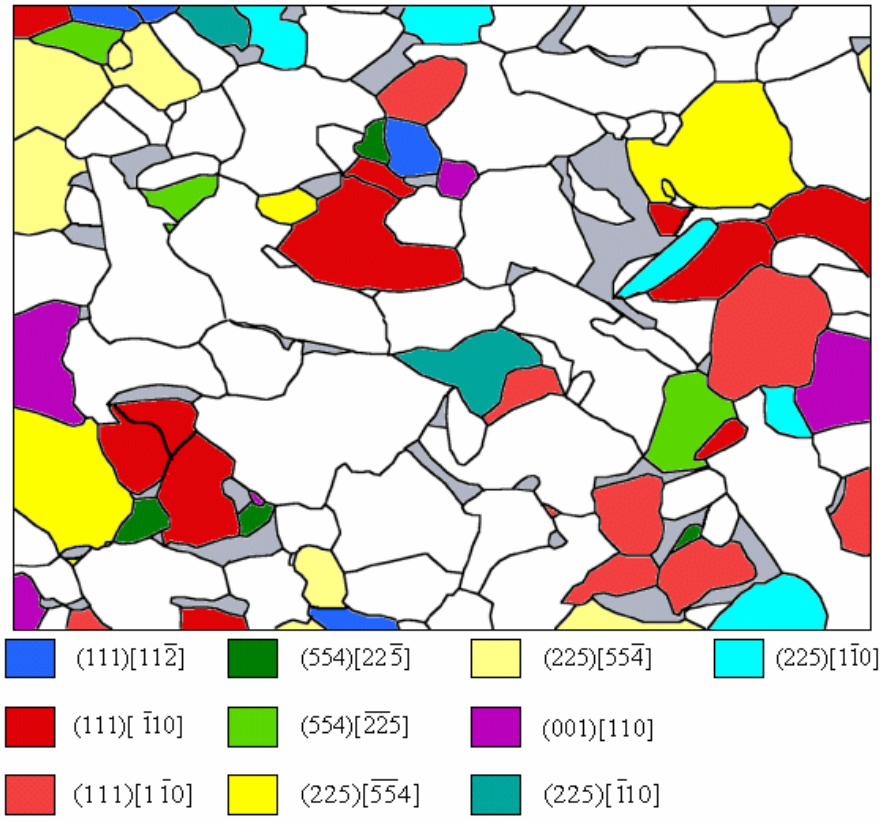
(111)[11$\bar{2}$]
(554)[22$\bar{5}$]
(225)[55$\bar{4}$]
(225)[1$\bar{1}$0]
(111)[$\bar{1}$10]
(554)[$\bar{2}\bar{2}$5]
(001)[110]
(111)[1 $\bar{1}$0]
(225)[$\bar{5}\bar{5}$4]
(225)[$\bar{1}$10]

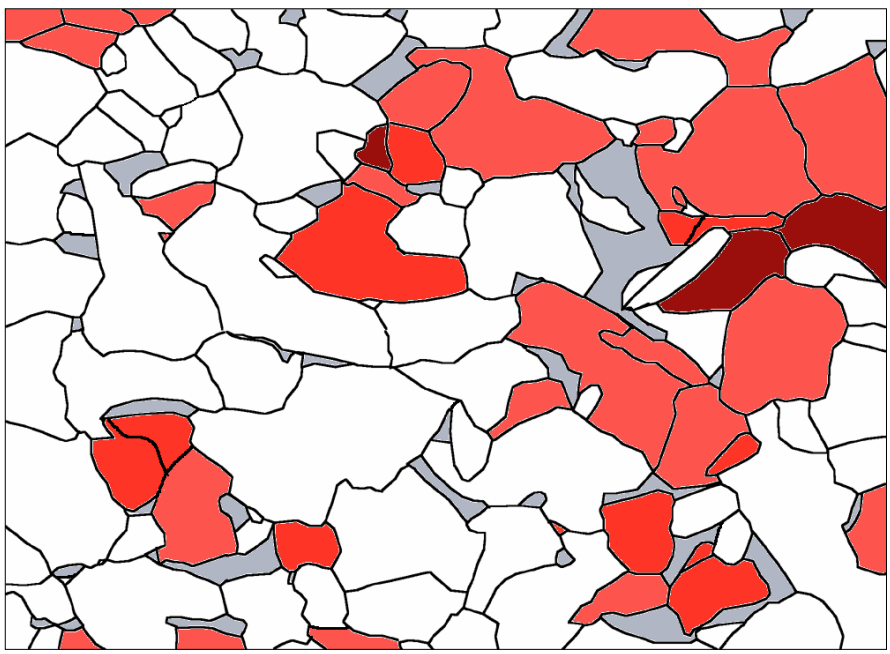

8.2.2 Mesotexture Studies

Totally, 2224 grain boundaries were analyzed to get the disorientation angle and axis distributions and the grain boundary character distribution (GBCD) shown in Figs. 8-7 and 8-8.

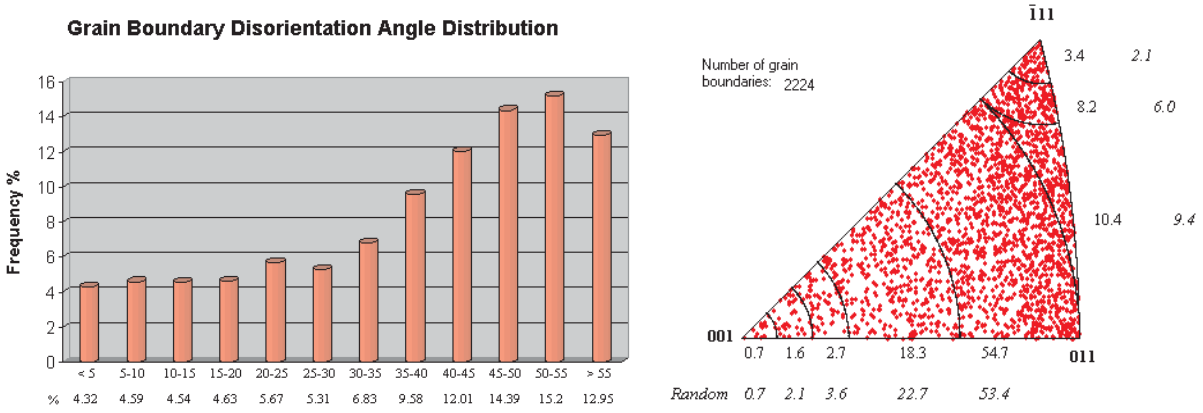

Figure 8-7 Disorientation angle and axis distribution.

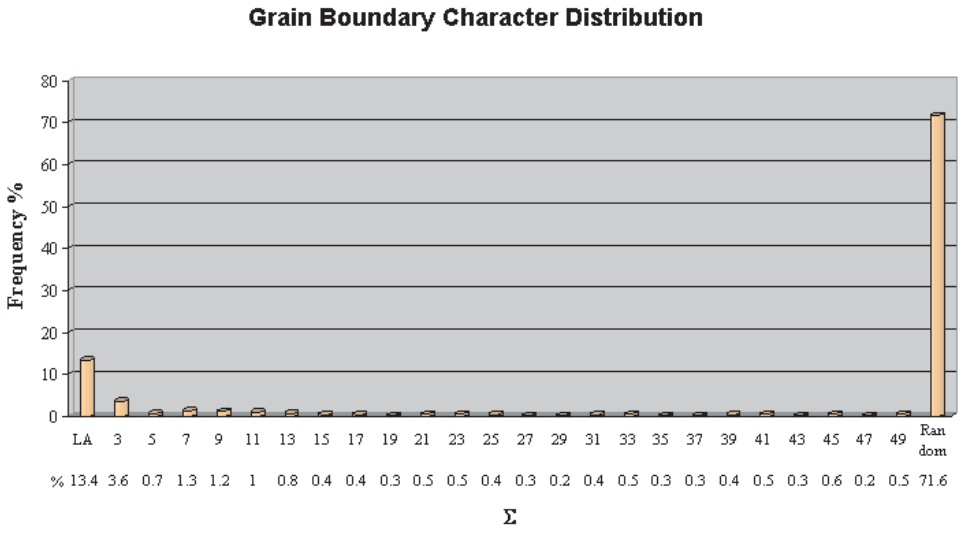

Figure 8-8 The GBCD of the 2224 grain boundaries.

It was recognized already during carrying out the measurements that a distinct dislocation substructure was present in the material. The pattern quality was good but the crystal orientation changed within the grains strongly. Deformation due to the specimen preparation, however, would normally introduce a uniformly distributed deformation which decreases remarkably the pattern quality. Probably the temperature at the end of hot rolling was already too low to allow full recrystallization, but recovery could still take place forming a subgrain structure.
Thus, a high fraction of LA boundaries was expected, and indeed, it turned out to be 13.4%. Because of the subgrain structure it was fairly difficult to identify grain boundaries by the pattern change, and therefore only those revealed by the chemical etching were used for the analysis.

Additionally, the GBCD indicates a fairly high amount of Σ 3 boundaries, also to recognize in the higher amount of boundaries with a disorientation angles > 55 ° and in the clustering of disorientation axes near the <111> directions.

The simulation of the grain boundary structure, carried out with the measured data, showed a random grain boundary geometry distribution. This was expected because the simulations with the generated data already indicated that the texture has to be strong to influence the GBCD.

The temperature during the hot rolling process is high enough to allow energy minimization to some extent, thus increasing probably the fraction of low energy boundaries such as low Σ value boundaries.

Similar to the crystal orientation maps, grain boundary maps were plotted using the same micrograph. Fig. 8-9 presents all random boundaries as blue, LA boundaries as green and coincident boundaries (Σ_{max} = 49) as yellow dashed lines. The Σ value as well as the relative deviation ν / ν_m , where ν is the actual deviation and ν_m is the maximum deviation according to the Brandon criterion, is given next to the specific grain boundary. The relative deviation is given for the LA boundary as well, where ν_m is 15 degrees. Boundaries to pearlite are plotted in black. In the same way, any other feature someone would like to look at could be drawn in a different color. As an example, Fig. 8-10 shows all grain boundaries having a higher disorientation angle than 50 degrees in red. The disorientation angle is given next to the grain boundary.

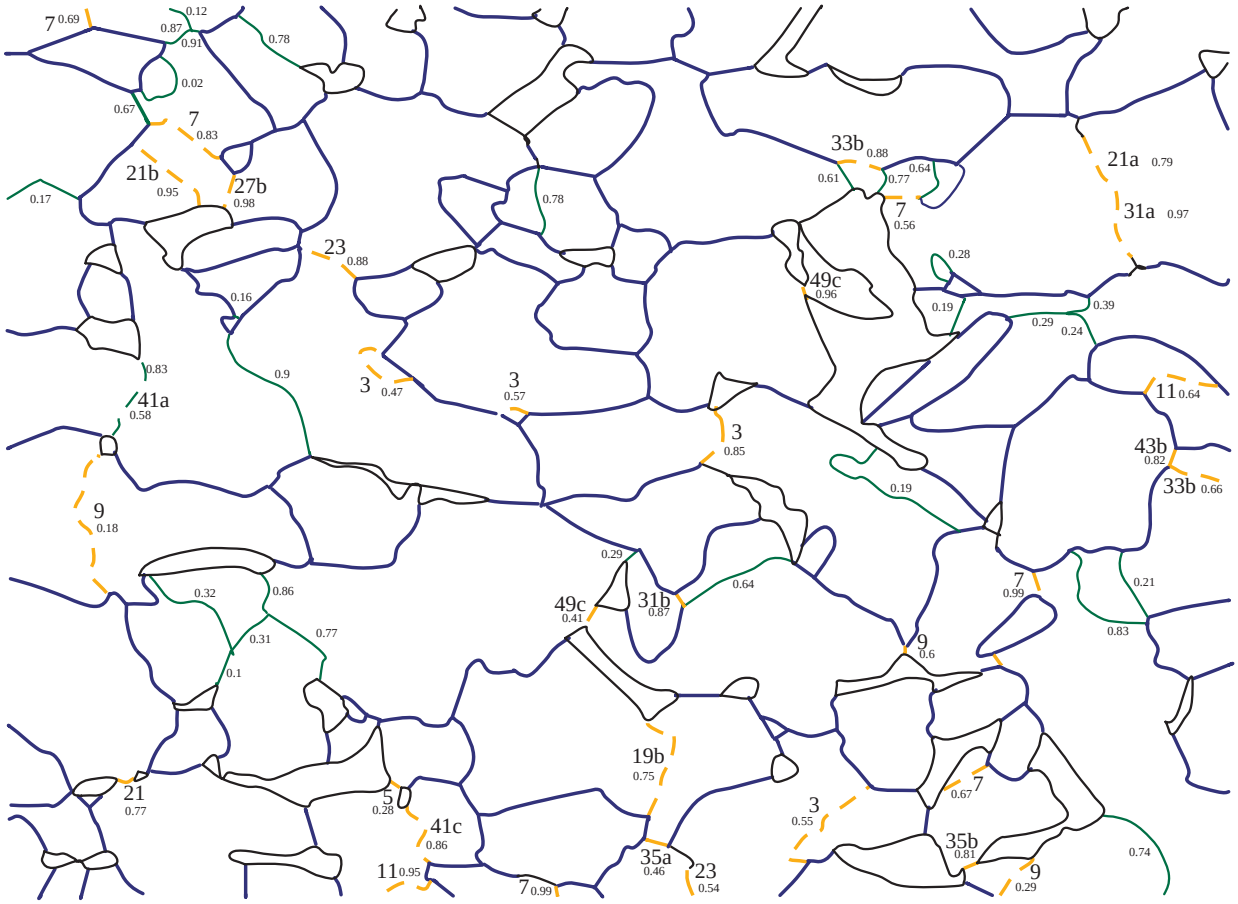

Figure 8-9 A typical grain boundary map.

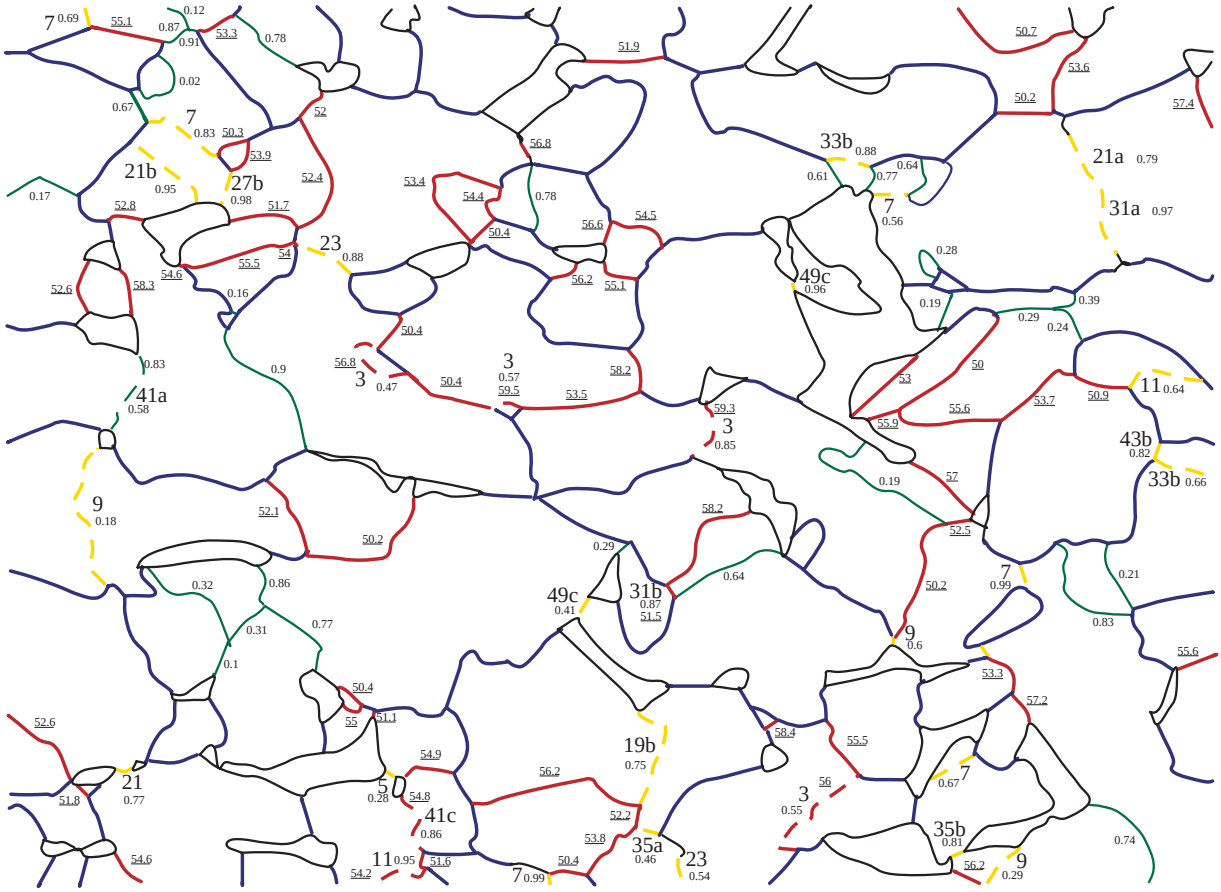

Figure 8-10 All grain boundaries having a higher disorientation angle than 50 degrees are displayed in red.

8.3 Copper Specimens

About 1500 measurements on different OFHC copper sheet samples were carried out. The full analysis of all the measurements was, however, out of the scope of this work. Therefore, just two examples are briefly shown.

Copper specimens were at first ground up to a 4000 mesh size silicon paper, followed by diamond polishing with 3 and 1 µm particle size and electropolishing with a solution of methanol and nitric acid below -35 degrees. Etching with the Cu5 solution as a final preparation step did not allow to obtain any patterns from the sample. Mechanical polishing with alumina or colloidal silica suspension prior to electropolishing resulted in a surface layer causing difficulties during electropolishing. Experiments showed that the layer produced by the colloidal silica did not dissolve even in concentrated nitric acid, while the rest of the copper sample did.

A technique for continuous casting of copper sheets is under development at Outokumpu Copper Pori. Various copper samples related to this production route were investigated in the present work, *i.e.*, as-cast, rolled and annealed sheets. Results

obtained on these materials were compared to those from conventionally produced sheets (*i.e.*, cast, hot rolled, cold rolled and annealed). Only two examples of the results will be presented below, *i.e.*, the GBCD in the continuously cast sheet and the texture of the cast and cold rolled sheet material.

The continuous casting works as following; an slitted tube is up-cast, opened by special tools and coiled. The mold for the tube is water cooled only from the outside, the sheet is pulled a few millimeters, stopped for a short time to allow solidification, pulled again, etc.

The sample investigated was produced with the highest speed which was possible to use with the equipment available. In this case, the cooling time in the mold itself is very short. The sheet exhibited a strong oxide layer on the surface, which means that it was still very hot when it came out of the mold. Grains which nucleated at the surface had enough time to grow as columnar grains through the whole sheet thickness, showing a strong solidification <001> fiber texture. The thickness of the sheet was about 11 mm and the average grain size in the sheet plane about 500 µm.

8.3.1 GBCD of the ND <001> Fiber Textured Copper Sheet

The as-cast material showed in the middle of the sheet thickness a strong ND <001> fiber texture (Fig. 8-11). A measurement of 45 individual grains is selected to illustrate the influence of such texture on the GBCD. Most of the grains had a regular hexagonal shape. 108 grain boundaries and 62 triple lines were analyzed. The results are presented in Table 8-1.

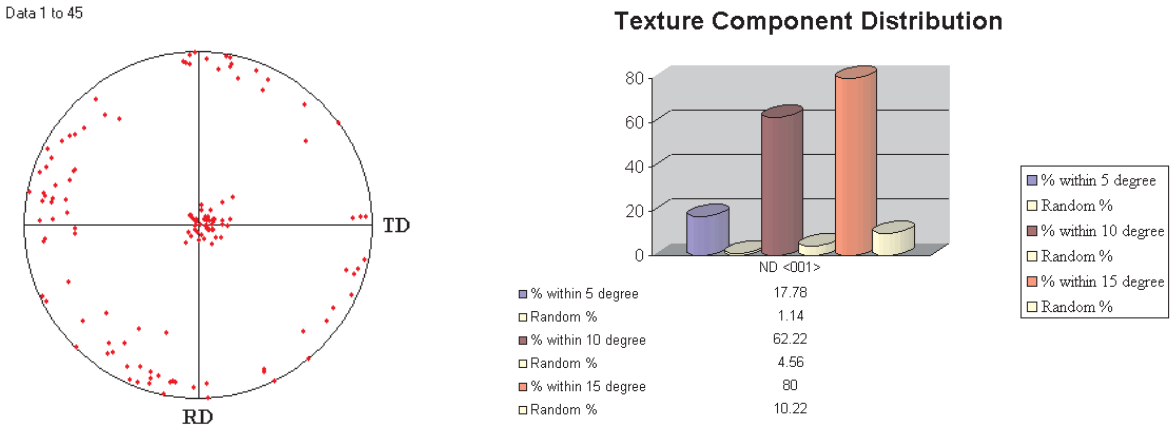

Figure 8-11 The {100} pole figure and the result of the texture strength calculation for ND <001> fiber texture.

Table 8-1 GBCD and the triple line distribution; only the listed Σ values were present within the 108 grain boundaries investigated.

GBCD		Triple Lines	
Σ 1 (LA)	35.2 %	0 special boundaries	21 %
Σ 5	2.8 %	1 special boundary	40.3 %
Σ 7	0.9 %	2 special boundaries	25.8 %
Σ 13a	0.9 %	3 special boundaries	12.9 %
Σ 19a	0.9 %		
Σ 23	2.8 %		
Σ 27b	0.9 %		
Σ 41a	0.9 %		
Random	55.6 %		

Due to the fairly low number of analyzed grain boundaries the results are not statistically reliable, but still some tendencies can be found in comparison with grain boundary simulation. Those would have to be confirmed by analyzing a higher number of data, as well as by using statistical tests like the χ^2 test or the Kolmogorov-Smirnov test. The first simulation used for comparison utilizes ND <001> textured simulated data having a maximum deviation of 15 degrees from the ideal orientation (Simulation I). Secondly, 14,000 grain boundaries were simulated from the 45 measured grain orientations (Simulation II). In principle, only 990 different grain boundaries can be constructed from the 45 grains. A far higher number of grain boundaries had to be selected since the random number generator is used for the simulations.
The most obvious difference is that the fraction of LA boundaries is much higher for the measured data (35.2 %) than for the simulated ones (Simulation I: 14.4 %; Simulation II: 21,2 %). This indicates solidification favors formation of LA boundaries. This, in turn, influences the triple line character distribution, increasing the amount of triple lines where 2 or 3 special grain boundaries meet.

8.3.2 Cold Rolled Copper Sheet

As a last example of data analysis, an ODF of a continuously cast and cold rolled copper sheet using the Euler angles calculated by Yuki is shown. This method can be very useful when comparing the microtexture data to the macrotexture measurements.
The thickness of the cold rolled sheet was about 0.6 mm. The thickness reduction of the sheet is about 90 %, if it is assumed that a 1 mm layer has been mechanically removed on each sheet side before rolling to remove the surface oxide. The pattern quality, in spite of the heavy cold deformation, was still very good.
An alternative method for data collection was used for this sample. The measurements were not taken from individual grains like in earlier studies, but the microscope stage was moved stepwise by 50 µm and an orientation measurement was taken at the current position. The data could be collected in a fairly short time and one got a fast impression of the texture present in the sample. The two measuring methods, however,

will not give the same result in all cases. It is more probable to take a measurement from a big grain than from a small grain when the stage movement method is used, which means that in the collected data more weight is put on big grains, similar to X-ray macrotexture data. In the grain by grain method, the influence of the grain size is excluded.

The ODF was generated using 100 grains from the sample, the inverse pole figure of which has been already shown in Fig. 5-7, and the {110} pole figure in Fig. 6-2. Fig. 8-12 presents the ODF of this microtexture measurement showing a typical copper rolling type texture.

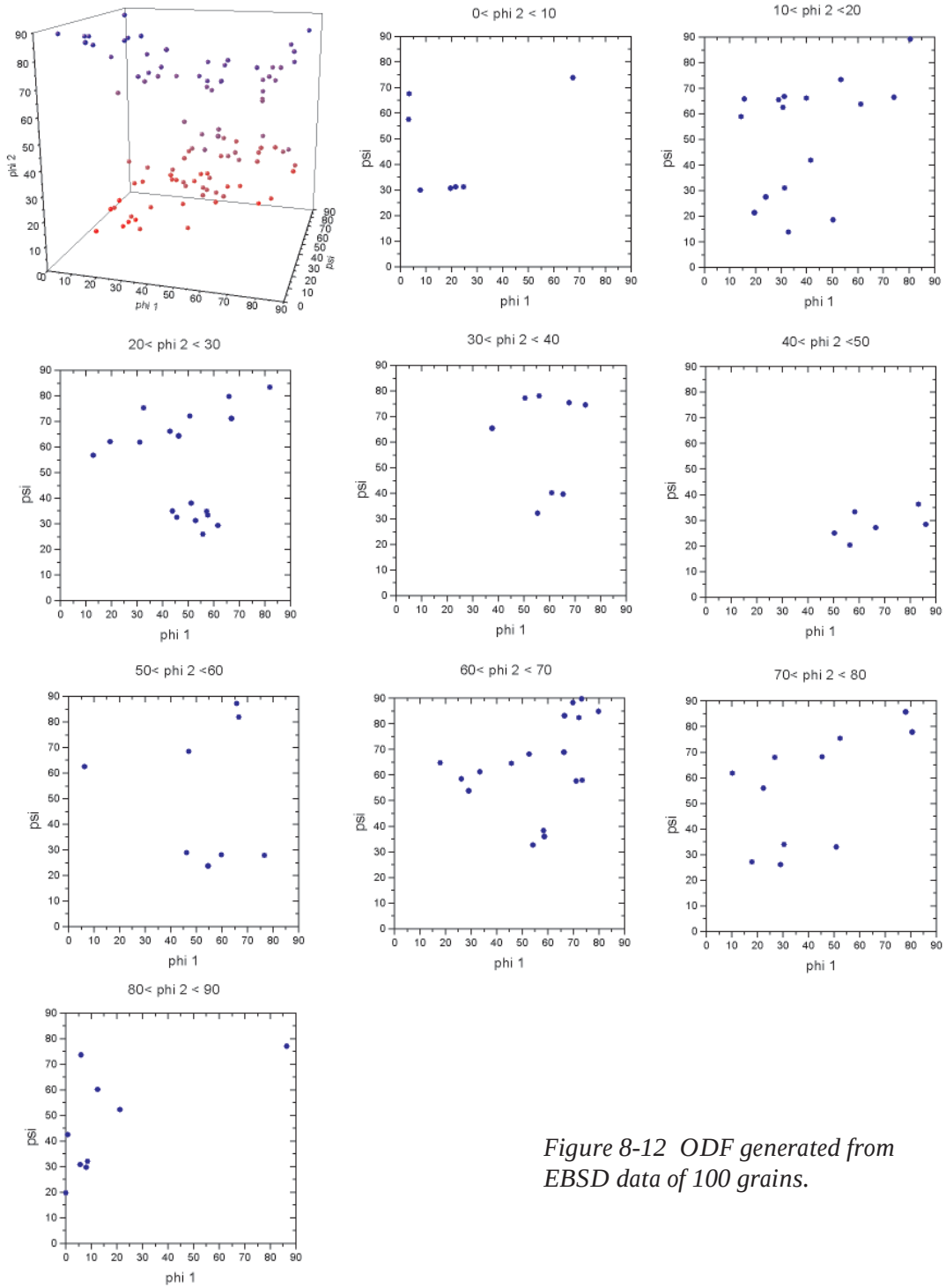

Figure 8-12 ODF generated from EBSD data of 100 grains.

9 Summary and Outlook

The original aim of the present work was to study the capabilities of an EBSD system, installed at CEM in 1996, and to gather experience of its use for different applications.
A broad literature review was first done to increase the knowledge about the application possibilities of the EBSD technique in the fields of microtexture and mesotexture studies, phase identification and strain measurement.
The EBSD system at CEM was used for the first time, and therefore initial settings and calibrations were first done. Spacers were designed to allow working with the two position calibration method.
The commercial indexing and analyzing software delivered with the system is inconvenient to use, since it runs only on the microscope control computer. It is very time consuming to analyze a higher number of data with it, especially when grain boundaries are studied. Additionally, only a few basic analyzing methods are provided. Moreover, some of the analyzing results were incorrect due to various bugs in the software, *e.g.*, a mixing of left and right-handed coordinate systems during indexing. Therefore it was decided to focus on the development of a stand-alone EBSD data analyzing software for microtexture and mesotexture studies on cubic materials with the point group $m\bar{3}m$.
'Yuki - An EBSD Analyzing Tool' was developed under Visual Basic 5.0 allowing the conduction of microtexture and mesotexture analysis in a fairly short time.
One of the various features included in Yuki is the possibility to perform simulations of the texture influence on the grain boundary geometry distribution. In different ways textured simulated data sets were used to illustrate these relationships. Additionally, the simulations with randomly simulated orientation matrices comprise a random reference for mesotexture studies on real samples.
Finally, the capabilities of Yuki were shown by the use of measured data from steel and copper samples. Orientation data of 1765 grains and 2224 grain boundaries of a hot rolled steel sheet were analyzed, also with the help of crystal orientation and grain boundary maps. About 1500 orientation data were collected from various copper sheet samples. Only two examples of this data are briefly shown in this thesis, since its main focus was to outline the data analysis.
For the future, it would be convenient to include some additional features into the developed software, *i.e.*, contour line plots and ODFs and Rodrigues vectors plots. Moreover, the analyzing capabilities of Yuki could be extended to materials having other crystal systems than cubic, especially the hcp crystal system would be relevant. However, the additional work necessary to include these features should not be underestimated.

10 References

Alam, M. N., Blackman, M. & Pashley, D.W. (1954), High-angle Kikuchi patterns. *Proceedings of the Royal Society A*, **221**, pp. 224-242.

Baudin, T., Chastel, Y. & Penelle, R. (1997), Strain estimation by electron back scattered diffraction, *Proceedings of Microscopy and Microanalysis 1997,* pp. 569-570.

Blochwitz, C., Brechbühl, J. & Tirschler, W. (1996), Analysis of activated slip systems in fatigued nickel polycrystals using the EBSD-technique in the scanning electron microscope, *Mat. Sci. Eng.* **A210**, pp. 42-47.

Buchgraber, W. (1996), Untersuchung des Einflusses von Versuchsparametern und plastischer Verformung auf die Linienschärfe von Electron Back Scatter Diffraction Patterns, Diplomarbeit, Montanuniversität Leoben.

Caul, M. D. & Randle, V. (1996), Grain-boundary characteristics in austenitic steel, *Proceedings of Microscopy and Microanalysis 1996*, pp. 344-345.

Cizek, P., Wynne, B. P., Hong Lu & Parker, B. A. (1996), Deformation banding in (001)[110] textured aluminium sheet deformed in tension, *Mat. Sci. Eng.* **A219**, pp. 44-55.

Davies, R. & Randle, V. (1997), Application of crystal orientation mapping to intragrain misorientations, *Proceedings of Microscopy and Microanalysis 1997*, pp. 563-564.

Day, A. & Shafirstein, G. (1996), Assessment of local residual strain by electron backscatter patterns and nanoindentation, *Mat. Sci. Tech.* **12**, pp. 873-879.

Dingley, D. J. & Randle, V. (1992). Microtexture determination by electron backscatter diffraction, *Journal of Materials Science* **27**, pp. 4545-4566.

Dingley, D. J., Baba-Kishi, K. Z. & Randle V. (1995), Atlas of Backscattering Kikuchi Diffraction Patterns, Microscopy in Materials Science Series, *IOP Publishing Ltd*, ISBN 0 7503 02 12 7.

Driver, J. H., Theyssier, M.-C. & Maurice, Cl. (1996), Electron backscattered diffraction microtexture studies on hot deformed aluminium crystals, *Mat. Sci. Tech.* **12**, pp. 851-858.

Engler, O. (1996), Nucleation and growth during recrystallisation of aluminium alloys investigated by local texture analysis, *Mater. Sci. Technol.* **12**, pp. 859-872.

Engler, O. , Hirsch, J. & Lücke, K. (1995), Texture Development in Al-1.8 wt% Cu depending on the precipitation state - II. Recrystallization textures, *Acta metall. mater.* **43**, pp. 121-138.

Field, D. P. & Dingley, D. J. (1995), Microtexture analysis in aluminium thin films, Reprint from the **november 1995** edition of *Solid State Technology*.

Field, D. P. & Dingley, D. J. (1996), Microstructure Mapping of Interconnects by Orientation Imaging Microscopy, *Journal of Electronic Materials* **25**, pp. 1767-1771.

Furley, J. & Randle, V. (1991), Mesotexture in annealed nickel, *Mat. Sci. Tech.* **7**, pp. 12-19.

Gleiter, H. (1982), On the Structure of Grain Boundaries in Metals, Review Paper, *Mat. Sci. Eng.* **52**, pp. 91-131.

Goyal, A., Specht, E. D., Wang, Z. L. & Kroeger, D. M. (1997), Grain Boundary studies of high-temperature superconducting materials using backscatter Kikuchi diffraction, *Ultramicroscopy* **67**, pp. 35-57.

Grain Boundary Structure and Kinetics (1980), Materials Science Seminar, Milwaukee 1979, *American Society of Metals*, ISBN 0-87170-097-2.

Harris, K. E., Ebrahimi, F. & Garmestani, H. (1998), Texture evolution in NiAl, *Mater. Sci. Eng.* **A247**, pp. 187-194.

Hawkes, P. (1998). A Century of Electrons, *European Microscopy and Analysis* **51**, pp. 5-8.

Hey, T. & Walters, P. (1998), Das Quantenuniversum: Die Welt der Wellen und Teilchen, *Spektrum, Akad. Verl.*, ISBN 3-8274-0315-4, original titel - The quantum universe, Cambridge University Press 1987.

Hjelen, J., Lewin, E. & Vatne, H. E. (1996), Determination of fracture facet crystallography by the use of electron back-scatter patterns, *Proceedings Eurem Dublin 1996*, CD-ROM.

Hjelen, J., Orsund, R. & Nes, E. (1991), On the origin of recrystallization textures in aluminium, Overview No. 93, *Acta metall. mater.* **39**, pp. 1377-1404.

Huin Lin & Pope, D. P. (1995), Weak grain boundaries in Ni_3Al, *Mat. Sci. Eng.* **A192/193**, pp. 394-398.

Humphreys, C. J. (1979). The scattering of fast electrons by crystals, *Rep. Prog. Phys.* **42.**

Joy, D. C., Newbury, D. E. & Davidson, D. L. (1982), Electron channeling patterns in the scanning electron microscope, *J. Appl. Phys.* **53**, pp. 81-122.

Juul Jensen, D. (1995), Growth rates and misorientation relationships between growing nuclei/grains and the surrounding deformed matrix during recrystallization, *Acta metall. mater.* **43**, pp. 4117-4129.

Kenik, E. A. (1996), Spatial resolution of electron backscatter diffraction in a FEG-SEM, *Proc. of Microscopy and Microanalysis 1996,* pp. 348-349.

Krieger Lassen, N. C. (1994), Automated Determination of Crystal Orientations from Electron Backscattering Patterns, *PhD Thesis, Institut of Mathematical Modelling, Lyngby.*

Kuokkala, V.-T. (1995), Electron Microscopy II, Lecture Notes, Tampere University of Technology.

Lehockey, E. M., Palumbo, G., Lin, P. & Brennenstuhl, A. (1996), On the relationship between grain-boundary character distribution and intergranular corrosion, *Proceedings of Microscopy and Microanalysis 1996*, pp. 346-347.

Lejcek, P. & Hofmann, S. (1995), Thermodynamics and Structural Aspects of Grain Boundary Segregation, *Critical Reviews in Solid State and Materials Science* **20(1)**, pp. 1-85.

Liu, W., Bayerlein, M., Mughrabi, H., Day, A. & Quested, P. N. (1992), Crystallographic features of intergranular crack initiation in fatigued copper polycrystals, *Acta metall. mater.* **40**, pp. 1763-1771.

Liu, Y. L., Hsun Hu & Hansen, N. (1995), Deformation and recrystallysation of a channel die compressed aluminium bicrystal with (112)[111] / (123)[412] orientation, *Acta metall. mater.* **43**, pp. 2395-2405.

Mackenzie, J. K. (1964), The distribution of rotation axes in a random aggregate of cubic crystals, *Acta metall.* **12**, pp. 223-225.

Matsuomoto, K., Shibayanagi, T. & Umakoshi, Y. (1997), On the role of grain boundary character distribution in grain growth of Al-Mg alloys, *Acta Mater.* **45**, pp. 439-451.

Michael, J. R. (1997), All you need to know about electron backscatter diffraction: Orientation is only the tip of the iceberg, *Proceedings of Microscopy and Microanalysis 1997*, pp. 387-388.

Michael, J. R., Schlienger, M. E. & Goehner, R. P. (1997), Electron Backscatter Diffraction in the SEM: Is electron diffraction in the TEM obsolete?, *Proceedings of Microscopy and Microanalysis 1997*, pp. 879-880.

Miodownik, M. A., Wilkinson, A. J. & Martin, J. W. (1998), On the secondary recrystallisation of MA754, *Acta mater.* **46**, pp. 2809-2821.

Mishin, O. V. & Gottstein, G. (1998), Grain boundary ensembles due to growth in copper with strong recrystallization texture, *Mat. Sci. Eng.* **A249**, pp. 71-78.

Mulvey, T. (1989). The electron microscope: the British contribution, *Journal of Microscopy* **155**, pp. 327-338.

Palumbo, G. & Aust, K. T. (1990), Structure-dependence of intergranular corrosion in high purity nickel, *Acta metall. mater.* **38**, pp. 2343-2352.

Palumbo, G., Lehockey, E. M. & Lin, P. (1997), Application of microdiffraction in SEM for assessing intrinsic materials susceptibility to intergranular corrosion and stress corrosion cracking, *Proceedings of Microscopy and Microanalysis 1997*, pp. 573-574.

Palumbo, G., Lehockey, E. M., Lin, P., Erb, U. & Aust, K. T. (1996), Grain Boundary engineering for intergranular fracture and creep resistance, *Proceedings of Microscopy and Microanalysis 1996*, pp. 362-363.

Panchanadeeswaran, S., Doherty, R. D. & Becker R. (1996), Direct observation of orientation change by channel die compression of polycrystalline aluminium-use of a split sample, *Acta mater.* **44**, pp. 1233-1262.

Park, Y. B., Lee, D. N. & Gottstein, G. (1998), The evolution of recrystallization textures in body centered cubic metals, *Acta mater.* **46**, pp. 3371-3379.

Priester, L. (1989), Geometrical speciality and special properties of grain boundaries, *Revue Phys. Appl.* **24**, pp. 419-438.

Quested, P. N., Henderson, P. J. & McLean, M. (1988), Observation of deformation and fracture heterogeneities in a nickel-base superalloy using electron back scattering patterns, *Acta metall.* **36**, pp. 2743-2752.

Randle, V. & Brown, A. (1988), The effects on grain misorientation texture during the grain growth incubation period, *Phil. Mag. A* **58,** pp. 717-736**.**

Randle, V. & Brown, A. (1989), Development of grain misorientation texture, in terms of coincident site lattice structures, as a function of thermomechanical treatments, *Phil. Mag. A* **59**, pp. 1075-1089.

Randle, V. (1991), Influence of kinetic factors on the distribution of grain boundary planes in nickel, *Mat. Sci. Tech.* **7**, pp. 985-990.

Randle, V. (1992), Microtexture Determination and its application, 174 pages, *The Institute of Materials, ISBN 0-901716 35 9.*

Randle, V. (1993), The measurement of grain boundary geometry, *Institute of Physics Publishing*, ISBN 0-7503-0235-6.

Randle, V. (1995), An investigation of grain-boundary plane crystallography in polycrystalline nickel, *J. Mat. Sci.* **30**, pp. 3983-3988.

Randle, V., Hansen, N. & Juul Jensen, D. (1996), The deformation behaviour of grain boundary regions in polycrystalline aluminium, *Phil. Mag. A* **73**, pp. 265-282.

Randle, V., Ralph, B. & Dingley, D. (1988), The relationship between microtexture and grain boundary parameters, *Acta metall.* **36**, pp. 267-273.

Samajdar, I., Verlinden, B. & van Houtte, P. (1998), Development of recrystallization texture in IF-steel: an effort to explain developments in global texture from microtextural studies, *Acta mater.* **46**, pp. 2751-2763.

Schwartz, A. J., Lassila, D. H. & LeBlanc, M. M. (1998), The effects of tungsten addition on the microtexture and mechanical behavior of tantalum plate, *Mat. Sci. Eng.* **A244**, pp. 178-190.

Semprimoschnig, C. O. A. (1996), Die kristallographische Fraktometrie - Entwicklung einer Methode zur quantitativen Analyse von Spaltbruchflächen, Dissertation, *Montanuniversität Leoben*.

Shvindlerman, L. S. & Straumal, B. B. (1985), Regions of existance of special and non-special grain boundaries, *Acta metall.* **33**, pp. 1735-1749.

Slavik, D. C., Wert, J. A. & Gangloff, R. P. (1993), Determining fracture facet crystallography using electron backscatter patterns and quantitative tilt fractography, *J. Mater. Res.* **8**, pp. 2482-2491.

Sutton, A. P. & Balluffi, R. W. (1987), On geometric criteria for low interfacial energy, *Acta metall.* **35**, pp. 2177-2201.

TSL, Advanced materials analysis via Orientation Imaging Microscopy™ (OIM™), TSL Techniqual Note, TexSEM Laboratories.

Tacikowski, M., Grabski, M. W., Driver, J. & Kobylanski, A. (1996), The effect of carbon and sulphur on the character of the grain boundary population in α-iron, *Mat. Sci. Eng.* **A205**, pp. 133-138.

Thomson, C. B. & Randle, V. (1996), Towards optimization of grain-boundary structures in annealed nickel, *Proceedings of Microscopy and Microanalysis 1996*, pp. 356-357.

Thomson, C. B. & Randle, V. (1997), The effects of strain annealing on grain boundaries and secure triple junctions in nickel 200, *J. Mat. Sci.* **32**, pp. 1909-1914.

Troost, K. Z. (1993), Assessment of implantation damage by backscatter Kikuchi diffraction in the scanning electron microscope, *Appl. Phys. Lett.* **63**, pp. 958-960.

Troost, K. Z., van der Sluis, P. & Gravesteijn, D. J. (1993), Microscale elastic-strain determination by backscatter Kikuchi diffraction in the scanning electron microscope, *Appl. Phys. Lett.* **62**, pp. 1110-1112.

Vatne, H. E., Karlsen, M. & Hjelen, J. (1996), Determination of lattice plane spacings from electron back-scatter patterns, *Proceedings Eurem Dublin 1996*, CD-ROM.

Venables, J. A. & Bin-Jaya, R. (1977), Accurate microscrystallography using electron back-scattering patterns, *Phil. Mag.* **35**, pp. 1317-1332.

Venables, J. A. & Harland, C. J. (1973), Electron back-scattering patterns - A new technique for obtaining crystallographic information in the scanning electron microscope, *Phil.Mag* **27**, pp. 1193-1200.

Watanabe, T. (1993), Grain boundary design and control for high temperature materials, *Mat. Sci. Eng* **A166**, pp. 11-28.

Watanabe, T. (1994), The impact of grain boundary character distribution on fracture in polycrystals, *Mat. Sci. Eng.* **A176**, pp. 39-49.

Watanabe, T. (1996), SEM-ECP analysis of grain-boundary character distribution in polycrystalline materials, *Proceedings of Microscopy and Microanalysis 1996*, pp. 354-355.

Watanabe, T., Fujii, H., Oikawa, H. & Arai, K. I. (1989), Grain Boundaries in rapidly solidified and annealed Fe-6.5 mass% Si polycrystalline ribbons with high ductility, *Acta metall.* **37**, pp. 941-952.

Watanabe, T., Suzuki, Y., Tanii, S. & Oikawa, H. (1990), The effects of magnetic annealing on recrystallization and grain boundary character distribution (GBCD) in iron-cobalt alloy polycrystals, *Phil. Mag. Lett.* **62**, pp. 9-17.

Weiland, H. (1997), In situ observation of deformation processes by OIM, *Proceedings of Microscopy and Microanalysis 1997*, pp. 567-568.

Weiland, H., Field, D. P. & Adams, B. L. (1995), In-situ observation of orientation changes on metallic surfaces, *Proceedings of Microscopy and Microanalysis 1995*, pp. 246-247.

Wert, J. A., Liu, Q. & Hansen, N. (1997), Dislocation Boundary formation in a cold-rolled cube-oriented Al single crystal, *Acta. mater.* **45**, pp. 2565-2576.

Wilkinson, A. J. & Dingley, D. J. (1991), Quantitative deformation studies using electron back scatter patterns, *Acta metall. mater.* **39**, pp. 3047-3055.

Wilkinson, A. J. & Dingley, D. J. (1992), The distribution of plastic deformation in a metal matrix composite caused by straining transverse to the fibre direction, *Acta metall. mater.* **40**, pp. 3357-3368.

Wilkinson, A. J. (1996), Measurement of elastic strains and small lattice rotations using electron back scatter diffraction, *Ultramicroscopy* **62**, pp. 237-247.

Wilkinson, A. J., Henderson, M. B. & Martin, J. W. (1996), Examination of fatigue crack plastic zones using scanning-electron-microscope-based electron diffraction techniques, *Phil. Mag. Lett.* **74**, pp. 145-151.

Wright, S. I., Dingley, D. J. & Field, D. P. (1996), Determining deformation, recovery and recrystallization fractions from orientation imaging microscopy (OIM) Data, *Proceedings of Microscopy and Microanalysis 1996*, pp. 352-353.

Appendix

A CD-ROM accompanies this work. 'Yuki - An EBSD Analyzing Tool' can be found on it, as well as the source code written in VB 5.0. The readme.txt file gives detailed information about the installation.
Some data files are included to allow experimenting with the software.
Moreover, two manuals were written during the present work, one for the EBSD system itself and an other one for Yuki. These two can also be found on the CD-ROM as *.doc files.
The CD-ROM contains also all the figures used in the present work.